XXI. NEUROLOGY*

L. Stark
S. Asano
F. H. Baker
Julia R. Bristol
C. A. Finnila
G. Gottlieb
H. T. Hermann
J. C. Houk
R. Howland
R. G. Kurkjian
K. D. Labaugh
G. P. Nelson
C. Northrup
Y. Okabe
M. Okajima
R. C. Payne
Helen E. Rhodes
P. R. Samson
V. Sanchez
A. Sandberg
G. Sever
G. Siegal
J. Simpson
I. Sobel
S. F. Stanton
J. Stark
Y. Takahashi
E. Van Horn
P. A. Willis
L. R. Young
W. Zapol

A. DYNAMICS OF THE HUMAN LENS SYSTEM

1. Introduction

The automatic focusing system of the human eye is one of the important servomechanisms in the human body and has attracted the interest of many physiologists.

When a man looks at an object his eyes focus on the target and the result is a clear image on the retina. When the eye does not focus on the object the retinal image blurs. The information concerning the state of the retinal image is sent to the optic center of the brain which processes it and sends the ciliary muscle orders to either contract or relax and thus to change the refractive power of the lens. This feedback loop is represented by the block diagram of Fig. XXI-1.

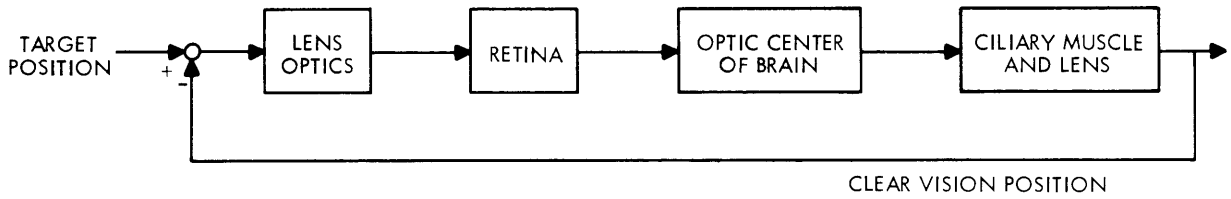

Fig. XXI-1. Feedback loop.

The way that the optic center processes the information sent from the retina is still unrevealed, although several hypotheses have been put forward such as the effect of aberrations[1] and noise.[2]

In order to reveal the mechanism of accomodation, we investigated the dynamic properites of the lens system using the frequency response approach. Our experimental data on the frequency response of the human lens system and the method of

*This research is supported in part by the U.S. Public Health Service (B-3055, B-3090), the Office of Naval Research (Nonr-1841(70)), the Air Force (AF33(616)-7588, AF49(638)-1130), and the Army Chemical Corps (DA-18-108-405-Cml-942); and in part by the National Science Foundation (Grant G-16526).

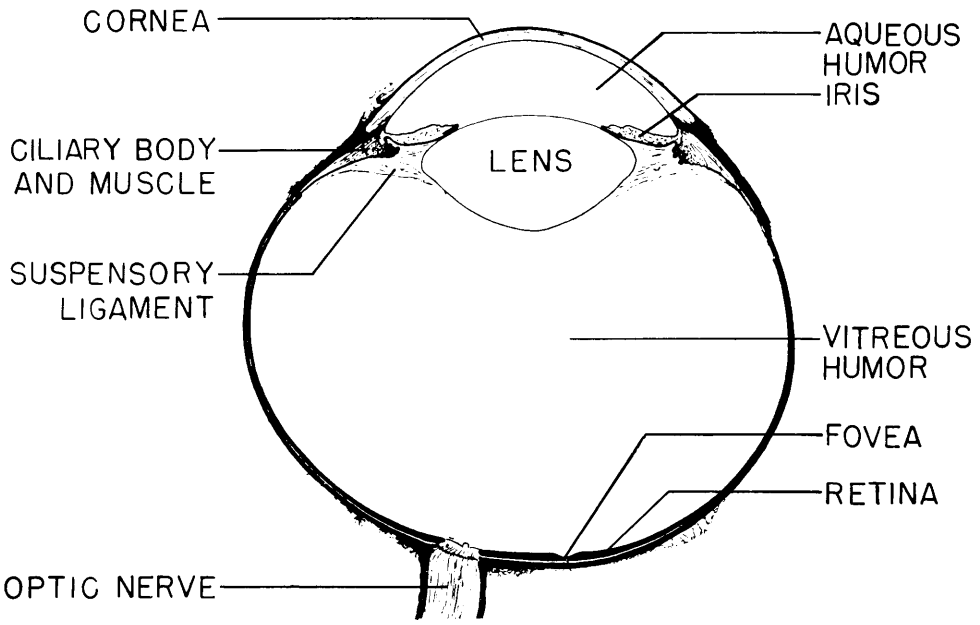

Fig. XXI-2. The human eye.

analysis will be given.

Before discussing the dynamics of the eye lens system, the anatomy of the eye will be briefly reviewed. Figure XXI-2 shows a cross section of the eyeball. The crystalline lens is composed of the lens capsule and the single-layered lens epithelium that contains elastic lens substance. It is held in a state of tension by the pull of the suspensory ligament. The fibers of the ligament are connected to the ciliary body. It is the intraocular pressure that causes a pull on the suspensory ligament and reduces curvature of the crystalline lens. In this state the eyes are at rest or looking to infinity. In near vision accomodation is necessary to bring about a clear image. This accommodation is made possible by contraction of the ciliary muscle. As this muscle contracts, the suspensory ligament is relaxed, and the lens becomes more spherical and increases its dioptric power.

2. Experimental Data

The dynamic properties of the lens system have been studied by recording the transient changes of refractive power of the lens caused by the input transient changes of object distance. The recording is made possible by using the infrared high-speed optometer of Campbell and Robson.[3] The data of this report were obtained by means of this optometer. The dynamic properties obtained from the experiment will now be described.

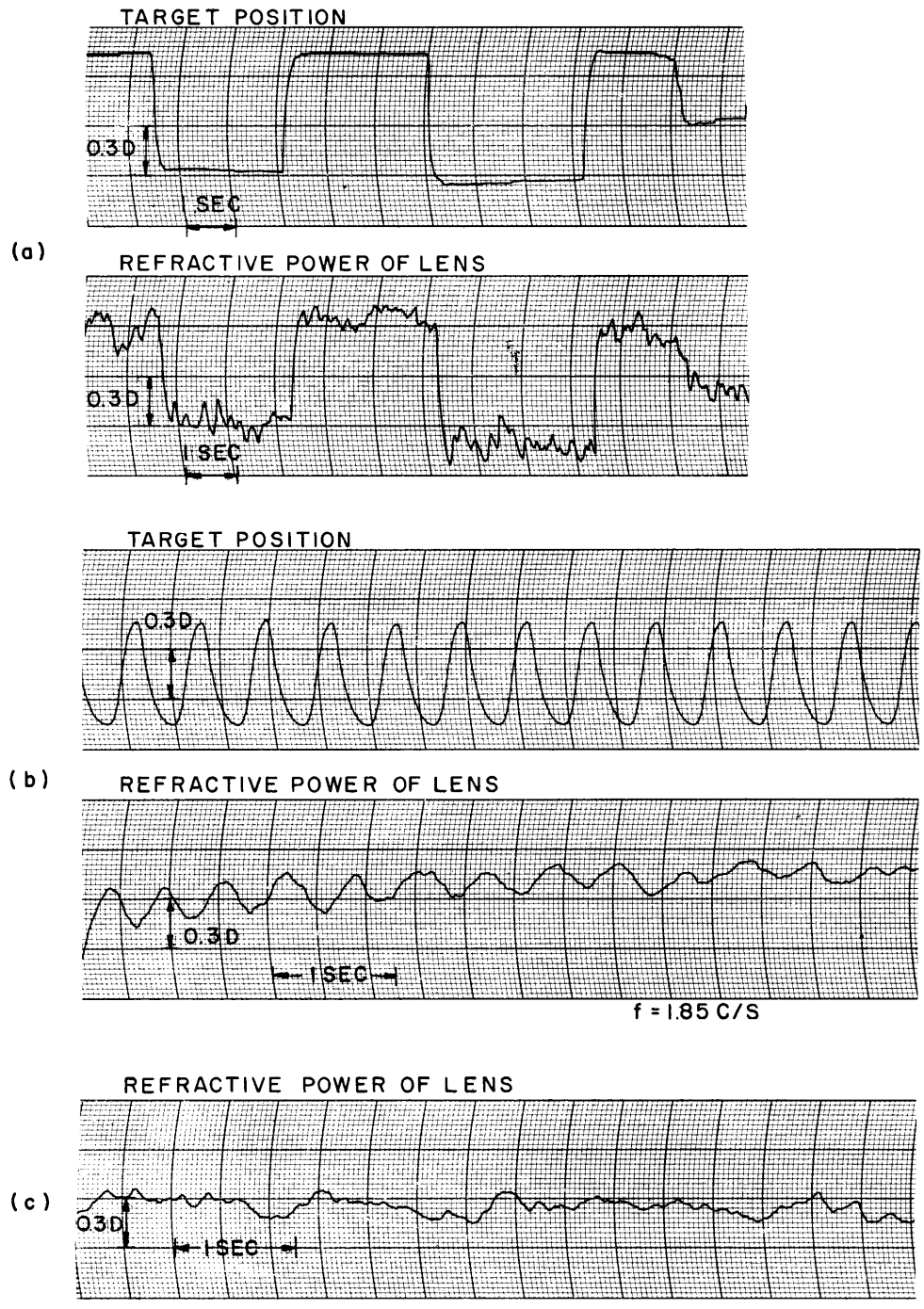

Fig. XXI-3. Actual response of lens to change in target position.

a. Step Response

The transient response of the refractive power of eye lens to stepwise change of the target position was studied, as shown in Fig. XXI-3a. The response to a step input is approximated by a negative exponential rise of the time constant T following a dead time. The responses are somewhat dependent on the direction of the movement of the target.

The average dead time and time constant obtained from these data are 0.36 sec and 0.4 sec, respectively, for far-to-near accommodation, and 0.38 sec and 0.4 sec, respectively, for near-to-far accommodation. This large dead time is the first difficulty encountered in understanding the dynamics of the eye lens system because a dead time of 0.38 sec would cause a 180° phase lag at only 1.3 cps, whereas there is no experimental evidence that instability is taking place at approximately this frequency.

b. Sinusoidal Response

The response of the eye lens system to oscillatory movement of the target was studied by Stark. One of the waveforms of the response is shown in Fig. XXI-3b.

By keeping the amplitude of the target motion constant and changing the frequency, the amplitudes and phase shifts of the refractive power of the lens were measured and are plotted in Fig. XXI-4. This is the closed-loop frequency response of the lens system. In Fig. XXI-4 there is a peak at approximately 2 cps which follows a considerable dip. Generally speaking, the lens system appears to be of the lowpass type.

Several attempts were made to represent this frequency response by a simple transfer-function model. The models used and the closed-loop frequency responses are shown in Fig. XXI-5.

It is clear from Fig. XXI-5 that none of these models can describe the experimental data, even with higher-order elements introduced. This result makes us realize that the eye lens system is a strongly nonlinear feedback system and that it cannot be described by any linear model.

To prove this point, the frequency responses were measured for three different input amplitudes: 0.2 D, 0.4 D, and 0.6 D (D denotes diopter). The results are shown in Fig. XXI-6 and show that there is an evident change in the shape of the response which depends on the magnitude of the input; this change proves the nonlinear characteristic of the lens feedback system.

c. Noise

The refractive power of the human lens is a constantly changing magnitude, even when the subject looks at a fixed target. This fluctuation was recorded and is shown in Fig. XXI-3c.

In Fig. XXI-7 the solid line refers to data obtained when the pupil is large. The

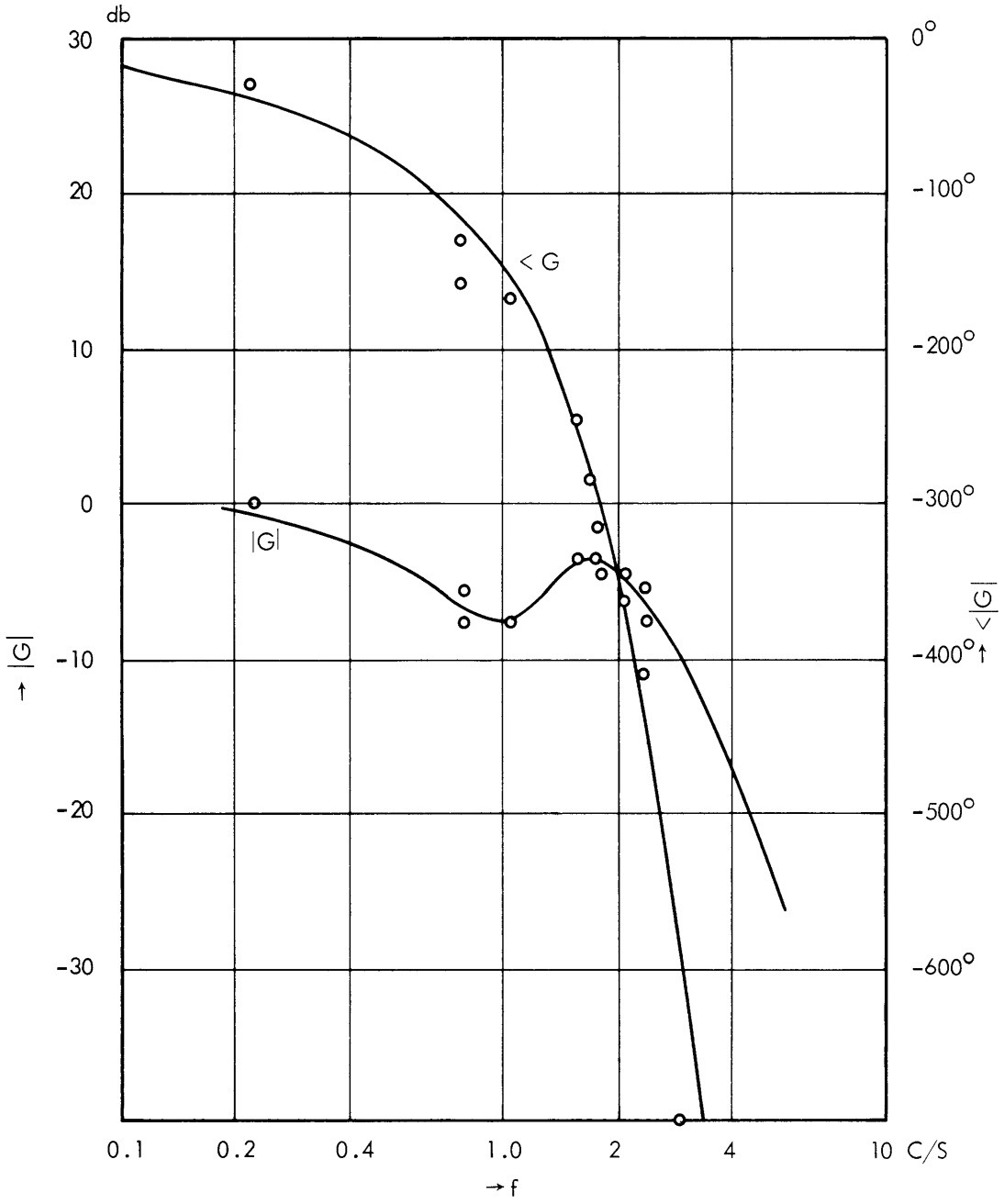

Fig. XXI-4. Closed-loop frequency response of lens system.

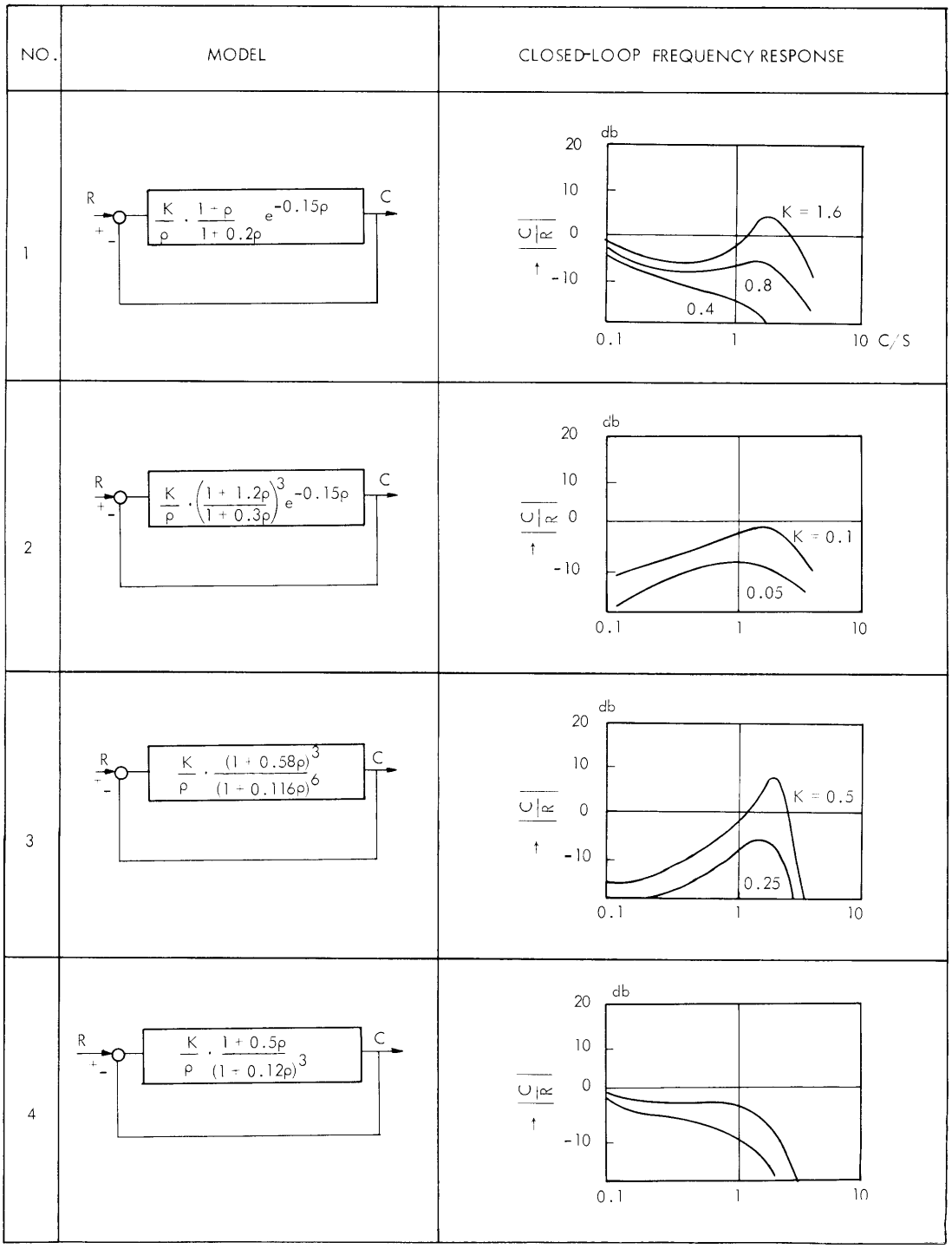

Fig. XXI-5. Transfer-function models and closed-loop frequency responses.

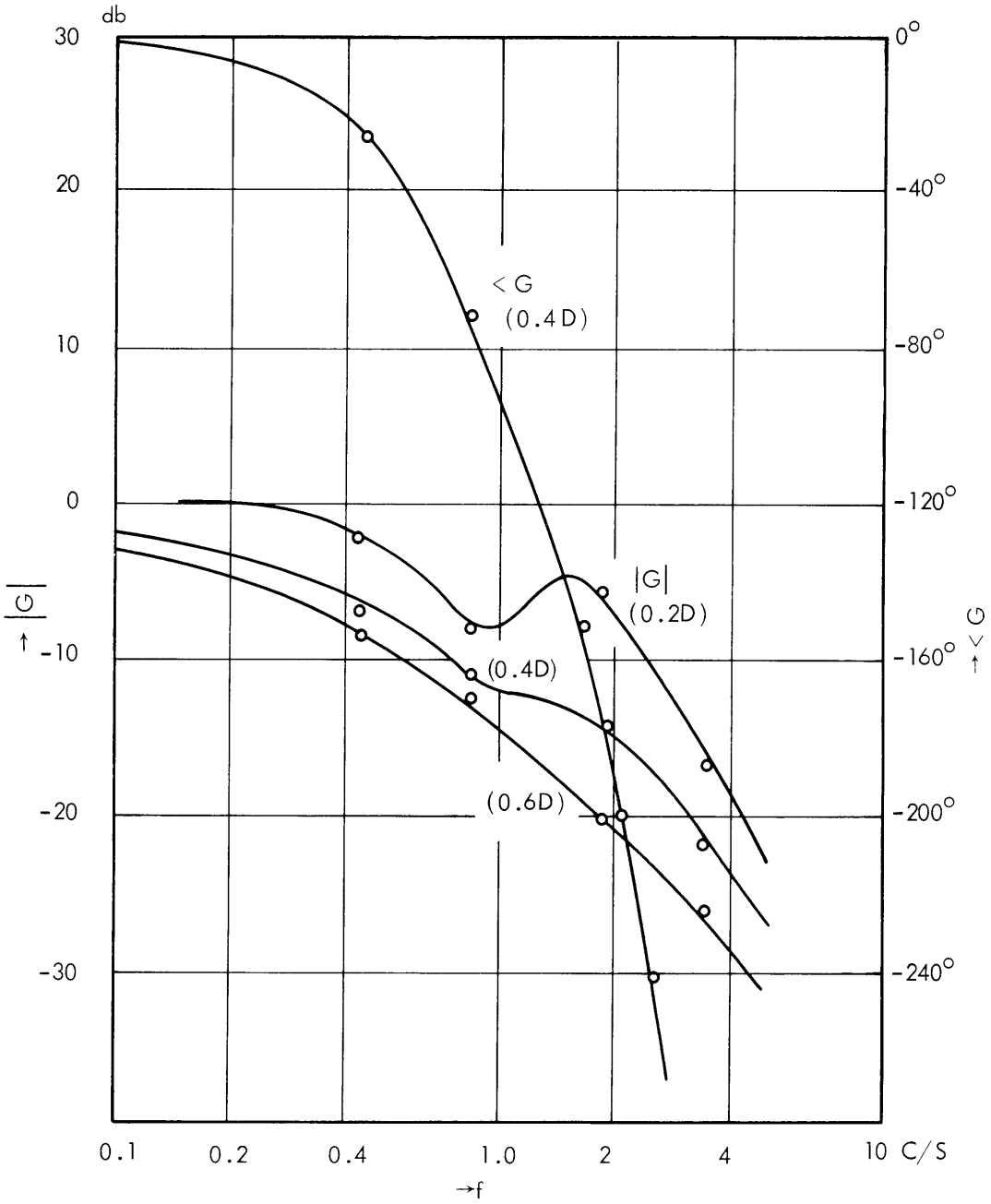

Fig. XXI-6. Frequency responses for different input amplitudes.

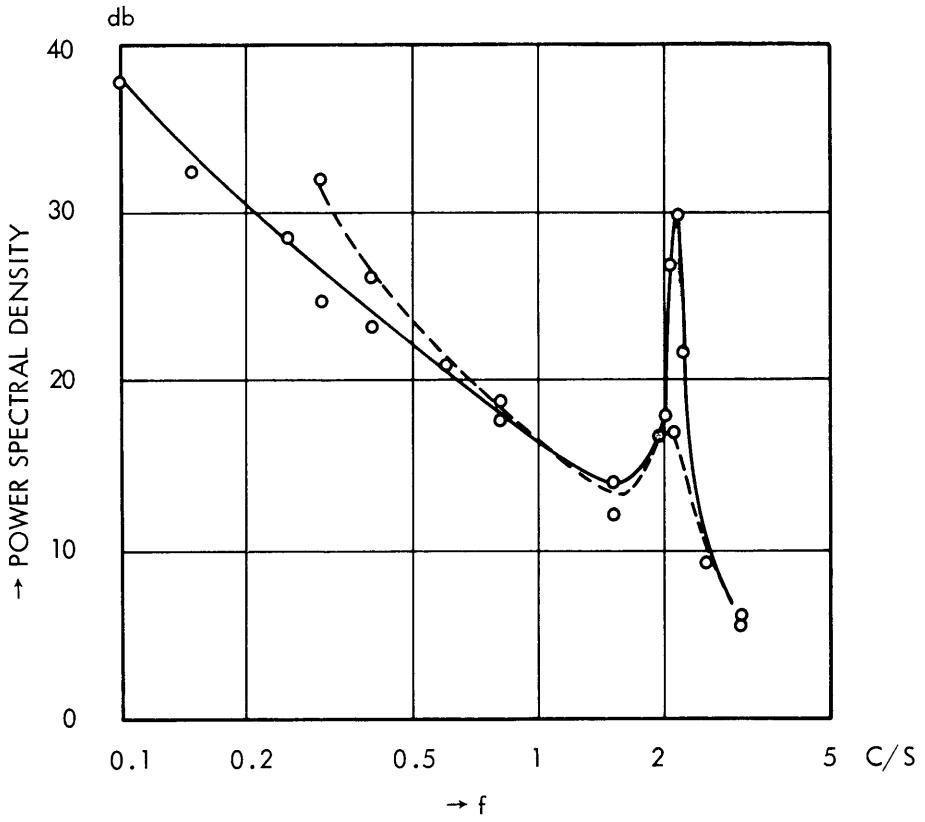

Fig. XXI-7. Power spectrum obtained from the time function.

dashed line refers to those obtained when the subject looked at the target through an artificial pupil of 1-mm diameter. The introduction of a small aperture before the eye eliminates the effect of distance to the target, so that the lens system is in the open-loop condition.

In Fig. XXI-7 the power spectrum for the closed loop shows a very sharp peak at 2 cps, whereas that for open loop is small.

3. Model of the Feedback System

We shall present a reasonable model of this feedback system to explain our experimental results. As we have mentioned, nonlinearity is of considerable importance in this system.

We begin our analysis by assuming that the feedback loop is constructed as in Fig. XXI-8, that is, as a linear element whose transfer function F(s) is preceded by a zero-memory nonlinearity.

According to the model of Fig. XXI-8, that which we measured in the frequency response experiment is $\frac{C(jw)}{R(jw)}$, while the amplitude of R(jw) is constant. The amplitude

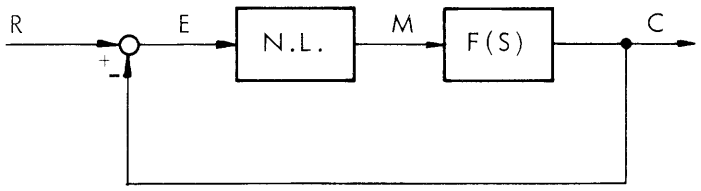

Fig. XXI-8. No-memory nonlinear and frequency-dependent linear elements of lens system.

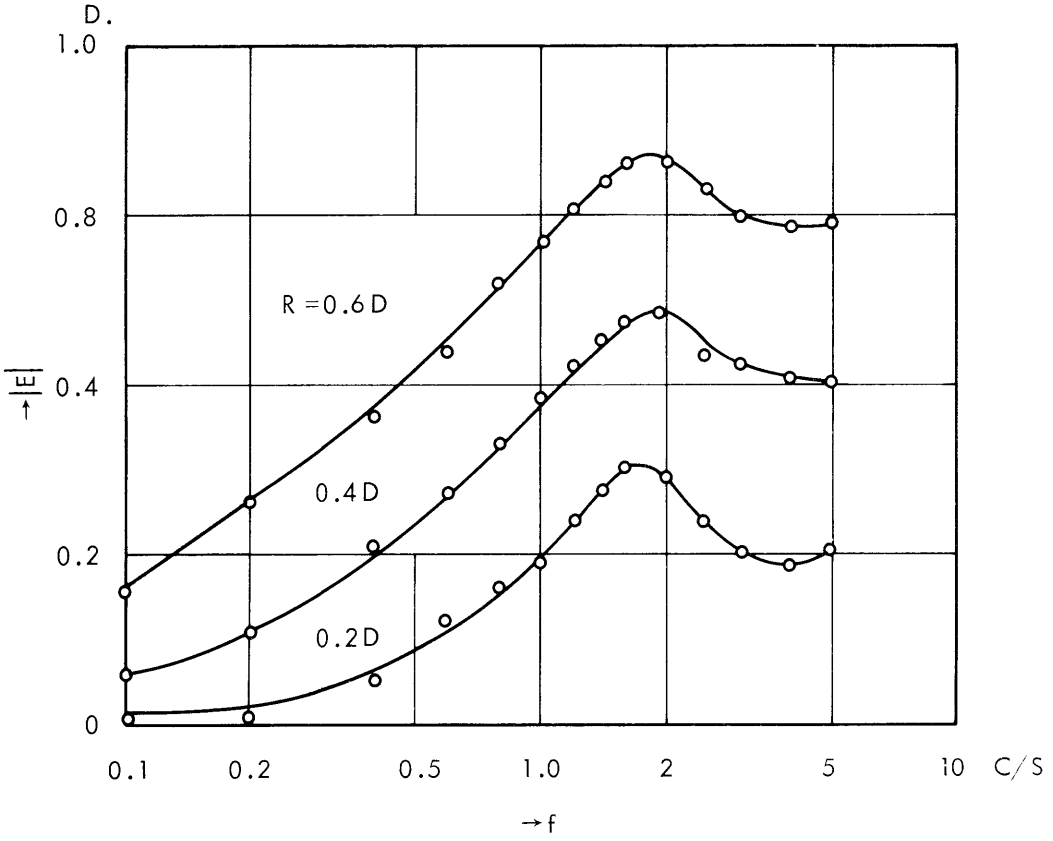

Fig. XXI-9. Error magnitude as a function of frequency.

of E does not remain constant as the frequency changes. We calculated $\frac{E}{R}$ from $\frac{C(jw)}{R(jw)}$ as

$$\left|\frac{E}{R}\right| = \left|1-\frac{C}{R}\right| = \sqrt{1+G^2-2G\cos\phi}, \tag{1}$$

where

$$\frac{C(jw)}{R(jw)} = G\, e^{-j\phi}. \tag{2}$$

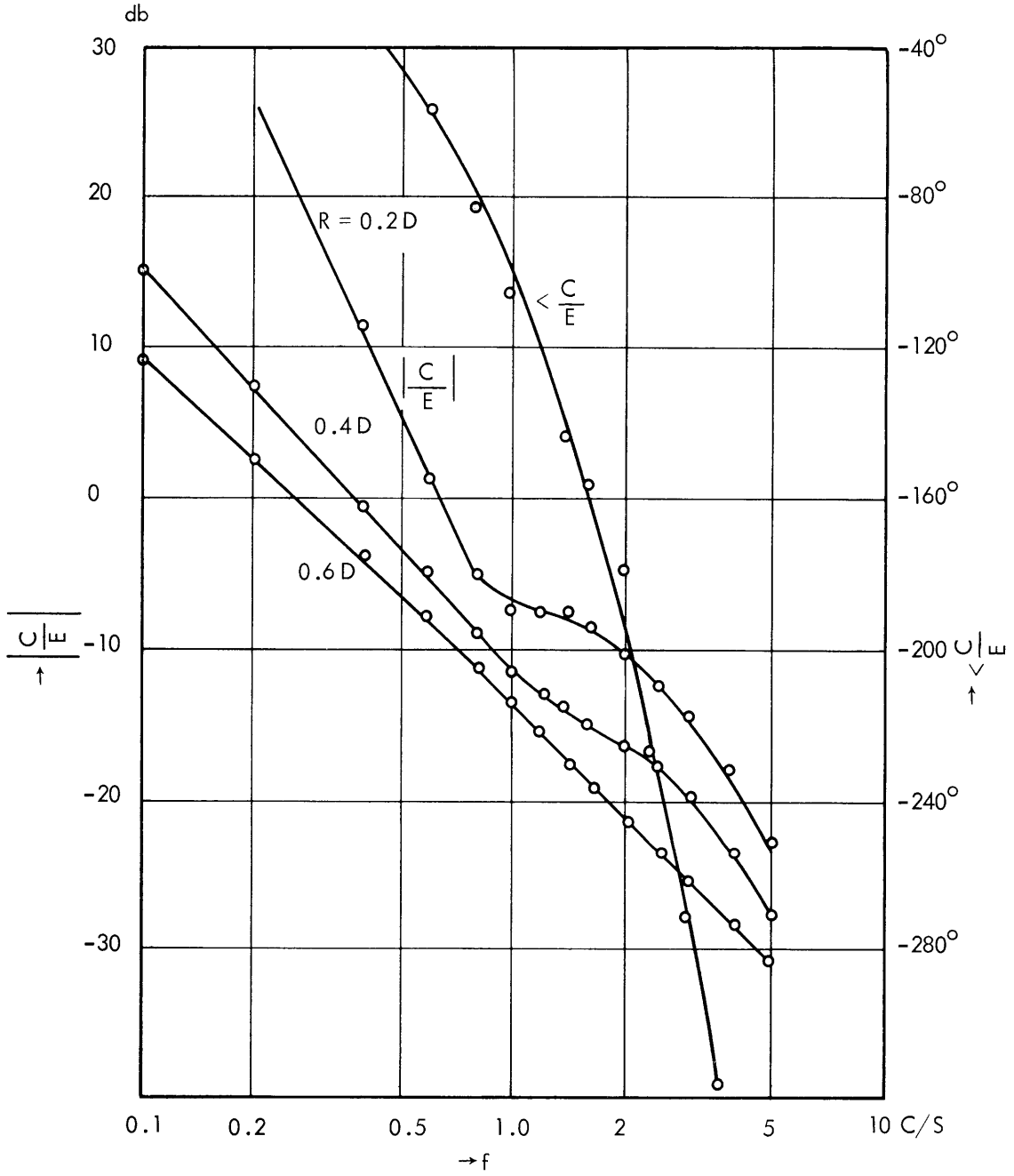

Fig. XXI-10. $\left|\frac{C}{E}\right|$ as a function of frequency.

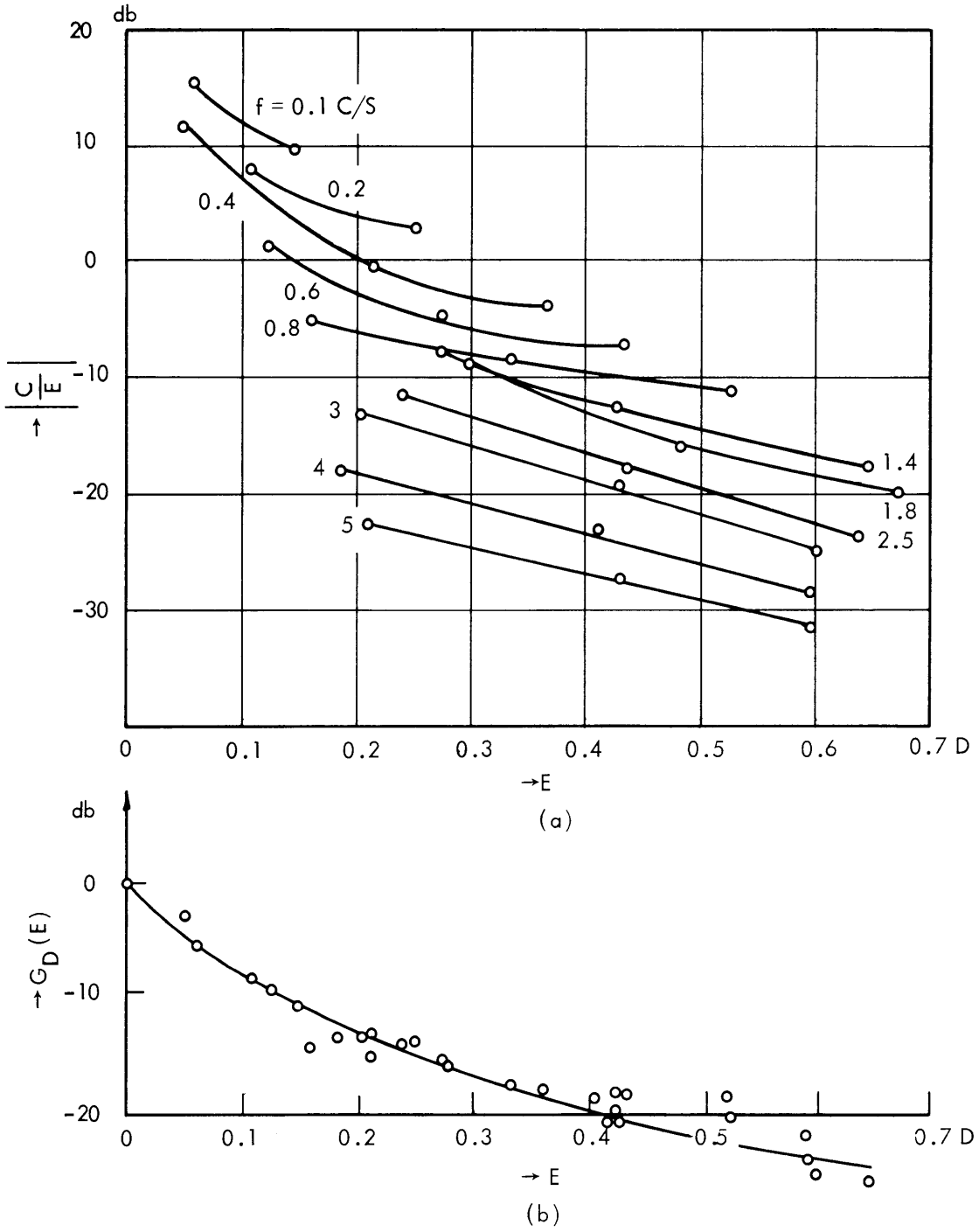

Fig. XXI-11. (a) $\left|\frac{C}{E}\right|$ as a function of error. (b) Describing function of nonlinear element.

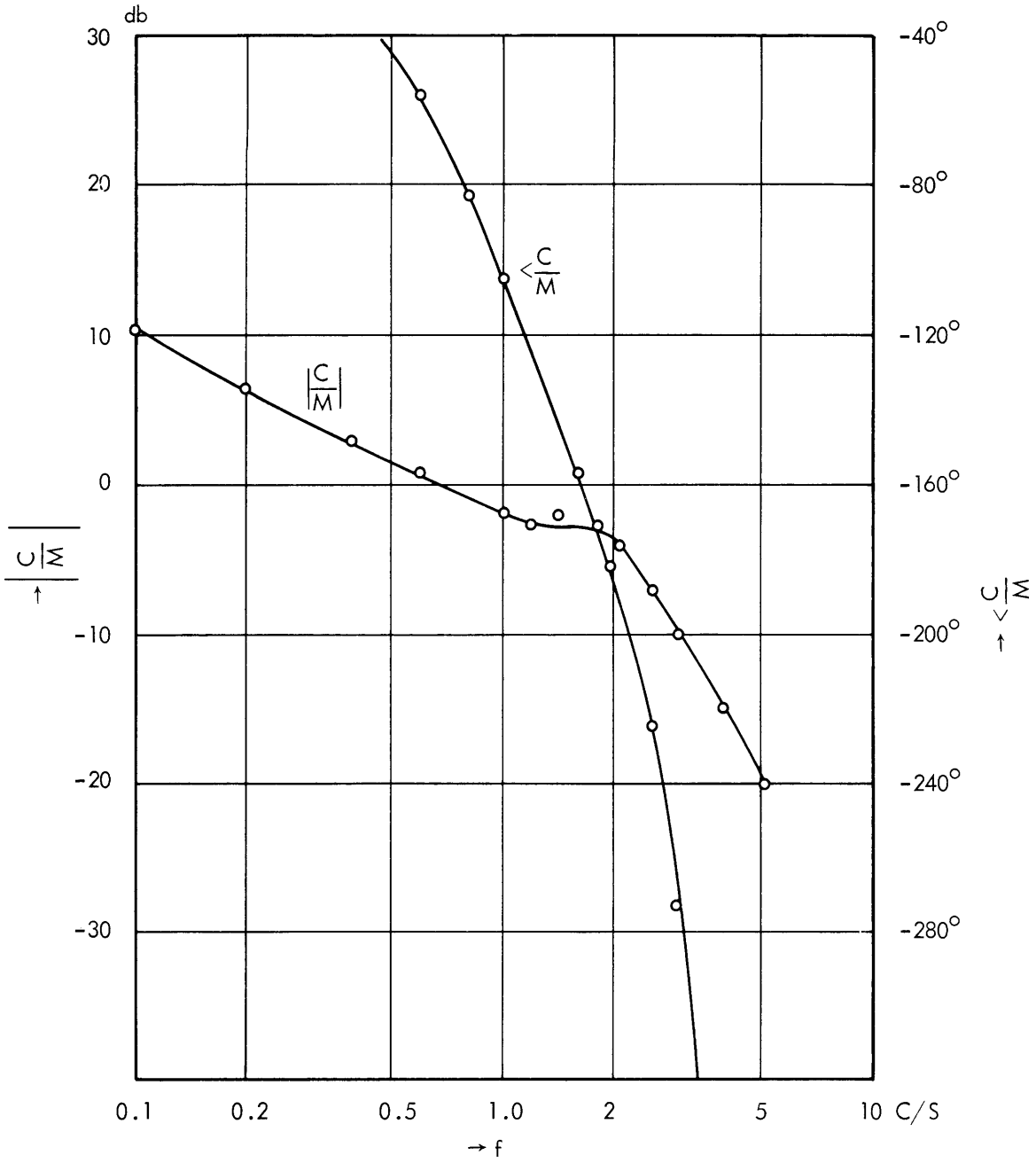

Fig. XXI-12. Linear element transfer function.

In Fig. XXI-9 E is plotted against frequency. For this calculation the phase lag for different input amplitudes is assumed to be constant.

We calculated $\frac{C(jw)}{E(jw)}$ under the same assumption and by using the following equation:

$$\frac{C(jw)}{E(jw)} = \frac{C(jw)}{R(jw)} \qquad \frac{E(jw)}{R(jw)} = \frac{G\, e^{-j\phi}}{1 - G\, e^{-j\phi}}. \tag{3}$$

The result is plotted in Fig. XXI-10.

On the basis of Fig. XXI-10 we ought to see that the input to the nonlinear element changes with frequency according to the curves of Fig. XXI-9. Three different attenuations in Fig. XXI-10 at the same frequency are caused by the nonlinear element. Since the magnitude of E at each frequency and at each R is found from Fig. XXI-9, we can plot $\left|\frac{C}{E}\right|$ versus E for different frequencies, as shown in Fig. XXI-11a. As these curves are segments of the describing function of the non-linear element, they must form a continuous curve when moved vertically. The result is given in Fig. XXI-11b which describes the function of the nonlinearity. By using Figs. XXI-9, XXI-10, and XXI-11b, the transfer function of the linear element is obtained, as shown in Fig. XXI-12.

4. Discussion

At the beginning of our analysis we assumed the model shown in Fig. XXI-8. Another model, in which the nonlinear element follows the linear element, is also possible. However, this model was not considered because, as we see from the time function of Fig. XXI-3b, the distortion of the sinusoidal waveform seems to be reduced by the low-pass network.

We shall now build an analytical model of the lens feedback system. The transfer function of a linear element that fits the attenuation characteristic of Fig. XXI-12 is

$$F(S) = \frac{5}{s} \frac{(1+s)}{(1+0.125s)^2} e^{-0.1s}. \tag{4}$$

The coincidence of phase characteristic between experimental data and the model is not perfect. Especially at lower frequencies, the discrepancy of the phases is large. Therefore it is necessary to improve the model. The nonlinearity is assumed to be that given in Fig. XXI-13. The closed-loop frequency response with constant input amplitude of this model was calculated and is given in Fig. XXI-14.

The nonlinear function in our model appears to clarify several previously unexplained characteristics of the accommodative control system: the effect of different input amplitudes on frequency response, the stable transient response to large steps, and the apparent instability displayed as the noise resonant peak. The integrator, the transport delay, and the linear lowpass element satisfy other characteristics of the system. More

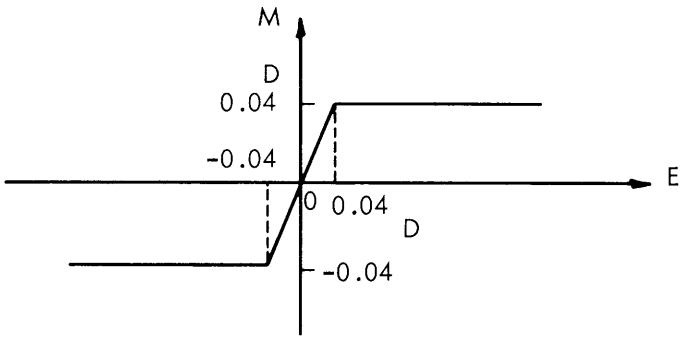

Fig. XXI-13. Static characteristics of the nonlinear element.

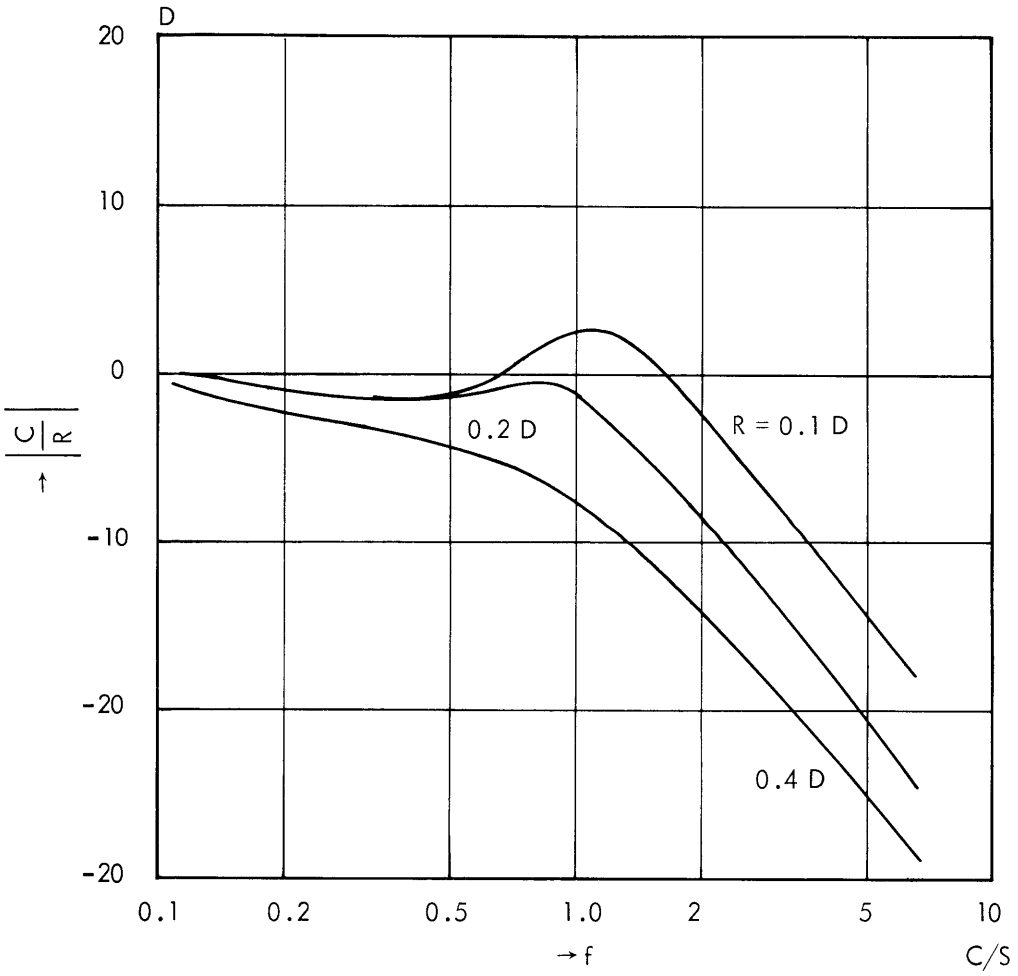

Fig. XXI-14. Closed-loop frequency response of the model.

experimental and theoretical work is needed.

We wish to thank Dr. Campbell and Dr. Robson for the hospiality of their laboratory where these experiments were carried out; for publishing one of our frequency response experiments,[4] and for many stimulating and critical discussions.

L. Stark, Y. Takahashi, G. D. Zames

References

1. F. W. Campbell and G. Westheimer, Factors influencing accomodation responses of the human eye, J. Opt. Soc. Am. 48, 568 (1959).

2. M. Alpern, Variability of accommodation during steady fixation levels of illuminance, J. Opt. Soc. Am. 48, 193 (1958).

3. F. W. Campbell and J. G. Robson, High speed infrared optometer, J. Opt. Soc. Am. 29, 268 (1959).

4. F. W. Campbell and G. Westheimer, Dynamics of accomodation responses of the human eye, J. Physiol. 151, 285 (1960).

B. SINGLE-UNIT RESPONSES IN A PRIMITIVE PHOTORECEPTOR ORGAN

1. Introduction

Although most nervous system responses apparently utilize large numbers of neurons, neurophysiologists have long been attracted by the elegant clarity of nerve impulse trains generated by a single neuron. Studies of single-unit responses have opened fruitful pathways, especially in the field of sensory reception. Single-unit isolation often makes possible the analysis of otherwise obscure experimental material. More important, these units provide the primary links of communication within the nervous system. In addition to knowledge of the single-unit response, it is clearly imperative to have an understanding of the rules of combination of the primary links in reconstructing the total response.

A few workers[1-3] have attempted rigorous quantitative analysis of single-unit response dynamics: usually the delineation of a mathematical statement, for example, the transfer function.

The transfer function, a linear integro-differential equation, enables one to summarize quantitatively the input-output relationships as a function of the convenient Laplace-transform complex variable. The parameters of this equation should have a clear correspondence to elements in the system that is under investigation.

The interesting photoreceptor organ of the sixth abdominal ganglion of the crayfish, Orconectes virilis (Hagen), when stimulated by light while it is in situ, responds with trains of nerve pulses. It has no complex optical or retinal arrangements that would render neural analysis less general. The entire population of nerve fibers conducting

impulses to the brain in response to light stimulation has already been quantitatively studied and a transfer function obtained for the response dynamics.[4,5] It was felt that single-unit analysis would be especially valuable here in view of both the known population-transfer characteristics and the suitability of this system for study of its combinational rules in effecting certain tropisms.

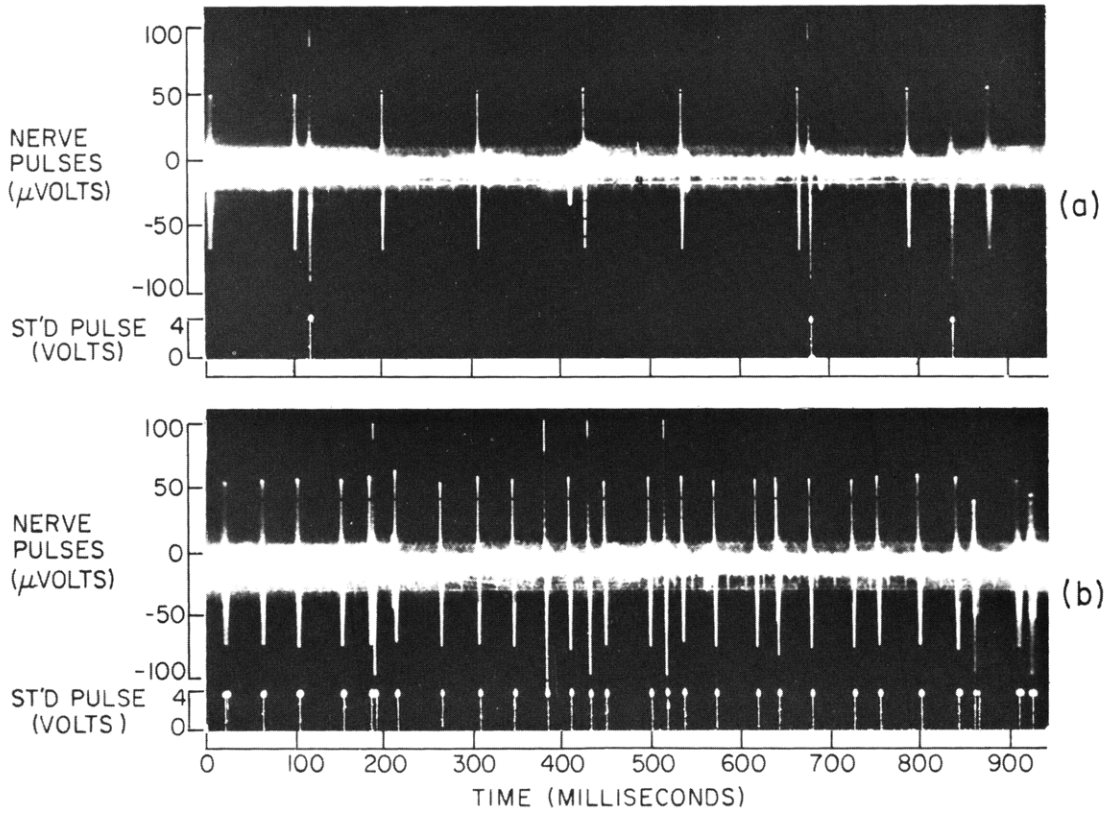

Fig. XXI-15. Nerve-impulse activity with (a) low and (b) high illumination. Activity consists of an A-fiber unit (large-amplitude proprioceptor) and one B-fiber unit (medium-amplitude light fiber). Trace pair (a) shows nerve-cord activity (upper) and shaped triggered pulses (lower) solely for A-fiber nerve impulses. Trace pair (b) shows nerve-cord activity (upper) and shaped triggered pulses (lower) corresponding to both A- and B-fiber nerve impulses. C-fiber activity and noise are excluded from the standard pulse generator in both (a) and (b).

2. Method

A moderate-sized specimen of Orconectes virilis (Hagen) was fixed to a cork board with soft rubber tubing in supine position. An electronic servo-controlled glow-modulator light source[4] with a range 0-8 millilumens, and a 10-μsec rise time, was focussed to a π mm^2 spot over the sixth abdominal ganglion of the ventral cord. The recording

chamber provided control of light, vibration, and temperature (19 ± 9.5°). Humidity control (100 per cent saturation) prevented drying or drop accumulation and thus permitted recording of nerve pulses without recourse to oil layer and perfusion fluid techniques.[5] Glass-insulated platinum-rhodium electrodes, 0.25 mm in diameter, were positioned by means of standard micromanipulators. With careful attention to hemostasis, recording for 6-8 hours was possible.

A 3 × 12 mm window, excised from the overlying exoskeleton, permitted access to the cord. The ventral artery that supplied the sixth abdominal ganglion was carefully dissected free and displaced to one side. Puncture or damage to this artery will weaken the preparation. The tough fibrous sheath surrounding the cord was dissected by means of glass microknives. Under microscopic visual control the cord was first hemisected and then progressively cut with microscissors (Shaffhausen) and fractionated with the microknives until a single light unit was isolated (determined by monitoring on a cathode-ray oscilloscope). Light signal-carrying nerve fibers generate pulses of medium (B) amplitude. Since the dissected nerve fascicle often contained both high- and low-amplitude pulses from fibers of different modalities (for example, tactile, proprioceptive), final isolation of the responding unit was effected by means of an electronic "pulse-height window."[6]

In this technique, only nerve impulses greater than a selected dc level can trigger a standard pulse. When low-voltage C pulses have been excluded (Fig. XXI-15b), the

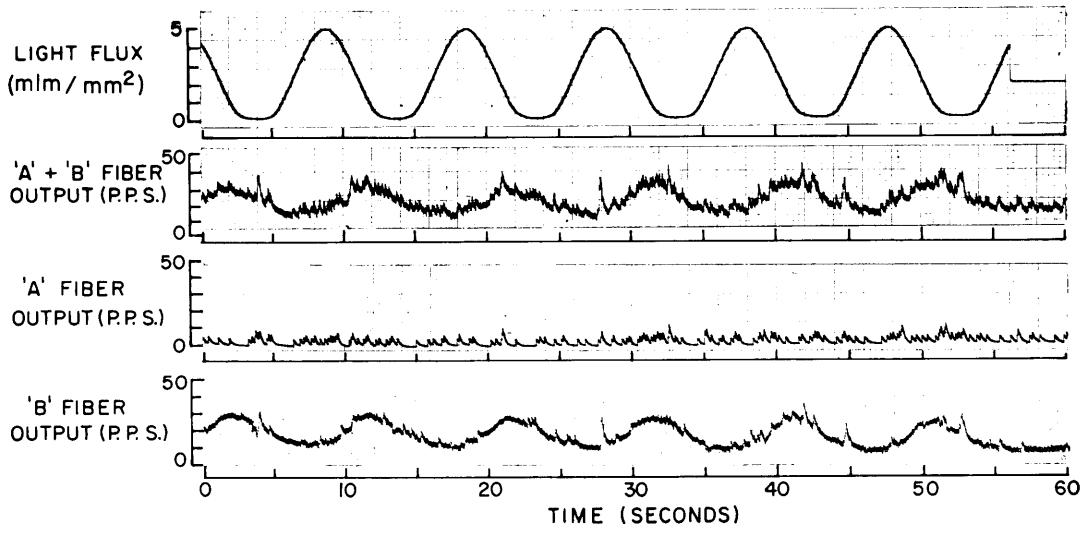

Fig. XXI-16. Sinusoidal variations in light flux (top trace) driving light-sensitive B fiber with an admixture of uncorrelated A-fiber impulses (second trace). When A-fiber impulses are isolated (third trace) and subtracted from combined A + B response an "impulse amplitude window" is formed to pass exclusively B-fiber impulses (fourth trace).

triggered pulses of the high-voltage (A) pulses (Fig. XXI-15a) may be subtracted from a combined set of A and B pulses (Fig. XXI-15b) and thus leave only B pulses (light-signal pulses) for computational purposes. The residual B pulses represent the raw-nerve pulse, generated by the light-sensitive unit. Figure XXI-15a shows the standard pulses triggered by each height-selected raw pulse. The output of the standard pulse generator is passed through a lag element (RC network) whose time constant, 0.20 sec, is long with respect to the pulse repetition rate, but short with respect to the response frequency of the phototransduction process. The resultant analog voltage corresponds to the average pulse frequency and is displayed by a conventional pen writer. This sequence may be seen in Fig. XXI-16. By combining the pulse-height window and surgical dissection, isolation of units becomes easy. The graphical display continuously sketched by the pen writer provided a convenient way of studying fluctuations in pulse rate and was used throughout this study for quantification of a single light unit from the photoreceptor organ.

By monitoring of changes in pulse-rate output, and at the same time controlling and monitoring the impingent light flux, one can construct the transfer characteristics of the photoreceptor unit. In this study, stimulus waveforms were restricted to sinusoids of various frequencies for steady-state analysis and steps for analysis of transient characteristics. Fourier synthesis techniques easily show the relationship between responses to these particular stimulus shapes and can be used to predict response to arbitrary stimulus waveforms.

3. Results

a. Dynamics

Small sinusoidal fluctuations of light intensity about a mean dc level produce regular responses in terms of average pulse-repetition rate, as shown in Fig. XXI-17. On subsidence of initial condition transients, response is related to input by two parameters at each frequency: gain (relative amplitude of input and output) and phase shift (amount of lag of response after stimulus). The harmonic distortion seen in examples of Fig. XXI-17 is typical and indicates that little power is present in higher harmonics as compared with fundamental response. Noise and time variations were minimized by averaging. Arranging the sequence of stimulating frequencies in random order eliminated possible trends. Clearly, response diminishes at higher frequencies; simultaneously, phase lag increases.

A Bode plot, as shown in Fig. XXI-18, enables one to assemble gain and phase data from many frequency-response runs into a compact and understandable display. The curves and asymptotes, derived from a best-fit transfer function, summarize quantitative features of the response. Low-frequency gain is 12 pulses sec^{-1} mlu^{-1} mm^2. The break frequency is 0.12 cps (0.75 radians per second), that is, the time constant

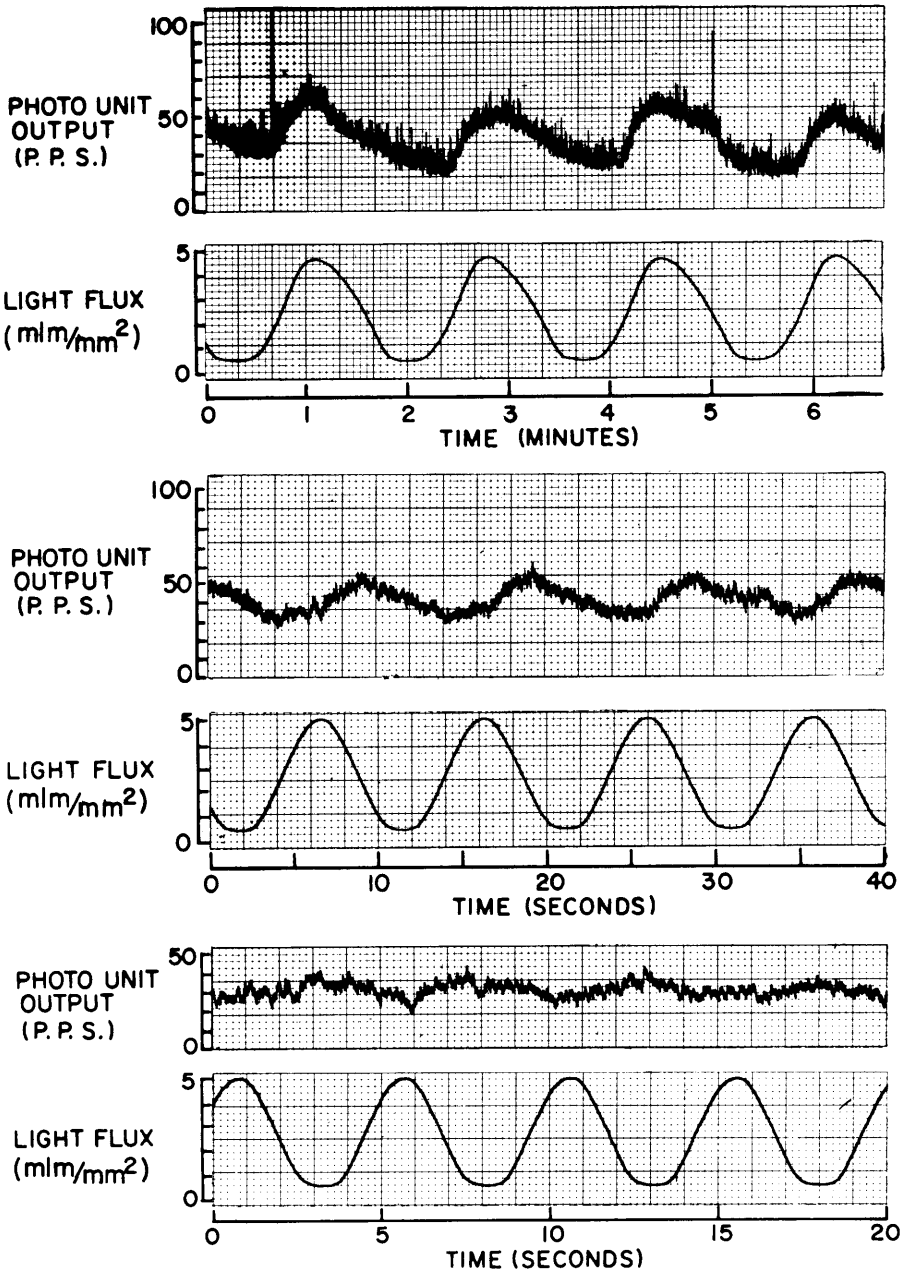

Fig. XXI-17. Sample of steady-state response of single B-fiber unit at 3 driving frequencies to show characteristics of system behavior. In top trace, 0.01-cps input produces an output with amplitude of ±13.3 pps, a mean of 37 pps, and a phase lag of 0°. Center, a 0.1-cps input shows an output amplitude of ±8.2 pps about a mean of 41.8 pps and with 122° phase lag. Bottom, a 0.2-cps input results in an output of ±3.4 pps, a mean of 27 pps, and 180° phase lag.

of the system is 1.3 sec. At the break frequency, gain is down 6 db. At higher frequencies, gain decreases with a -2 slope (12 db/octave, 40 db/decade, or 20 decilog/decade), which is equivalent to a second-order critically damped lag element. This can be represented as $1/(1+1.3s)^2$, where s is the Laplace transform complex variable (roughly equivalent to d/dt). Divergence of low-frequency data suggests the presence of very slow adaption (a distant zero on the negative real axis), which is not quantitatively examined in these experiments, nor represented in the transfer function.

Theorems relating phase lag and gain for minimum phase elements (MPE) enable one to assign the phase that is appropriate to a second-order lag in the plot of phase as a function of frequency, as shown in Fig. XXI-19. Phase lag due to a nonattenuating

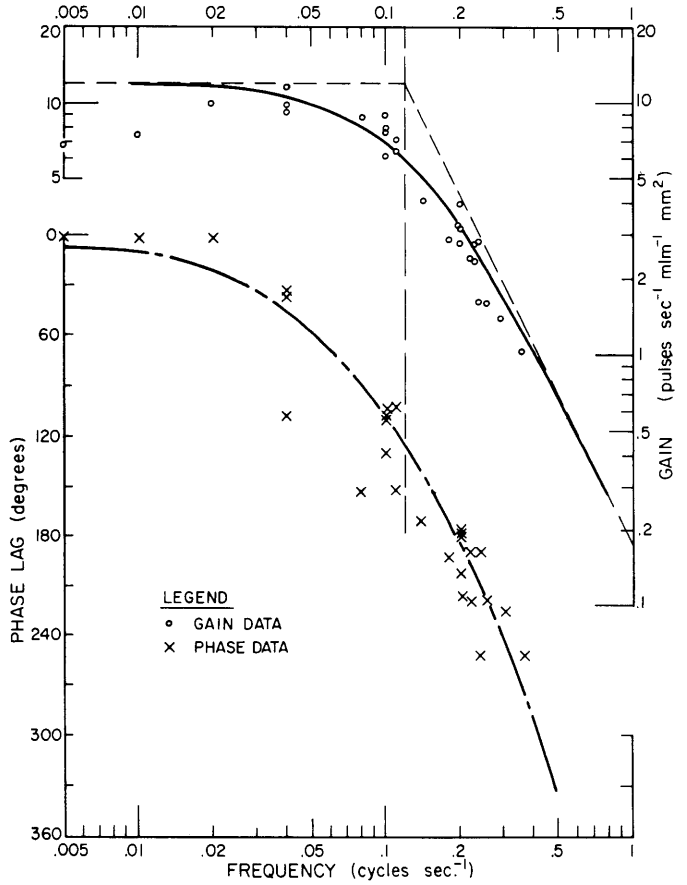

Fig. XXI-18. Bode plot. Gain is plotted on a log-log scale, phase lag on linear-log scale; points are experimental. Continuous line of gain plot is guided by asymptotes on either side of break frequency. Response is down 6 db at break frequency of 0.12 cps, which is characteristic of a second-order critically damped system. Phase-lag curve is computed from sum of the minimum and nonminimum phase elements in transfer function.

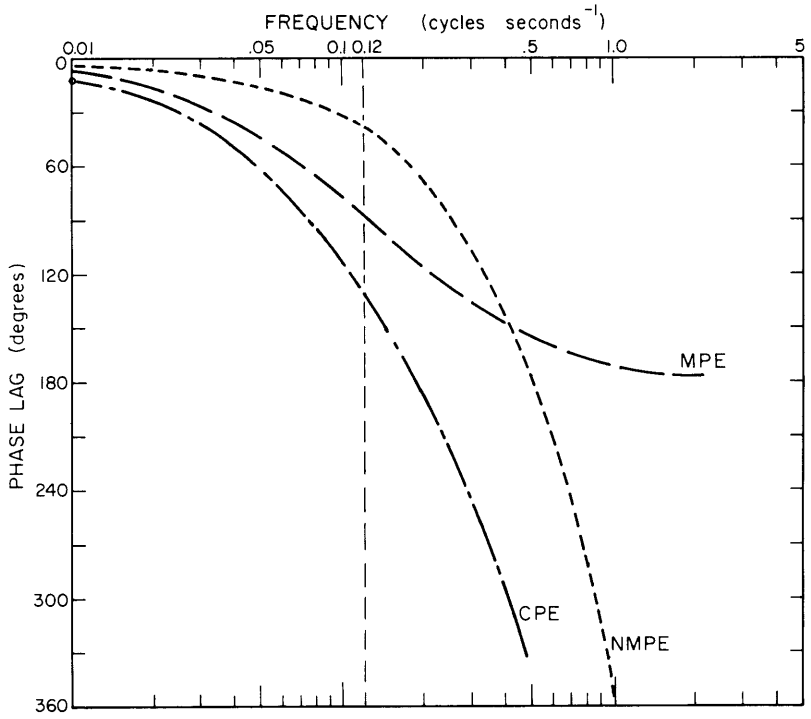

Fig. XXI-19. Bode plot. Decomposition of phase elements. Composite curve CPE computed from joint contributions of nonminimum phase elements (NMPE) and minimum phase elements (MPE). MPE (lag elements) computed from experimentally obtained second-order equation, $1/(1+1.3s)^2$. NMPE, because of transport delay, (1.0 sec), represents an element that, when added to MPE, produces a good approximation to experimental data. Note that no phase advance appears in the frequency range studied; points are experimental.

time-delay factor, the nonminimum phase elements (NMPE), is linearly proportional to frequency, and shows an ever decreasing slope on the logarithmic frequency scale in Fig. XXI-19. The two components, MPE and NMPE, sum together to produce total system phase lag. The 1-sec time-delay factor has the form $e^{-1.0s}$. Experimental phase points appear to fit the total phase curve (except at low frequencies at which the adaption element produces some phase advance).

We may assemble the transfer function:

$$G(s) = \frac{12\, e^{-1.0s}}{(1+1.3s)^2} \qquad \text{pulses}^{-1}\ \text{millilumen}^{-1}\ \text{mm}^2, \tag{1}$$

where components on the right-hand side have been assigned forms and parameters from the experimental frequency-response results given above. A less convenient form is the classical integro-differential equation,

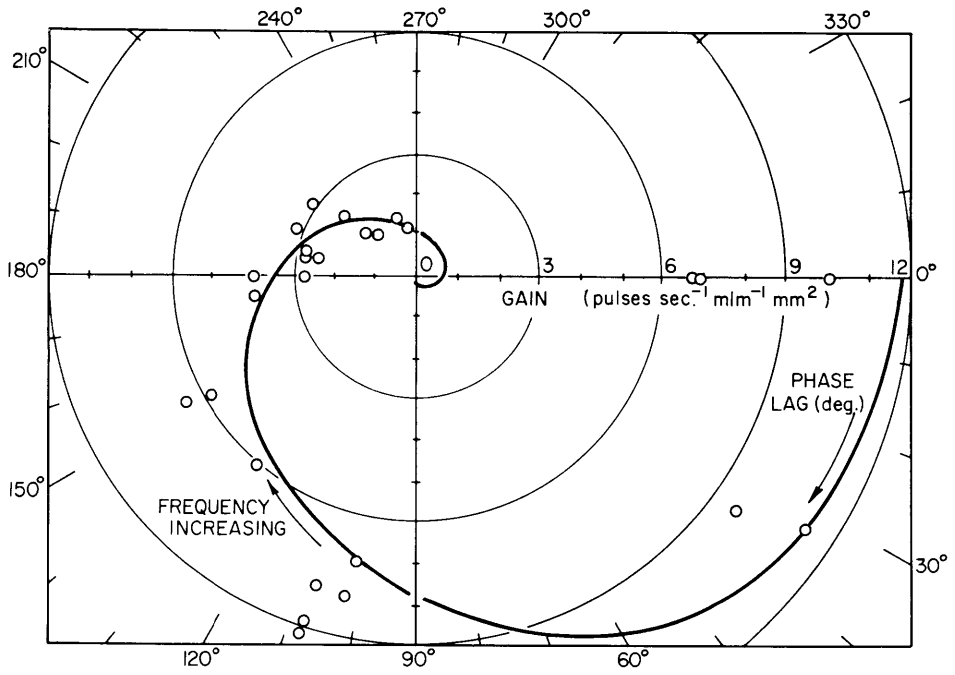

Fig. XXI-20. Nyquist plot of gain vs phase relationship of single-unit response to light. Solid line computed from transfer function. Experimental points are same data as in Fig. XXI-18. Frequency increases monotonically, but not regularly, in clockwise direction. Phase lag increases as the result of both MPE and NMPE; gain decreases as phase increases because of second-order lag; both, combined, account for spiral in toward zero in this polar plot representation.

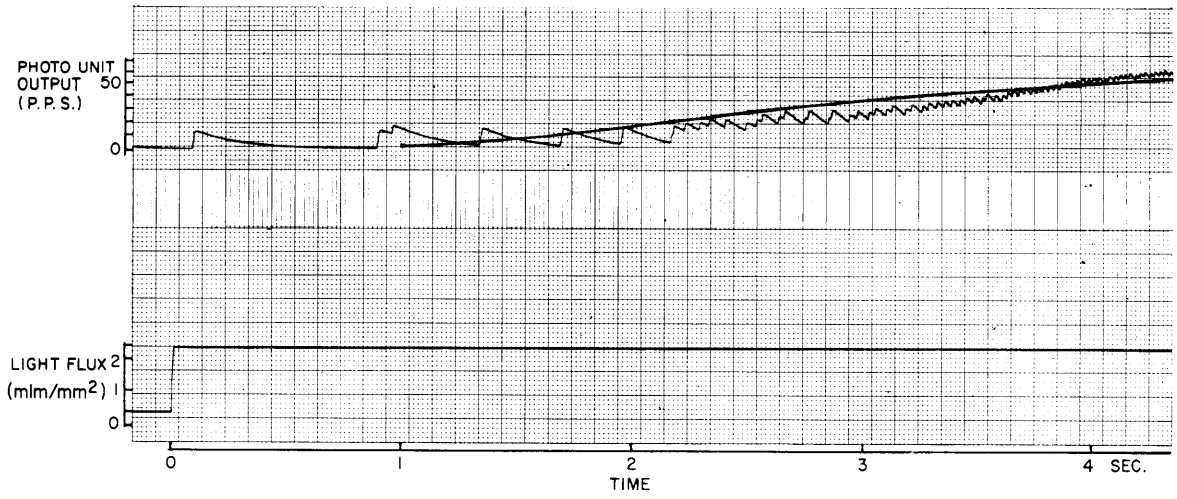

Fig. XXI-21. Response to small steps is shown with prediction from transfer function. The response to large steps with its transfer function shows more rapid rise, overshoot, higher dc level, and more adaptation.

$$12\, I(t-1.0) = 1.69 \frac{d^2F}{dt^2} + 2.6 \frac{dF}{dt} + F, \qquad (2)$$

where t is time in seconds, F is pulses per second, and I is light flux intensity in millilumens per square millimeter.

Another graphic display of the frequency-response data is shown in Fig. XXI-20, the Nyquist plot. This polar representation of gain and phase lag again shows the effect of the adaption element that reduces both the gain vector and phase lag at low frequencies.

The transfer function summarizes the dynamical behavior of the system not only to sinusoidal stimulation but to all physically realizable inputs. One important example is the step-function input. The predicted step response of the photoreceptor unit is indicated in Fig. XXI-21, together with actual experimental responses. The time delay of 1 sec and the second-order rise (one inflection point) clearly show the same characterisitcs as those derived in the frequency-response analysis. Furthermore, quantitative agreement between the transfer-function prediction (dashed line) and experiment (the pulse-rate trace) should be noted.

The 1-sec time delay of the transfer function is not due to nerve conduction time. The actual site of photochemical transduction is still wholly obscure.[7] The concentration of photopigment, if present, is below the limits of present-day detectability. Furthermore, it is likely that only 2-6 primary sensory neurons perform the light transduction.[8]

b. Sampling

The response of a single unit has a number of experimental advantages over the population response reported earlier by us. The signal-to-noise ratio is obviously improved, as comparison of Fig. XXI-22 with the middle trace of Fig. XXI-17 demonstrates. Much of the noise in the population response is due to the randomness introduced by summation of several mutually irrational, although strictly periodic, sequences.[9] The periodic sequences are the nerve-impulse trains generated by a single unit. The population is formed by summation of a number of single units whose pulse frequencies are not harmonically related. Single-unit responses are less conceptually removed from the actual neurophysiological generator of the sensory mechanism. Thus, single-unit study allows examination of basic biological processes.

However, it is important to justify the implicit assumption made in dealing with the single-unit sample: that the sample is actually representative of the physiological behavior of the population. In certain known physiological systems, such as the alpha motor neuron, and the position receptors of a joint, the single-unit response is not similar to the population response. An alternative arrangement, that of distributed thresholds, with a signal that is proportional to numbers of units firing at each state, transmits the signal.

The crayfish tail photoreceptor, however, does show that unit and population responses are almost identical. In fact, by comparing the Bode plot of Fig. XXI-23 of frequency-response data from the population with that from a single-unit in the same animal, it is seen that the phase data are not distinguishable. The gain data, fitted by asymptotes for the same transfer function, are similar, except for the dc gain. Population gain is three times unit gain. The population in this experiment apparently consisted of three individual units.

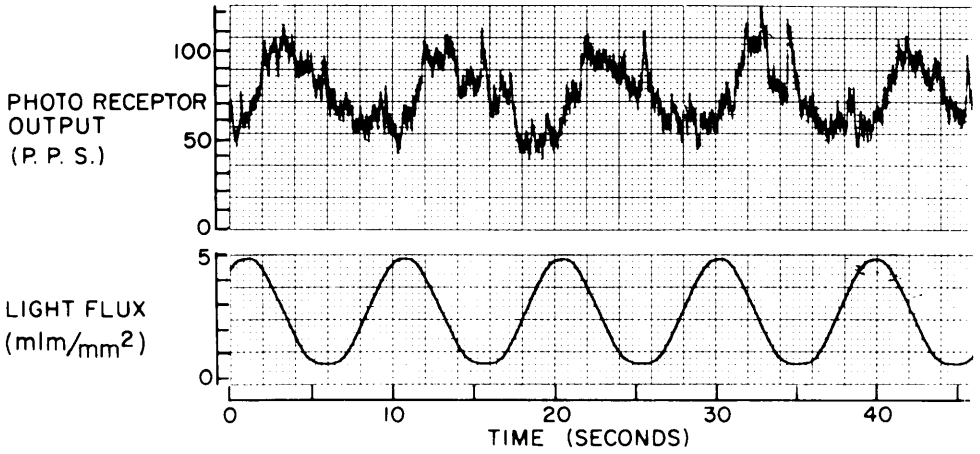

Fig. XXI-22. Sinusoidal fluctuations of light intensity stimulating sixth abdominal ganglion. (Driving frequency at 0.1 cps produces an output response of 24.6 pps about a mean of 74.6 pps and with phase lag of 140°.) This is the response of a population of units. Comparison with Fig. XXI-17 (response of a single B-fiber unit) clearly demonstrates the improvement in signal-to-noise ratio obtained by means of the window method of single-unit recording. Nonlinearities are similar in both population and single-unit response shapes.

Other evidence showing that the sampled single unit is representative of such photosensitive units in general may be seen in Fig. XXI-24. Here, four unselected single units, each from an individual preparation, are indistinguishable with respect to break frequency, attenuation slope, and phase characteristics. Low-frequency gain varied from preparation to preparation, and values of 4, 7, 7, and 12 pps^{-1} $millilumen^{-1}$ mm^2 were obtained; for comparison in the Bode gain plot, these gains were all normalized to 12. The asymptotes and curve are theoretical and are derived from the transfer function in Eq. 1.

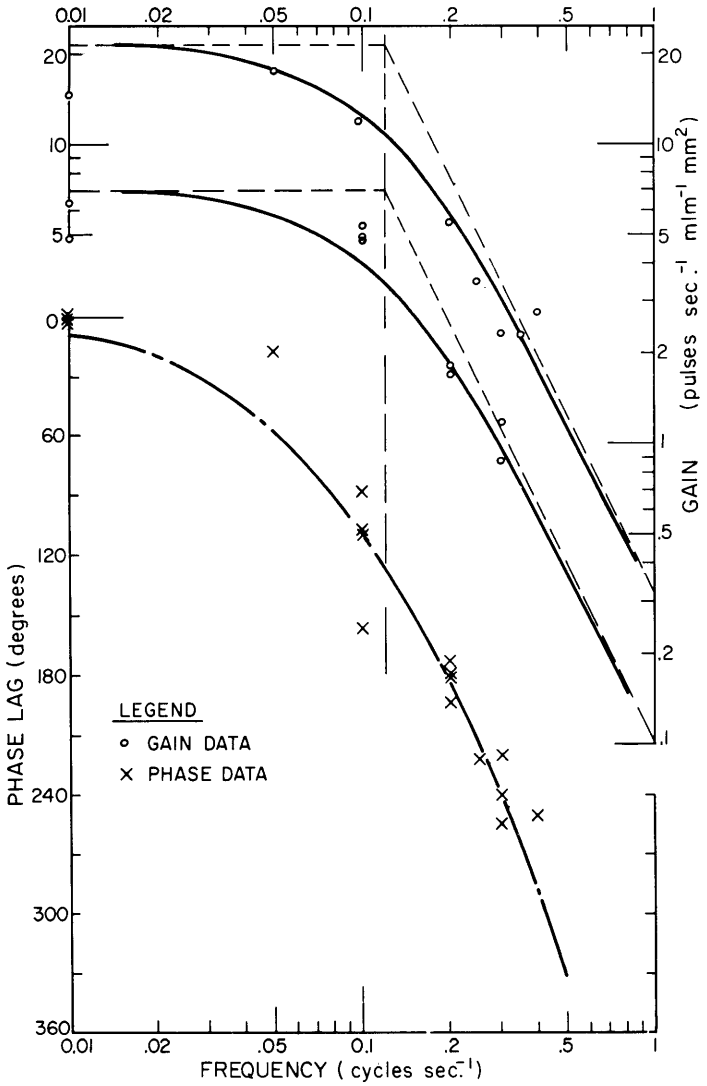

Fig. XXI-23. Bode plot comparing population and single-unit response from same preparation. Curves and asymptotes are derived from the single-unit transfer function and applied to single-unit data. Same transfer function but with gain increased threefold is applied to population response is assumed to be composed only of three B-fiber units. Fit of curves to experimental points is strong evidence for a very limited number of light-responding units.

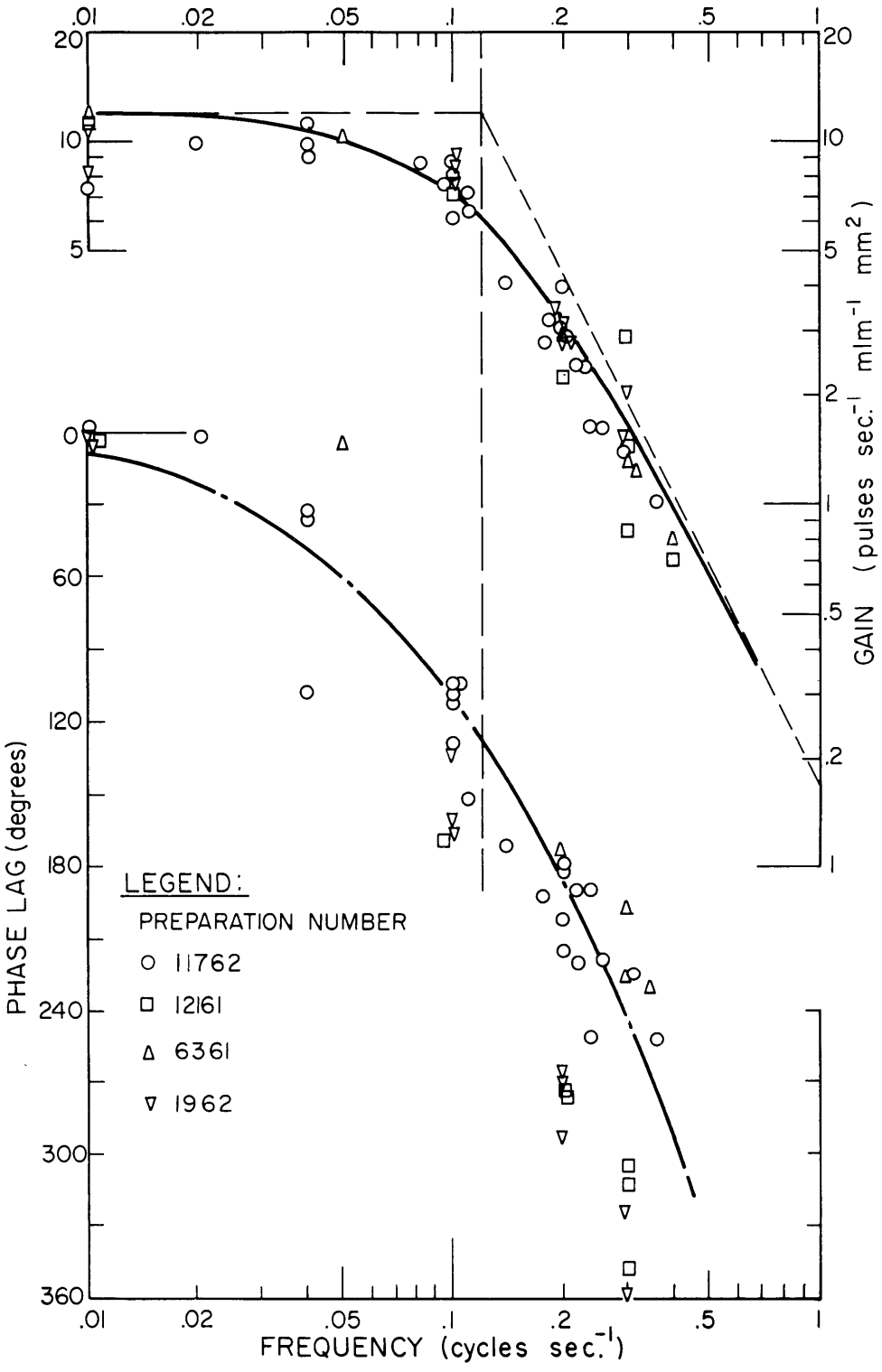

Fig. XXI-24. Composite Bode diagram from 4 different preparations. This shows considerable similarity of response frequency and phase characteristics from animal to animal. Gains were more variable, however (6, 7, 7, 12) and were normalized to 12 here. Temperature (19° C) and other experimental conditions were held constant. Variation between crayfish may account for differing gains.

c. Nonlinearities

Although it is clear that 80-90 per cent of the power in the waveform of the response to sinusoidal stimuli is contained in the fundamental frequency – thus linear analysis is implicitly justified – interesting nonlinearities appear consistently in our data. An asymmetry in rate of change of pulse frequency can be seen in Fig. XXI-25. Pulse-rate rise is more rapid than pulse-rate fall and produces the sawtooth waveform. This effect is more prominent with large signal inputs.

Saturation is another important and, as shown in Fig. XXI-26a, is more prominent at large signal-input levels. This figure shows output amplitude as a function of input amplitude at one frequency, 0.08 cps. Two scales are used, ΔF vs ΔI, and $\Delta F/\bar{F}$ vs $\Delta I/\bar{I}$ for normalized units, where ΔF is change in frequency of nerve pulse rate and

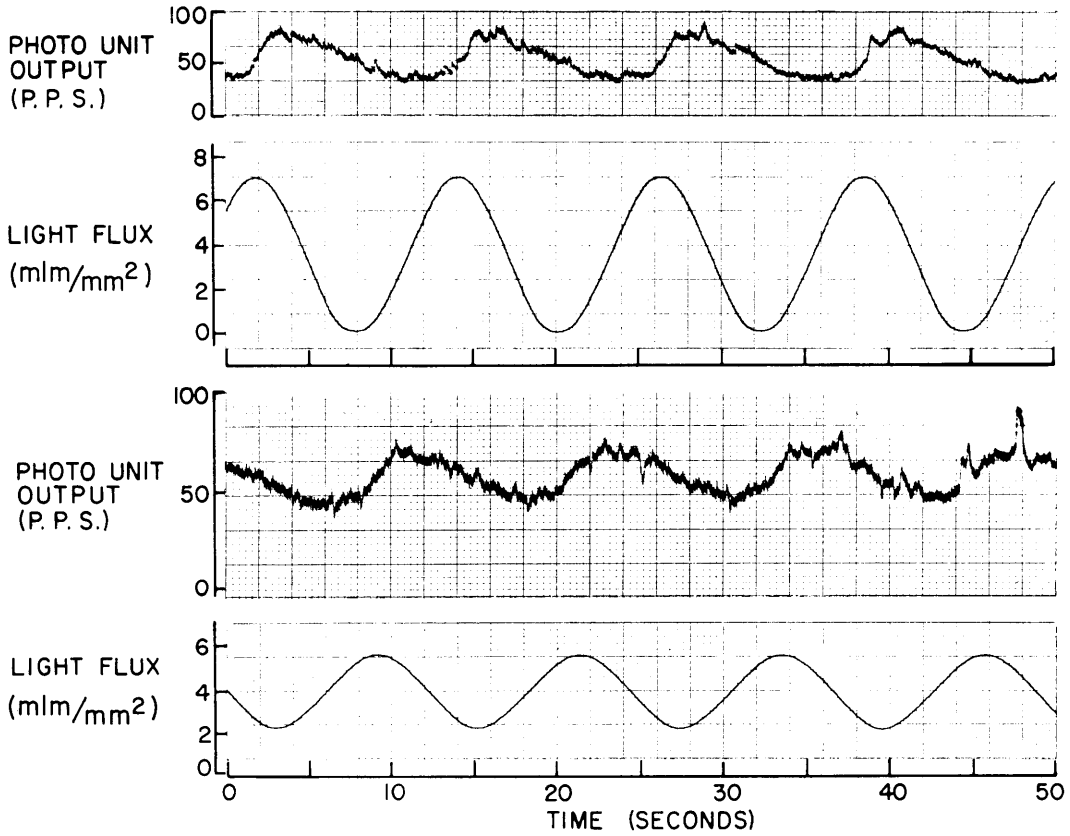

Fig. XXI-25. Sawtooth nonlinearity in single-unit response. Upper pair of traces shows larger signal-driving function and response; lower pair is smaller signal excitation and response. Scale of response is doubled in lower trace. Less saw-tooth asymmetry is apparent in smaller-signal operating conditions. G = 7.6 and 90° for small signal, and G = 6.6 and 72° for larger signal; thus nonlinearity produces apparent relative phase lead and some decrease in gain.

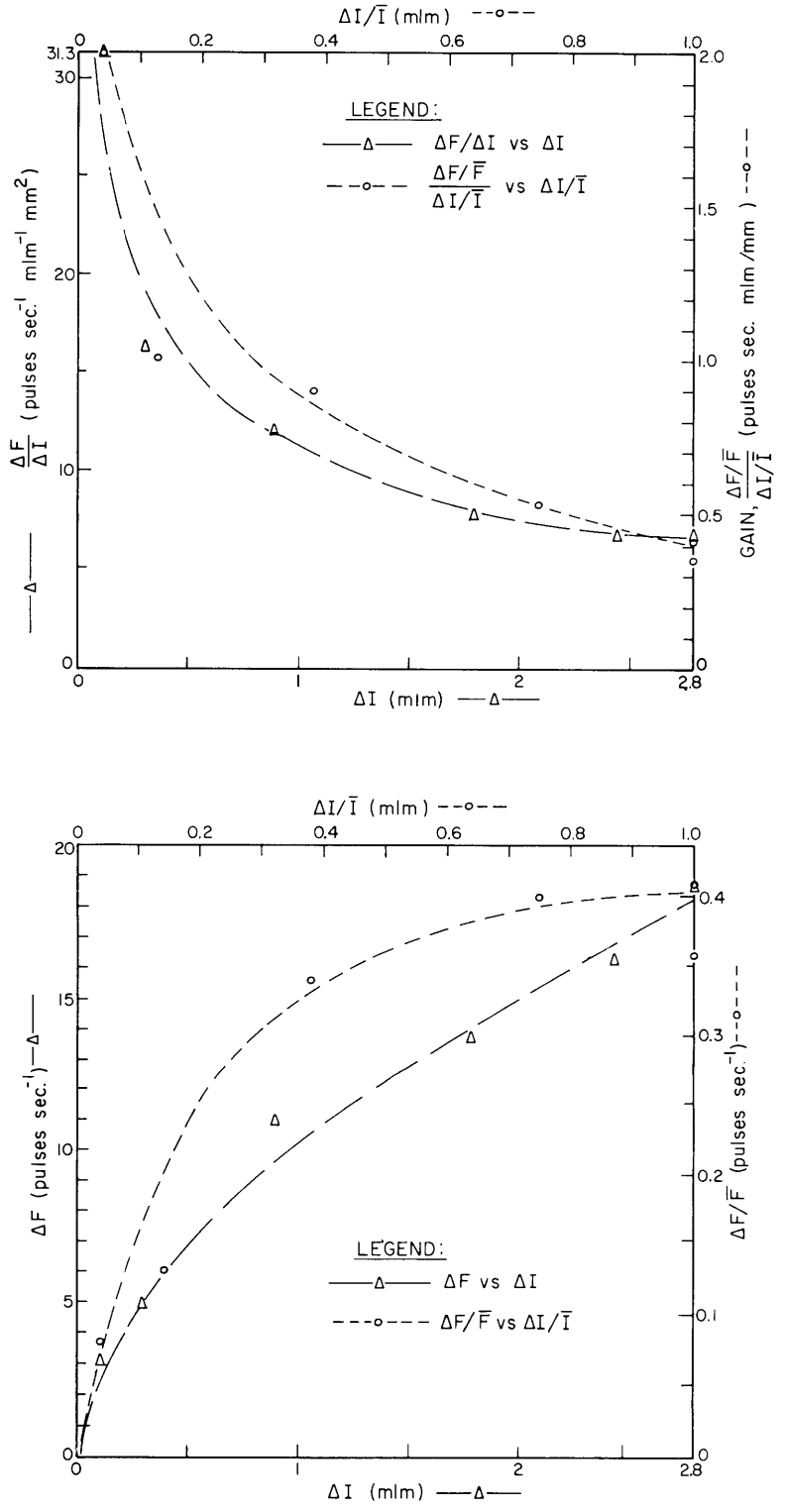

Fig. XXI-26. Saturation nonlinearities. All data obtained at 0.08 cps. (a) Output as a function of input. (b) Gain as a function of input. Left and bottom scales are not normalized; right and top scales are normalized. Saturation is similar in both scales.

F is mean pulse rate. Similarly, ΔI is change in light flux/unit area, and $\bar{I}$ is mean light flux/unit area. In Fig. XXI-26b gain is displayed as a function of input amplitude; normalized values and scales are also furnished. In the particular experiment shown, the curves are quite similar. However, if ΔI is kept constant and $\bar{I}$ varied, clear evidence is obtained which indicates the necessity for normalization. This is merely an instance of the well-known Weber-Fechner law, which states that $\Delta I/\bar{I}$ or the fractional change of stimulus energy is the effective stimulus. The experiments reported here have been designed with constant I and small ΔI to avoid these complications.

The inclusion of the material dealing with asymmetry, saturation, and scale-compression nonlinearities is for the purpose of providing quantitative estimates of these minor limitations on the linear analysis leading to the transfer function.

4. Discussion

In the analysis of biological systems, it is clearly useful to pass beyond a simple, loose, naturalistic description to one that has logical, quantitative vigor and is capable of being tested for internal consistency. Particularly in neural systems, for which information coding is, after all, the prime function, quantitative relationships must be developed. It is commonplace to observe that nature shows nonlinear system behavior. Nontheless, piecewise approximation to a nonlinear system may be successfully carried out by small-signal linearization techniques, as our studies indicate. The usefulness of sinusoidal inputs and Fourier methods of function synthesis have been confirmed and a concise mathematical description developed. The divergence from a pure linear system may be examined by partial exploration of the extreme dynamic range of both mean light levels and modulation amplitudes. It is important to note, however, that significant departures from the linear equation occur in gain characteristics and not the phase portion of the frequency-response curves, and suggest no-memory type of nonlinearities. A more complete mathematical description may be stated only after considerable delineation of the nonlinear departures.

H. T. Hermann, L. Stark

References

1. J. W. S. Pringle and V. J. Wilson, The response of a sense organ to a harmonic stimulus, J. Exp. Biol. 29, 229 (1952).

2. J. J. Groen, O. Lowenstein, and A. J. H. Vendrik, The mechanical analysis of the responses from the end organs of the semicircular canal in the isolated elasmobranch labyrinth, J. Physiol. 117, 320-346 (1952).

3. T. W. M. Roberts, Discussion of speculations on servo control of movement, The Spinal Cord, edited by J. L. Malcolm and J. A. B. Gray (J. and A. Churchill, Ltd., London, 1953), pp. 255-258

4. L. Stark, Transfer Function of the Biological Photoreceptor, Air Force Technical Report WADC TR59-311, August 1959, pp. 1-22.

5. L. Stark and H. T. Hermann, The transfer function of a photoreceptor organ, Kybernetik 1, 124-129 (1961).

6. H. T. Hermann, L. Stark, and P. A. Willis, Instrumentation for processing neural signals, EEG Clin. Neurophysiol. (in press).

7. H. T. Hermann and L. Stark, Prerequisites for a photoreceptor structure in the crayfish tail ganglion, Anat. Record (in press).

8. W. R. Utall and H. Kasprzak, The caudal photoreceptor of the crayfish: Adaptation and the luminosity function, Abstracts of Biophysical Society Meeting, Washington, D.C., February 1962 (No. TE 7, 1962).

9. A. R. Cox and W. L. Smith, On the superposition of renewal processes, Biometrika 41, 91-99j(1954).

10. H. T. Hermann and L. Stark, Random walk response of the crayfish, Quarterly Progress Report No. 61, Research Laboratory of Electronics, M.I.T., April 15, 1961, pp. 230-234.

C. OPTOKINETIC NYSTAGMUS IN MAN

A previous report[1] described our experimental arrangement and indicated that the slow or compensatory phase was grossly inadequate to compensate for field velocity. We have continued these studies with some variables fixed (four vertical stripes visible in a 40° horizontal and 70° vertical field, constant stripe intensity, and light/dark ratio (0.15), but with varying field velocity and fixation conditions. A bright 0.1°-angle light spot was projected as the fixation point or was extinguished for "no fixation point" conditions. With the light spot extinguished the subject could only voluntarily direct his eyes forward, since the screen was the only object in the visual field.

Our main conclusion is summarized in Fig. XXI-27, which shows the angular velocity of the slow or corrective phase of optokinetic nystagmus as a function of field velocity (ω_f). It is clear that at $\omega_f = 40°$ per second only 15 per cent of the image velocity is compensated for, or corrected. Data from a control tracking experiment show that the eye movement-control system is able to track accurately at this velocity. Even less compensation (4 per cent) is obtained when a bright fixation point enables the fixation response to compete with the pursuit stabilized-image system for control of the eye musculature. Introduction of a fixation point increases the duration of the slow phase movement, decreases the rate and final angle of excursion, and decreases dependence upon field velocity. The fixation point also reduces the angular field velocity at which fusion occurs (40° per second vs 60° per second), as shown in Fig. XXI-28.

The fast phase of the nystagmus is considered to be the action of the fixation response which repositions the fovea of the retina upon the center of the image field. Figure XXI-29 shows that the mechanism controlling this movement is fairly accurate. The velocity of the saccadic jump is highly correlated with the angle of jump, since the duration of the saccadic movement is rather constant (40-50) msec).

It should be stated, however, that the experimental data reported on here are somewhat variable and that it is usually necessary to average a number of responses to arrive at consistent results.

It seems that optokinetic nystagmus is the result of competition between two control systems for eye movement – (a) the pursuit stabilized retinal-image velocity control, and (b) the saccadic fixation position control. It is clear that the pursuit

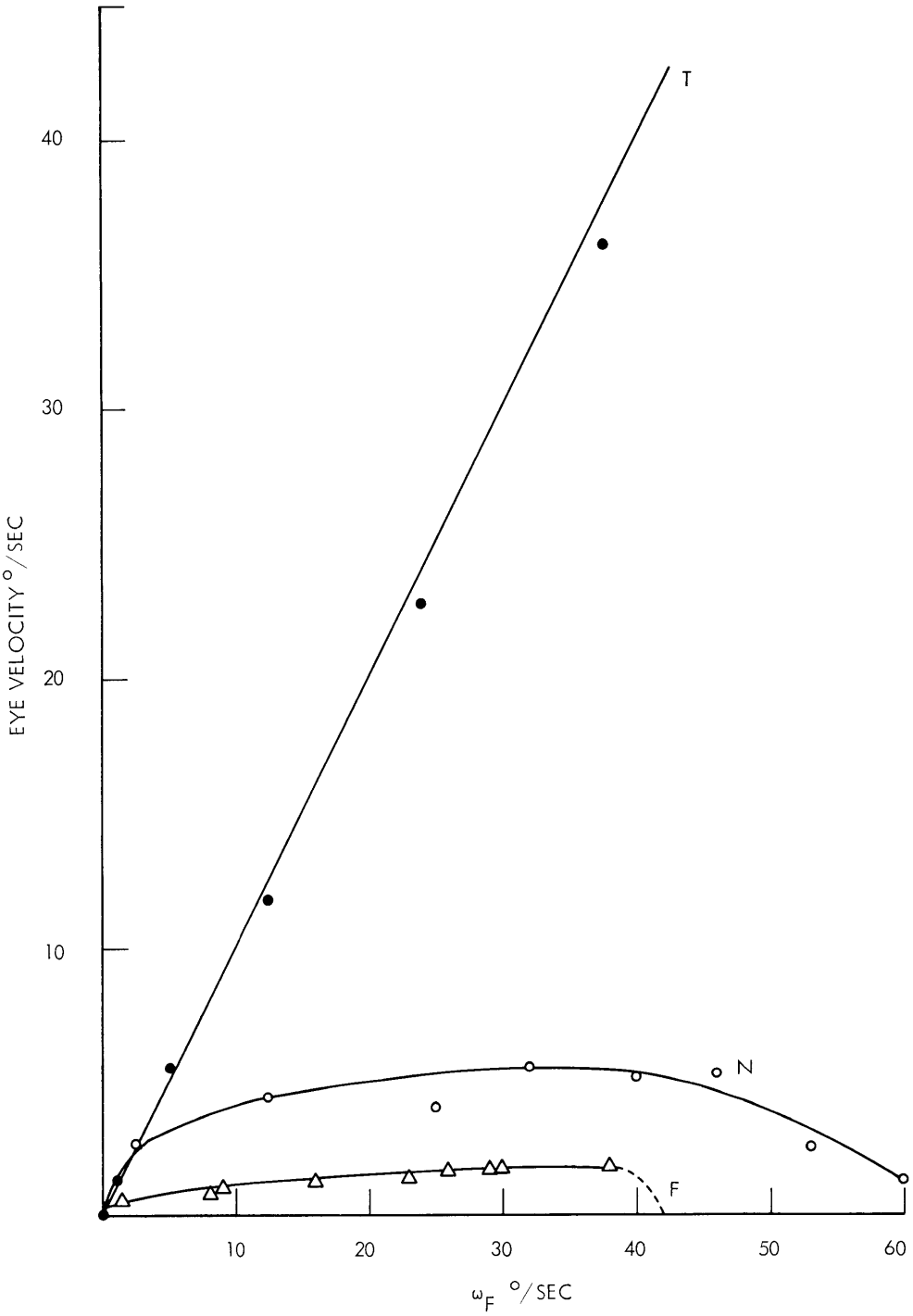

Fig. XXI-27. Dependence of optokinetic nystagmus upon field velocity. N indicates "no fixation point" nystagmus; F, the effect of a fixation point; and T, a control tracking experiment showing ability of the retina eye muscle system to perceive and rotate the eyeball at input velocity.

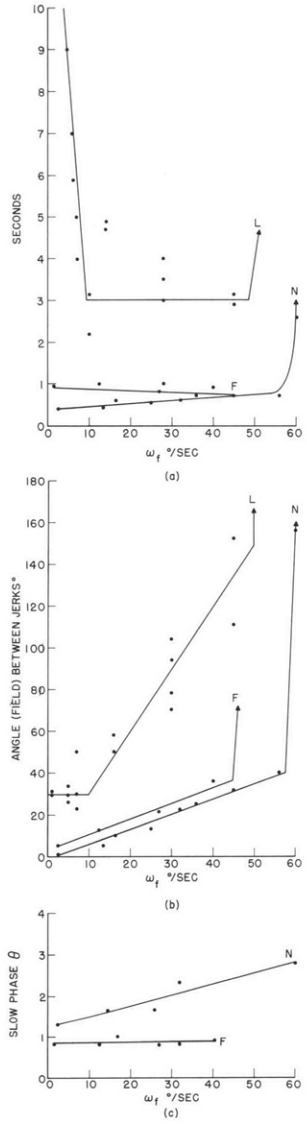

Fig. XXI-28. Field velocity **effects on** optokinetic nystagmus. F and N, same as in Fig. XXI-27; L **represents** land-crab data from a previous report[2] for comparison with human material. (a) Duration of slow phase (time between jerks); (b) Angle (field) between jerks; and (c) Maximum angle (slow phase) before saccadic return.

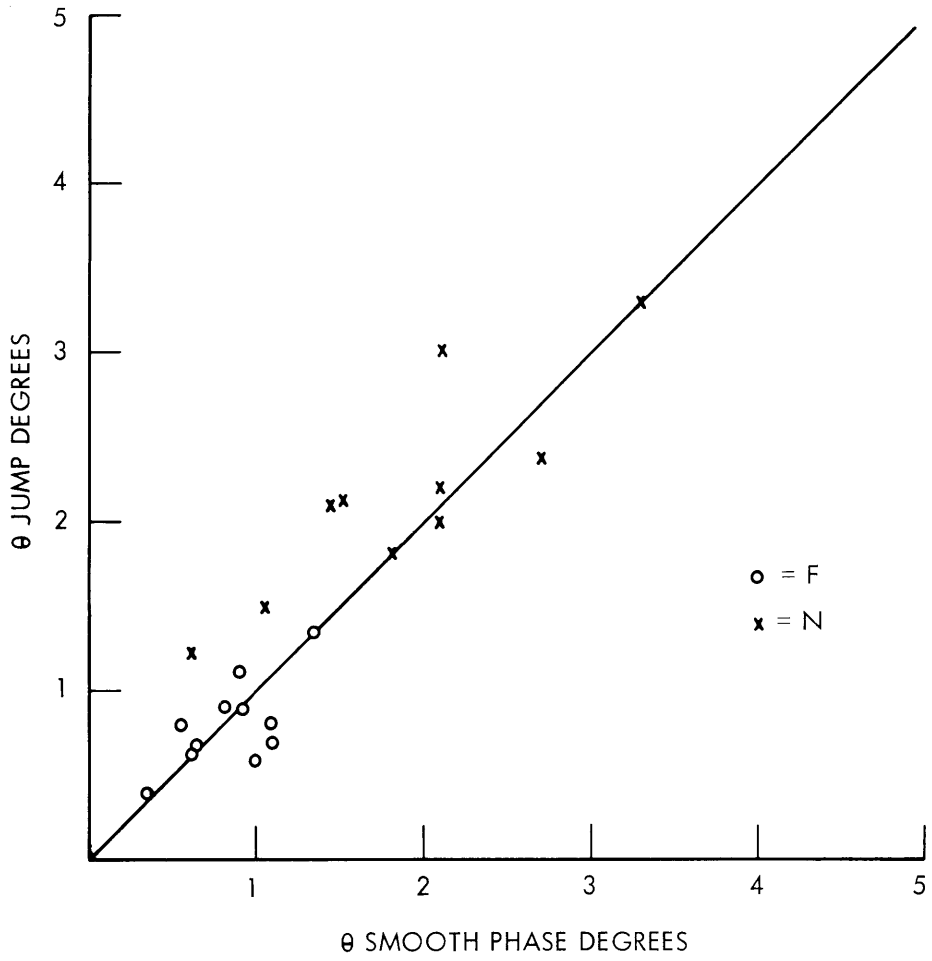

Fig. XXI-29. Angle of jerk as a function of angle of slow phase showing excellent compensation for return to fixation. Circles, with fixation point; crosses, without fixation point.

system is not effectively reducing error, but evidently is working at some minimal level, while the fixation response is accurately compensating for disturbances introduced by the minimally-operating velocity system.

G. P. Nelson, L. Stark

References

1. L. Stark and G. Nelson, Optokinetic nystagmus, Quarterly Progress Report No. 64, Research Laboratory of Electronics, M.I.T., January 15, 1962, pp. 326-328.

2. L. R. Young, Experiments on the visual system of the land crab, Quarterly Progress Report No. 65, Research Laboratory of Electronics, M.I.T., April 15, 1962, pp. 247-251.

D. A SAMPLED-DATA MODEL FOR EYE-TRACKING MOVEMENTS

The application of servoanalysis to the study of human eye movement control in a tracking task has yielded a new type of mathematical model for a biological servomechanism. Experiments on the ability of subjects to move their eyes in order to follow the horizontal motion of a target led to three basic principles on which the model was based. First, the predictability of the target signal was shown to have a profound effect on the system's ability to track continuous and discontinuous target motions; thus the system is classified as an input-adaptive controller. Second, the saccadic and pursuit systems were shown to be functionally separate, with the former acting as a position tracker and the latter as a velocity tracker. Third, the eye movement tracking characteristics in the nonpredictive mode were shown to be of a discrete nature: thus a noncontinuous model is required for adequate description.

A sampled-data model for nonpredictive tracking has been developed, and this model successfully predicts the major characteristics of the biological servomechanism, both for transient responses and in the frequency domain. In addition to describing normal tracking, the model predicts the observed changes in tracking characteristics and the limits of stability as the effective visual feedback is varied.

1. Introduction

The eye movement control system is an interesting human servomechanism employing voluntary, as well as involuntary, control to direct the line of gaze at a moving target. Previous mathematical descriptions,[1-4] in which transient response, as well as frequency characteristic, have been considered, have failed to predict the over-all system behavior. Experimental evidence indicates three characteristics of the system that cannot be overlooked in developing a model. (a) The predictability of the target signal has been shown to affect the mode of operation in tracking continuous and discontinuous target motions.[5] (b) The saccadic and pursuit mechanisms have been shown to be functionally separate, with position errors being corrected by fast saccadic jumps, and velocity errors by smooth pursuit movements.[6] (c) It can be demonstrated that the discrete nature of the system in tracking nonpredictable target motions is inconsistent with a continuous mathematical model and requires a sampled-data model for adequate description.[7] Support for the sampled-data nature of the tracking system includes the experimental evidence given in this report.

a. Pulse Response

The eye-movement response to a pulse of target position is characterized by a delay preceding the saccadic response, and a refractory period, approximately equal to the delay, preceding the saccade which returns the eye to its initial position. Thus for a pulse width that is much less than 180 msec, the eye responds to the pulse after the

target has returned and remains in the displaced state for approximately 180 msec before returning. The output of a linear continuous system with a cascade delay would be a delayed, possibly distorted, pulse of the same width as the target pulse, and could be described as the superposition of two equal and opposite step responses displaced in time by the pulse width. Superposition obviously cannot be applied in this situation. The result is, however, similar to that of a sampled-data system with a zero-order hold, and permits changes of the output variable to occur only at sampling instants.

b. Open-Loop Step Response

When the visual feedback loop is effectively opened by introducing unity external feedback from eye position to target position, the movements of the eye cause no change in the error signal observed at the retina. Under these conditions, a step of target position, corresponding to a step of observed error, induces a regular series of equal saccadic jumps, with a constant time of one refractory period between the jumps. Just as the pulse response, this result indicates that saccadic movements can be made no closer together than some critical period, regardless of the error that is observed.

c. Discrete Changes in Pursuit Velocity

Upon close inspection of the records of eye movements during continuous random target motions, the smooth pursuit motions are a series of constant-velocity segments. The large discrete changes in velocity occur at intervals of 100-200 msec and are often accompanied by a simultaneous saccadic movement. The discreteness of the pursuit movements is clearly shown in the response to parabolic inputs. The observed tracking record and its derivative indicate that the velocity increases in a stepwise manner and that all of the saccadic movements are in the direction of the target motion; thus the position lag resulting from the pursuit motion with constant-velocity segments is corrected.

d. Peak in the Frequency Response

Inspection of the tracking records for continuous unpredictable inputs reveals a considerable number of saccadic jumps separated by one refractory period (~ 180 msec). Bode plots resulting from Fourier analysis of the output bear out this observation by showing a sharp peak in gain of approximately 6 db at 2.5-3.0 cps and indicating the presence of a great deal of energy with the half-period of 160-200 msec. The sampling process transforms an input spectrum F(s) into an output spectrum

$$\frac{1}{T} \sum_{n=1-\infty}^{\infty} F(s+nj\omega_o).$$

Here, T is the sampling interval, and ω_o the sampling angular frequency. Clearly, a peak in the output spectrum occurs first at $\omega = \omega_o/2$. If a sampling interval of 180 msec is assumed, then the sampling frequency would be 5.55 cps and the first peak in the output energy spectrum would occur at 2.8 cps, which is in agreement with experimental data. Furthermore, since the Nyquist sampling theorem states that at least 2 samples per period are necessary for any reconstruction of data from samples, the tracking ability of a sampled-data model would be nonexistent for target frequencies higher than one-half the assumed sampling frequency. This fact is in agreement with our experiments which show no tracking of input frequencies greater than 2.5-3.0 cps.

e. Dependence of Accuracy on Prediction

During a square-wave tracking experiment in which the subject predicts the change in target position and moves his eyes before the target moves, he tends to overshoot or undershoot the desired position by a considerable percentage. This observation is reasonable when one considers that this predictive movement is made from memory of the anticipated target position and without the aid of any visual reference. Of particular interest, however, is the case of slight prediction, in which the saccadic movement takes place after the target change, but less than 150 msec after that target step. Since the response takes place in less than a minimum reaction-time delay, the initiation of the movement command must occur before the target step, although the actual saccade does not take place until the target has reached its new position. If it were possible for the eye-movement command, once initiated, to be modified by the presence of a new visual reference before the saccade takes place, then the responses occurring from 0-150 msec after the target step should be performed with the same accuracy as those taking place after a full normal reaction time. Since the experimental results show the same inaccuracies for delays of less than one reaction time as for true predictions, we conclude that once a saccadic movement command is initiated, no new visual information can alter that particular command. This conclusion is consistent with the operation

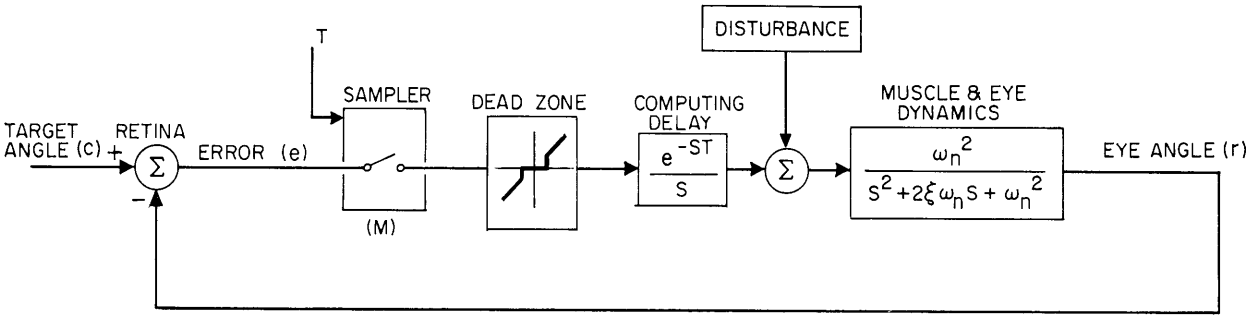

Fig. XXI-30. Sampled-data model for the saccadic system.

of a sampled-data system that takes in information only at the sampling instants.

2. Sampled-Data Model for Saccadic Tracking

In the model shown in Fig. XXI-30, the error angle (e) between the desired angle of gaze (c) and the actual eye position (r) is detected at the retina. This error is sampled by an impulse modulator (M) at sampling intervals, T, where T is the average refractory period for saccadic movements (~0.2 sec). The synchronization of the modulator must be assumed to be set to coincide with the beginning of a target motion, if the eye had made no saccadic jumps during the previous 0.2 sec. Each error sample impulse is delayed by one reaction time and integrated to give a step command indicating the desired change in eye position that is necessary to bring the eye to the position that had been the desired position one reaction time previously. (Z is defined as a pure delay of T seconds, or $Z = e^{sT}$.) This step is then filtered by the dynamic response of the extraocular muscles and the eye loading them, to yield an actual eye-position movement exhibiting finite rise time and possible overshoot. A second-order model for saccadic movements serves to demonstrate that the details of the individual movements can be neglected in considering the over-all characteristics of the sampled-data model for the eye-movement control system.

The parameters published by Westheimer[4] (ω_n = 240 rad/sec = 0.7) indicate that at the next sampling interval, 0.2 sec after the onset of saccade, the eye position will have settled to within at least $e^{-33.6}$ of its final value. (By final value is meant the steady-state eye position resulting from that one saccade. If this is not the desired eye position and the error lies outside the foveal dead zone, it will be corrected by a secondary saccadic movement at the next sampling interval.) Since this disparity is less than the errors in fixation resulting from miniature eye movements (designated as disturbances in Fig. XXI-31) or errors in computation of the desired amplitude of

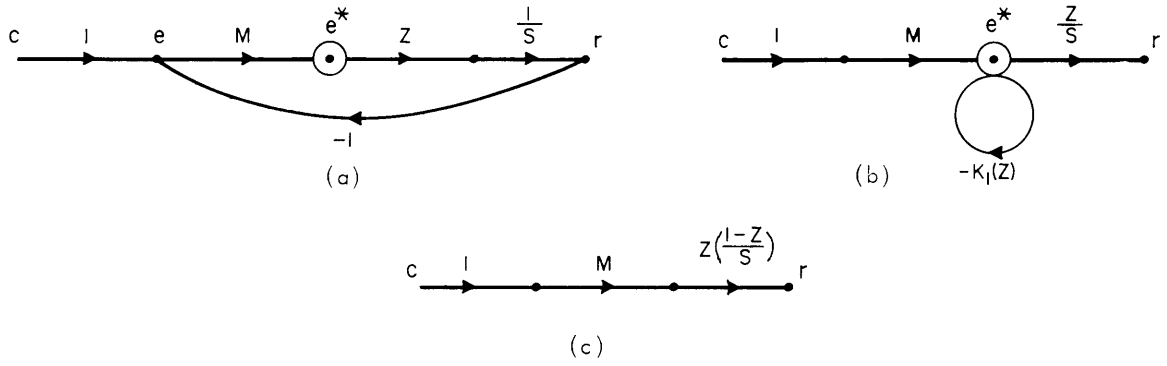

Fig. XXI-31. Simplified flow chart for the saccadic system.

the saccade, its effect on the observed error at the next sampling instant can be neglected. For the sake of simplicity of presentation, therefore, the muscle and eyeball dynamics will be ignored in the rest of this report. It must be remembered that when the simplified model indicates a discrete change in eye position, the actual eye position predicted would be a typical saccadic movement.

With this simplification, and the effect of disturbances and the 1.0° dead zone neglected, the saccadic system model for discrete position tracking reduces to the flow chart of Fig. XXI-31a. By isolating the discrete data mode e^*, the flow chart can be redrawn as in Fig. XXI-31b, in which $-K_1(z)$ represents the discrete transfer function of the open loop.

$$K_1(z) = z\left(\frac{1}{S}\right)^*$$

$$K_1(z) = \frac{z}{1 - z}$$

$$\frac{1}{1 + K_1(z)} = 1 - z.$$

The flow chart is finally reduced to that of Fig. XXI-31c, showing that the output of the saccadic system alone is

$$R(s) = C(s)^* \, z\left(\frac{1-z}{s}\right),$$

which can be recognized as a delayed zero-order hold.

3. Sampled-Data Model for the Pursuit System

Whereas saccadic movements serve to center the target image on the fovea, the purpose of the pursuit system is stabilization of the target image on the retina by keeping the angular velocity of the eye equal to that of the target for target velocities less than 25-30° per second. It is reasonable to describe the pursuit system as a sampled-data velocity tracker.

The block diagram of Fig. XXI-32 represents one way in which this velocity tracker could work. As in the saccadic model, the error between the desired and actual eye position is sampled every reaction time T, which may or may not be the same sampling period as for the saccadic model. The error rate is estimated from the difference between the past two error samples divided by the sampling interval T. This error-rate estimate is the desired change in the eye velocity and its integral is the eye velocity attributable to the pursuit system. The first limiter reflects the fact that the pursuit does not attempt to follow the high velocities present in discontinuities of the target position, and the second limiter indicates that the pursuit velocity saturates at 25-30° per second. The output of the second limiter will be a sequence of ramps of eye position

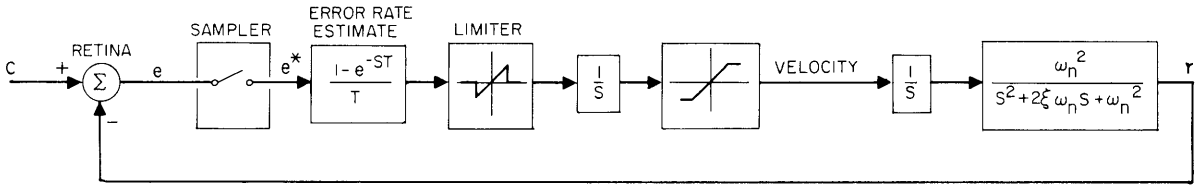

Fig. XXI-32. Sampled-data model for the pursuit system.

at the desired velocity. The effect of the muscle and eye dynamics is to smooth out the discontinuities in velocity and also to introduce a small constant steady-state error between the desired ramp and the actual output.

Since the eyeball dynamics have no effect on the over-all closed-loop characteristics of the sampled-data pursuit model, these dynamics will be neglected in this presentation.

The flow chart for the simplified pursuit model with the nonlinearities removed is shown in Fig. XXI-33a. As before, the flow chart is reduced by considering all inputs and outputs at the discrete data point e^*. In Fig. XXI-33b the z transform of the open-loop transfer function is denoted by $-K_1(z)$:

$$K_1(z) = (1-z)\left(\frac{1}{Ts^2}\right)^*$$

$$K_1(z) = \frac{(1-z)}{T}\left(\frac{Tz}{(1-z)^2}\right)$$

$$K_1(z) = \frac{z}{1-z}.$$

Since

$$\frac{1}{1+K_1(z)} = (1-z),$$

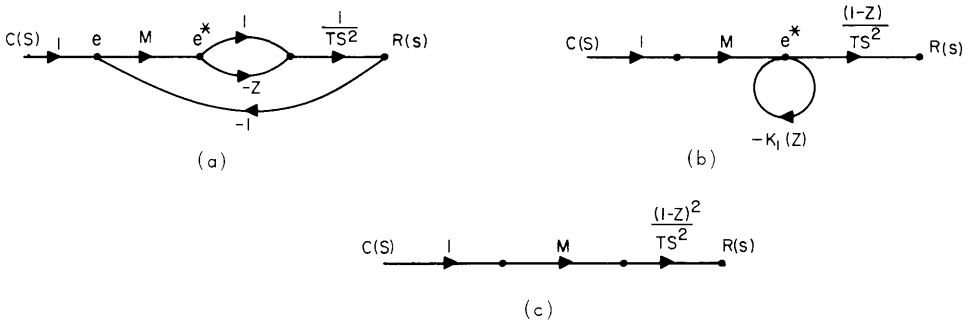

Fig. XXI-33. Simplified flow chart for the pursuit system.

the sampled-data velocity tracker finally reduces to the flow chart of Fig. XXI-33a. For the pursuit system alone, eye position would be given by

$$R(s) = C(s)^* \frac{(1-z)^2}{Ts^2}.$$

This equation may be rewritten to clarify the operation of the velocity tracker.

$$R(s) = C(s)^* \left(\frac{1-z}{T}\right) \left(\frac{1-z}{s}\right) \left(\frac{1}{s}\right);$$

this equation states that the target position is sampled and its velocity is estimated by the first difference $\left(\frac{1-z}{T}\right)$. Since old data are used to calculate present velocity, this term accounts for the delay in the pursuit system. The term $\left(\frac{1-z}{s}\right)$ is a zero-order hold, keeping the output velocity constant between sampling instants, and the integrator yields the eye position resulting from this velocity.

4. Complete Sampled-Data Model

Since the refractory period is not a deterministic function, the simplifying assumption will be made that T is a constant sampling interval equal to the mean experimental value for the saccadic system and also for the pursuit system.

Since the average refractory period for velocity changes is equal to or slightly less than that for saccadic movements for any one subject tested, the sampling intervals will be assumed to be equal for the pursuit and saccadic systems. Furthermore, the error sampling for the pursuit and saccadic loops will be assumed to be synchronous, both starting with the initiation of any significant change in target position or velocity following a quiescent period. Under these simplifying assumptions a single sampler, or impulse modulator, may be used to furnish error samples for the saccadic and pursuit tracking loops.

The pursuit loop, as a velocity tracker, should use estimates of error rate to keep the eye velocity equal to the target velocity, with corrections coming in as regularly spaced ramps of eye position. It is important that the pursuit model not try to null out any apparent smooth error rate resulting from a step change in error during a saccadic jump.

The function of the first limiter in the pursuit system block diagram was to force the pursuit system to ignore all very rapid changes in the observed error. These error discontinuities may occur either from target discontinuities or from the step changes in eye position caused by the saccadic system. This nonlinear element has been removed, and its function retained in the following manner. The pursuit loop in the model is considered open at the time of (or at the sampling instant following) any target velocity greater than 30° per second. This artifice is easily managed in considering

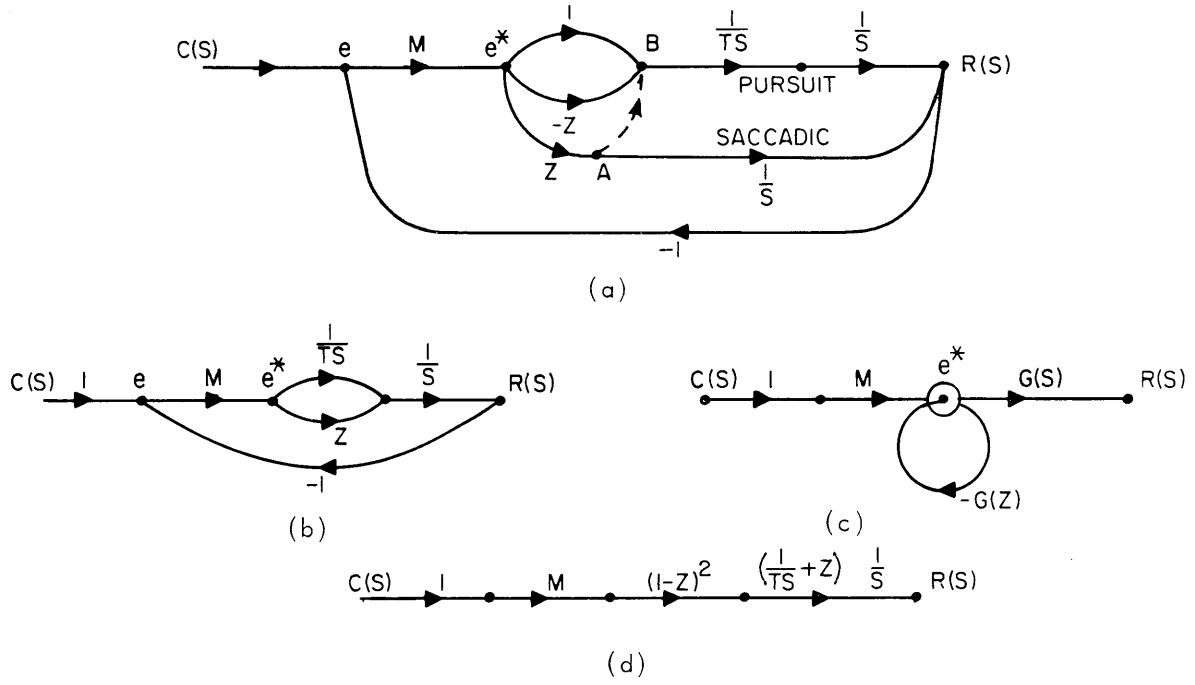

Fig. XXI-34. Complete sampled-data model flow chart.

random target inputs. The other component of error discontinuity, resulting from a saccadic movement, may be prevented from stimulating the pursuit loop by introducing an extra cross-coupling branch (from A to B) between the saccadic and pursuit models.

The equivalent flow chart of Fig. XXI-34b is identical with the purely saccadic sampled-data model, except for the branch with transmission 1/Ts which represents the contribution of the pursuit system. This is the branch target. The further reduction of the flow chart is done in the usual manner. In Fig. XXI-34c the forward transmission is

$$G(s) = \left(\frac{1}{Ts} + z\right)\frac{1}{s} .$$

The sampled transfer function around the closed loop is

$$G(z) = \left[\frac{1}{Ts^2} + \frac{z}{s}\right]^*$$

$$G(z) = \frac{2z - z^2}{(1-z)^2} .$$

This contributes the forward-loop transmission

$$\frac{1}{1 + G(z)} = (1-z)^2 ,$$

and the resultant flow chart is as shown in Fig. XXI-34d.

Thus for the integrated sampled-data model with both the pursuit and saccadic systems functioning, the predicted eye position is given by

$$R(s) = C(s)^* (1-z)^2 \left(\frac{1}{Ts} + z\right) \frac{1-z}{s}.$$

Written in another form, this equation becomes

$$R(s) = C(s)^* \left[(1-z)\, z\left(\frac{1-z}{s}\right) + \left(\frac{1-z}{T}\right)\left(\frac{1-z}{s}\right)\left(\frac{1}{s}\right)\right].$$

The first term in brackets is a delayed zero-order hold on the first difference of target samples. This represents the action of the unit delay in velocity changes by the pursuit system.

The second term in brackets, $\left(\frac{1-z}{T}\right)\left(\frac{1-z}{s}\right)\left(\frac{1}{s}\right)$, is the same as that encountered in the simple pursuit model. It represents the function of the velocity tracker in using the first difference of target samples to estimate the velocity, holding this in a zero-order hold, and then contributing ramps of target position equal to the integral of this velocity.

5. Model and Experimental Transient Responses

a. Step Response

Since this involves a discontinuity of target position, the pursuit loop is initially open

$$C(s) = \frac{A}{s}$$

$$R(s) = \left(\frac{A}{s}\right)^* z\left(\frac{1-z}{s}\right)$$

$$R(s) = \frac{Az}{s}$$

The response is a delayed step, in agreement with experiments. (See Fig. XXI-35.)

b. Pulse Response

Once again, the pursuit loop is open at the discontinuities (and the sampling instant following a discontinuity occurring between sampling instants). For a pulse width τ, with $\tau < T$,

$$C(s) = \frac{A}{s}(1-e^{-\tau s})$$

$$C(z) = A$$

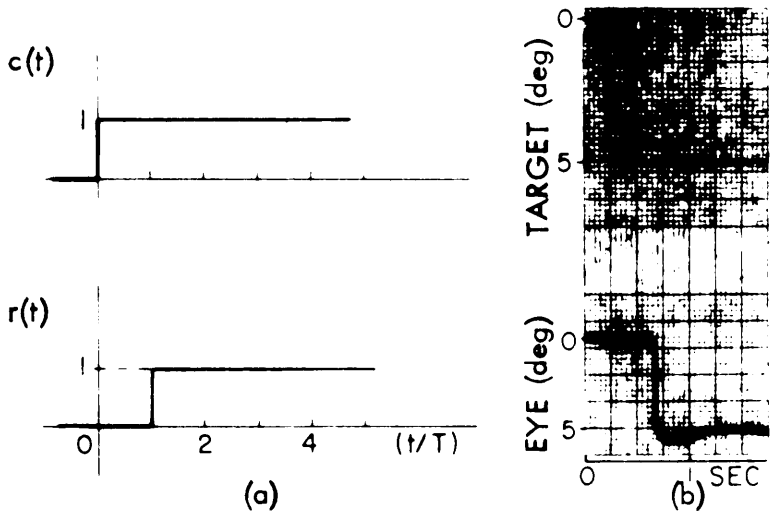

Fig. XXI-35. Step response. (a) Model; (b) Experimental.

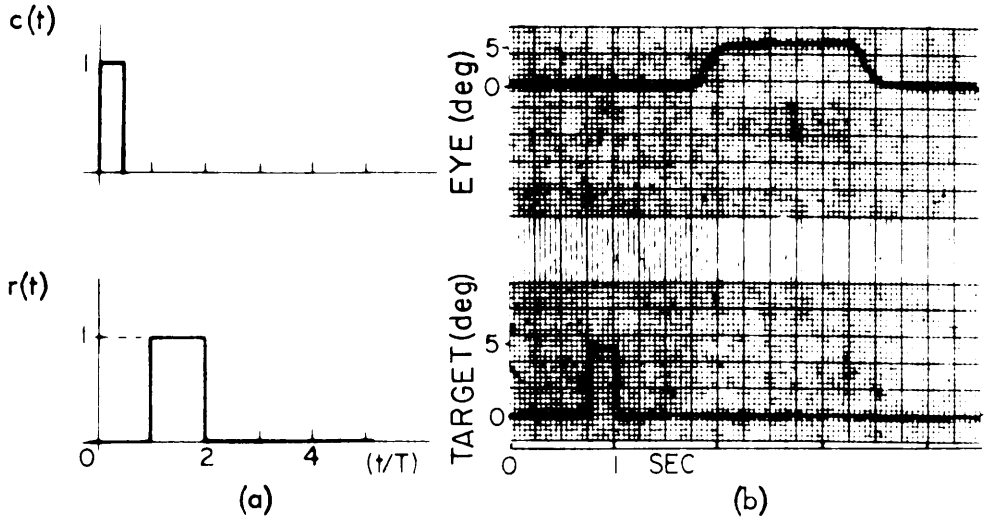

Fig. XXI-36. Pulse response. (a) Model; (b) Experimental.

$$R(s) = Az\left(\frac{1-z}{s}\right).$$

The response is a delayed pulse of width T (see Fig. XXI-36).

c. Ramp Response

$$C(s) = \frac{A}{s^2}$$

$$C(z) = \frac{ATz}{(1-z)^2}$$

$$R(s) = \frac{ATz}{(1-z)^2}\ (1-z)^2\left[\frac{1}{Ts^2} + \frac{z}{s}\right]$$

$$R(s) = A\left[\frac{z}{s^2} + T\frac{z^2}{s}\right]$$

The response is a ramp of slope A delayed by T plus a step AT occurring at t = 2T. (See Fig. XXI-37.)

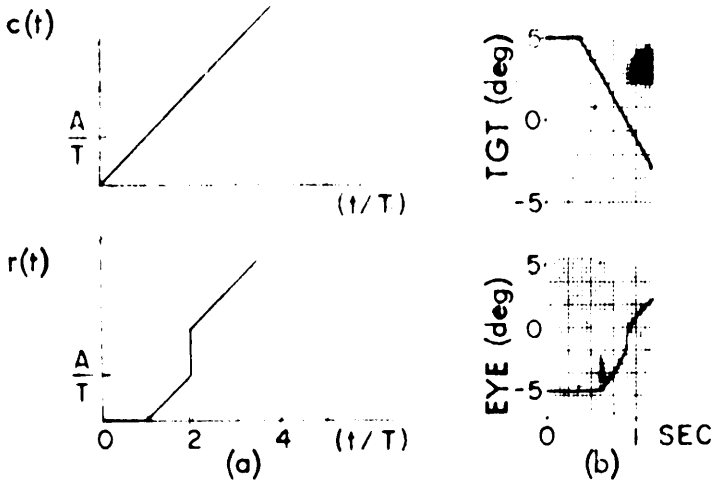

Fig. XXI-37. Ramp response. (a) Model; (b) Experimental.

d. Step-Ramp Response

The response to a target movement consisting of a step to one side followed by a constant velocity in the opposite direction may be treated by superposition of the step response, in which the pursuit loop is inactive, and the ramp response involving the complete system, as discussed above.

$$C(s) = \frac{-A}{s} + \frac{B}{s^2}$$

$$R(s) = \frac{-Az}{s} + B\left[\frac{z}{s^2} + T\frac{z^2}{s}\right]$$

This transient response is plotted in Fig. XXI-38a, and an experimental result is shown in Fig. XXI-38b.

e. Saw-Tooth Response

A single saw-tooth waveform of duration KT has the Laplace transform

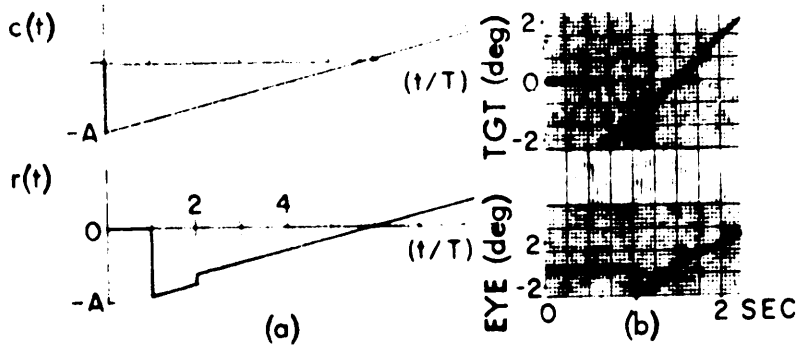

Fig. XXI-38. Step-ramp response. (a) Model. (b) Experimental.

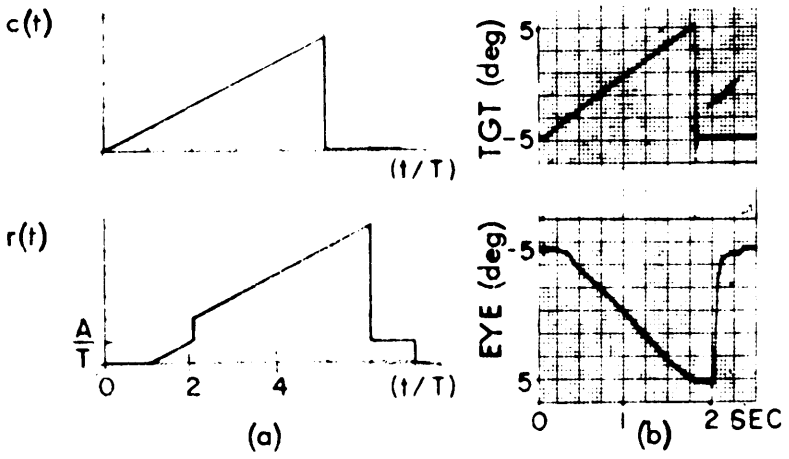

Fig. XXI-39. Saw-tooth response. (a) Model. (b) Experimental.

$$C(s) = \frac{A}{s^2} - e^{-sKT}\left(\frac{A}{s^2} + \frac{AKT}{s}\right)$$

$$C(z) = A\left[\frac{Tz}{(1-z)^2}\, s(1-z^K) - \frac{KTz^K}{1-z}\right].$$

Since the second term in brackets represents a target position discontinuity, its response is determined by the saccadic system alone.

$$R(s) = A\left[\left(\frac{z}{s^2} + \frac{z^2}{s}\right)(1-z^K) - \frac{KTz^{K+1}}{s}\right]$$

Figure XXI-39 shows the predicted and actual transient response for this type of input.

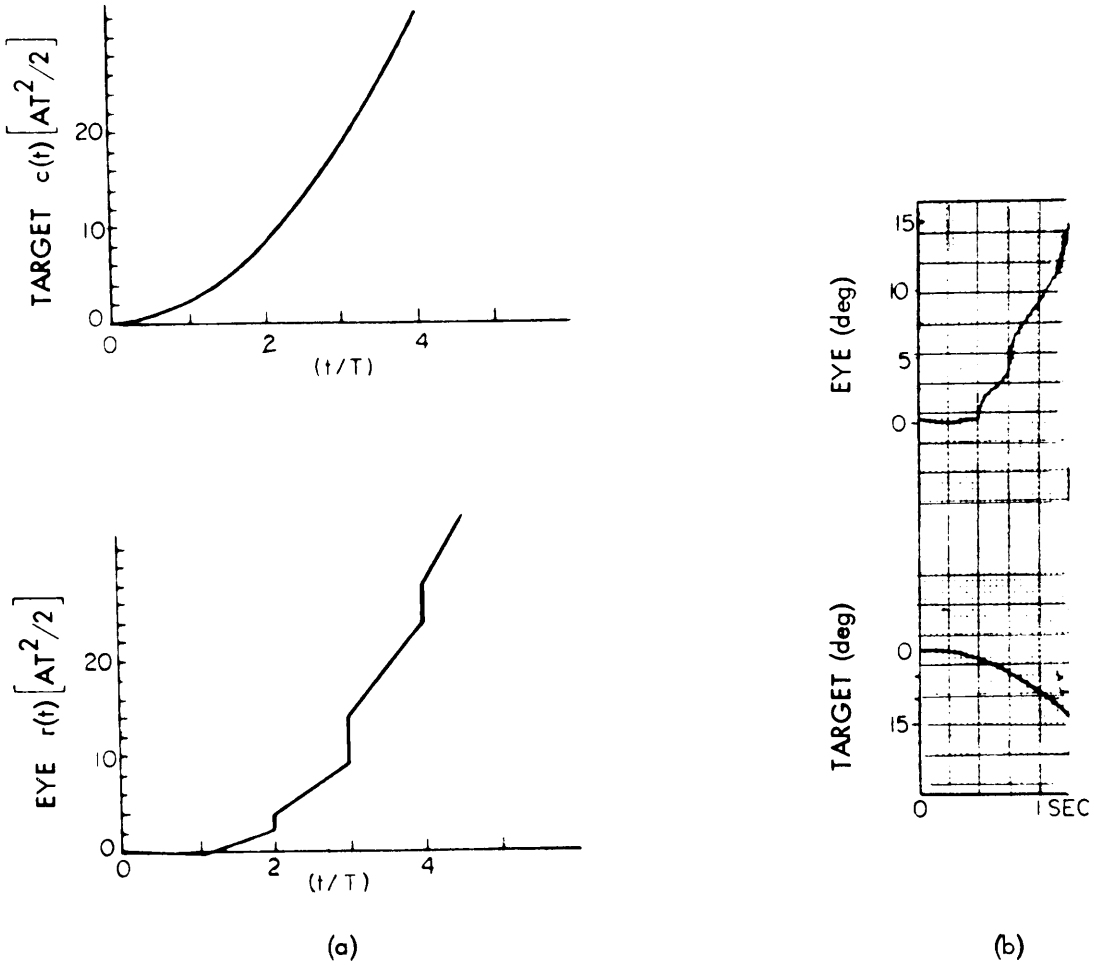

Fig. XXI-40. Parabola response. (a) Model. (b) Experimental.

Notice that for Figs. XXI-39 and XXI-38 the model predicts the occurrence of a second saccadic correction, which is indeed observed in step-ramp experiments, whether the initial velocity is zero or nonzero.

f. Parabola Response

As noted, the system response to a parabolic input yielded evidence for the discrete nature of the velocity tracking system. The input function is

$$C(t) = \frac{At^2}{2}$$

$$C(s) = \frac{A}{s^3}.$$

The z transform of this function can be found in a table of z transforms.

$$C(z) = \frac{AT^2}{2} \frac{z(1+z)}{(1-z)^3}$$

$$R(s) = \frac{AT^2 z}{2} \left(\frac{1+z}{1-z}\right)\left(\frac{1}{Ts^2} + \frac{z}{s}\right)$$

The corresponding time function is plotted in Fig. XXI-40. Notice that the predicted response consists of constant velocity segments and regularly spaced saccadic jumps in the direction of the target motion.

6. Other Supporting Evidence

In addition to the model agreement with experimental transient responses, the model-frequency characteristics closely resemble the experimental Bode plots. Furthermore, experimental transient and frequency characteristics change with the effective visual feedback (varied by controlling target position from measured eye position) in a manner exactly predicted by the sampled-data model.

L. R. Young, L. Stark

References

1. D. H. Fender and P. W. Nye, An investigation of the mechanisms of eye movement control, Kybernetik 1, 81 (1961).

2. A. Sunderhauf, Untersuchungen über die Regelung der Augenbewegungen, Klin. Monatsbl. Augenb. 136, 837 (1960).

3. G. Vossius, Das System der Augenb., Z. Biol. 112, 27 (1960).

4. G. Westheimer, Mechanism of saccadic eye movements, A. M. A. Arch. Ophthalmol. 52, 710 (1950).

5. L. Stark, G. Vossius, and L. R. Young, Predictive control of eye movements, Quarterly Progress Report No. 62, Research Laboratory of Electronics, M. I. T., July 15, 1961, pp. 271-281.

6. C. Rashbass, The relationship between saccadic and smooth tracking eye movements, J. Physiol. 159, 326 (1961).

7. L. R. Young, A Sampled Data Model for Eye Tracking Movements, Sc. D Thesis, Department of Aeronautics and Astronautics, M. I. T., May 11, 1962.

E. AN ANALYTICAL MODEL OF A MUSCLE SPINDLE RECEPTOR FOR SIMULATION OF MOTOR COORDINATION

The muscle spindle receptor is a differential-length receptor found in parallel with contractile fibers of muscles of many species. Its importance in human motor coordination is great, since its positional feedback characteristics cause the myotatic, or stretch reflex. It also sends kinaesthetic information to higher centers to help control complex motor coordination tasks.

A model of this mechanism has been formulated as one component in the more complete model of human motor coordination which was briefly described in Quarterly Progress Report No. 63 (pp. 215-217); as before, continuous signals representing the average number of pulses per second are used.[1] Studies made by Granit[2] and Lippold,[3] and neurological textbooks and handbooks were used as a basis for this model.

1. The Model

The spindle is connected in parallel with the muscle contractile fibers and its direct mechanical effect on the muscle is negligible (Fig. XXI-41a). Thus we can consider the length of the muscle, X_m, to be an input produced either through the alpha efferent nerve or through stretch by external forces. The efferent nerve carries information concerning the length of the nuclear bag to the central nervous system. The gamma efferent nerve excites the contractile element, or intrafusal fiber, of the spindle. It is another input that may bias the output of the nuclear bag or may, perhaps, act indirectly as an input that might control movement. This follow-up servo has been suggested by Merton[4] and Roberts. In our model we have simplified this input to a change in length of the intrafusal fiber, X_γ, and have nerely added it to X_m (Fig. XXI-42). The dynamics of this input may have to be considered more explicitly when we investigate coordinated movements through this input.

The response of the spindle receptor to a step input of stretch, as found by Lippold[3] (Fig. XXI-43), shows approximately 400 per cent overshoot. This differential effect is called the "phasic response." After approximately 200 msec the output settles down to its steady-state value: the steady-state response is called the "tonic response." Lippold[3] also found good evidence to suggest that the phasic response is caused entirely

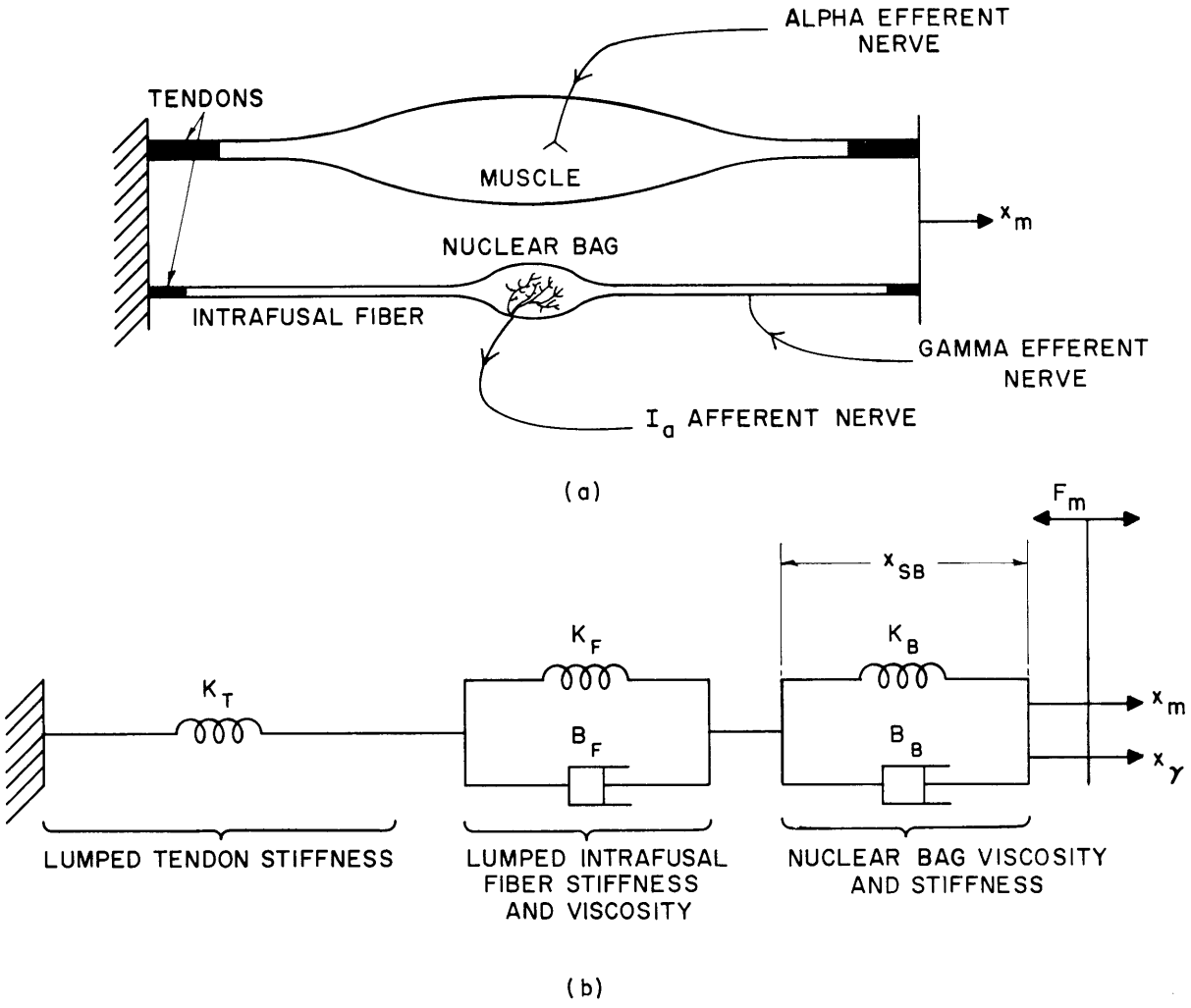

Fig. XXI-41. (a) Diagram showing a simplified muscle with one of its in-parallel spindle receptors removed from the muscle for ease of illustration. (b) Mechanical model of a spindle receptor. Inputs are X_m (length of the muscle) and X_γ (artificial length caused by an input to the intrafusal fiber); the output is X_{SB} (length of the nuclear bag).

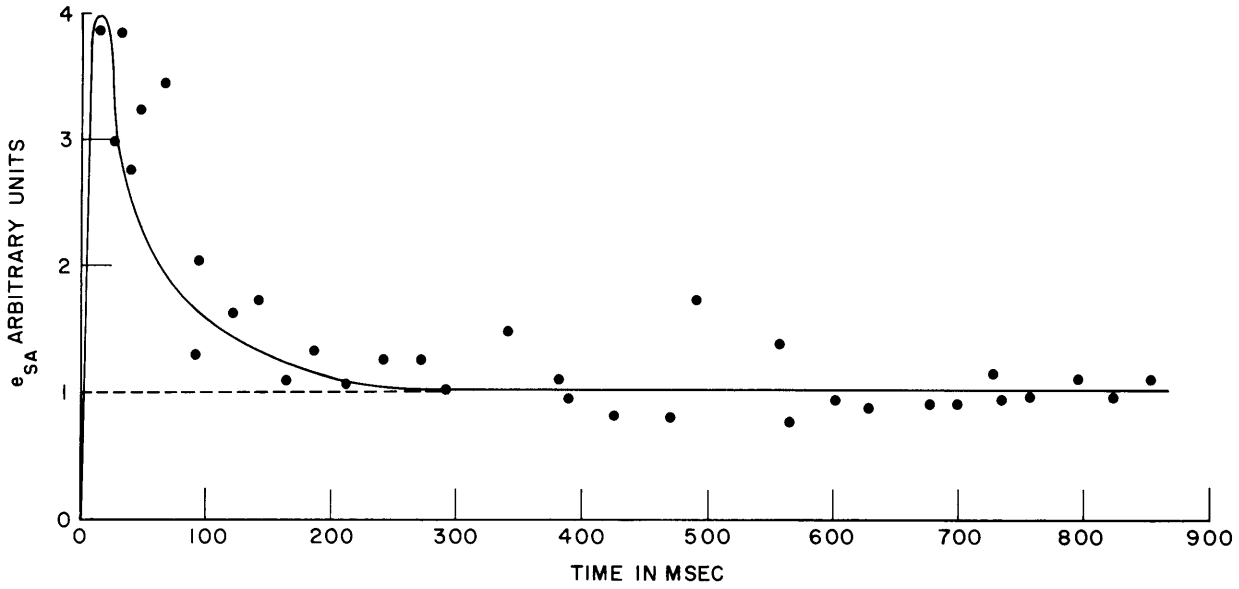

Fig. XXI-42. Step response of the spindle receptor. Dots show data points taken from Lippold.[3] Continuous curve shows model response, $e_{SA}(t)$, in arbitrary units of pulses per second.

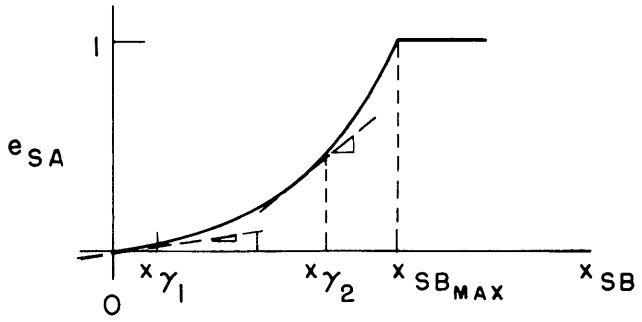

Fig. XXI-43. Input-output characteristics of mechanical-to-electrical transducer of the nuclear bag. e_{SA} is the output of the spindle receptor; X_{SB} is the length of the nuclear bag. Note the change in small-signal gain caused by dc levels of X_m or X_γ, the components of X_{SB}.

by mechanical factors and that the mechanical-to-electrical transducer is a no-memory device. This information has been incorporated into our model.

2. Mechanical Factors

The trasnfer function for the mechanical model of Fig. XXI-41b is

$$\frac{X_{SB}}{X_m} = H(S) = G_m \frac{(T_1S+1)}{(T_2S+1)(T_3S+1)}$$

where

$$T_1 = \frac{B_F}{K_F}; \quad T_2 = \frac{B_F + B_B}{K_F + K_B}$$

$$T_3 = \frac{B_F B_B}{K_T(B_F+B_B)}; \quad G_m = \frac{K_F}{K_F K_B}.$$

We may fit this transfer function to Lippold's data (Fig. XXI-43) by choosing $T_1 = \frac{1}{6.8}$, $T_2 = \frac{1}{18}$, and $T_3 = \frac{1}{200}$. It is interesting then to see what the values of B and K must be. Since there was no way to calculate the mechanical-gain constant K from available data, we are left with three constraints (the three equations relating $T_{1,2,3}$ to B and K) and five unknown B and K. An approximation for two of these unknowns must be made. The intrafusal fiber seems to be identical to any other muscle fiber in a given muscle. Four estimates of the value of K_F were calculated with the use of published data. Our results showed that

$$K_F = 0.1 \text{ kg/meter}$$

(within one order of magnitude). Then B_F was assumed to be approximately equal to B_B—thus only three unknowns were left. Solving for these, we obtained

$$B_F = B_B = 0.015 \text{ kg–sec/m}$$

$$K_B = 0.4 \text{ kg/m}$$

$$K_T = 1.5 \text{ kg/m}.$$

We then evaluated

$$K = 0.2.$$

3. Mechanical-to-Electrical Transducer

Inspection of Granit's data[2] reveals that the tonic input-output characteristic of the spindle receptor is somewhat parabolic. Furthermore, other curves show that the tonic gain increases with increased gamma bias (X_γ). It was found that a squaring operator

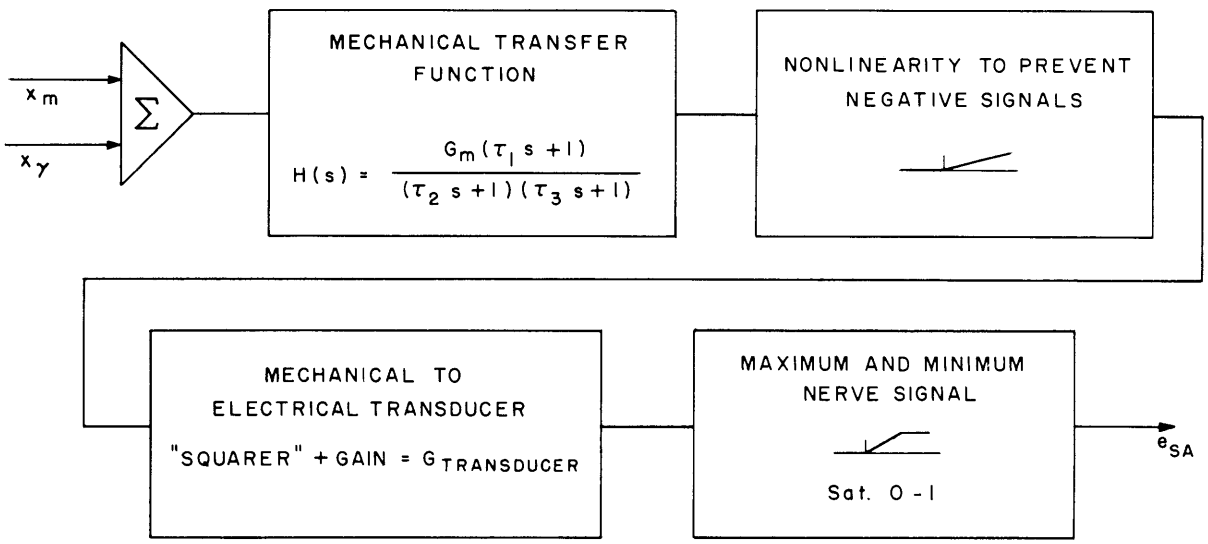

Fig. XXI-44. Complete block diagram of the spindle receptor model. Inputs are muscle length and length that is due to gamma input and to intrafusal fiber; output is average number of pulses per second.

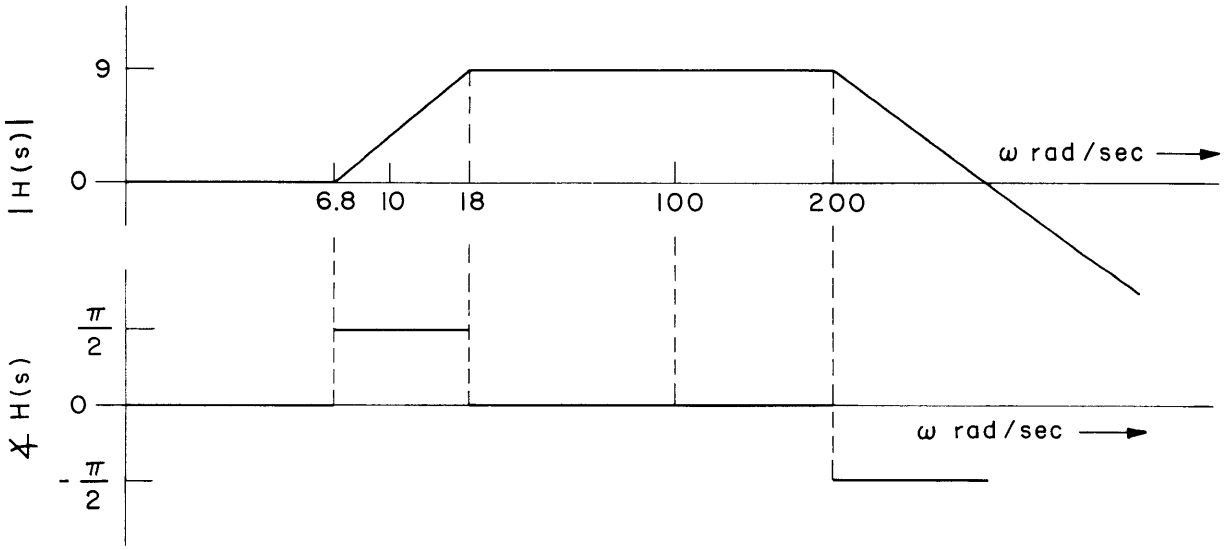

Fig. XXI-45. Asymptotic Bode plots of the gain and phase characteristics of H(S), the transfer function of the mechanical part of the spindle receptor model.

fits these data quite well (Fig. XXI-44). The increased slope at $X_{\gamma 2}$, as compared with $X_{\gamma 1}$, shows the increased small-signal gain for an increase of gamma bias. Negative signals cannot be generated by the transducer; thus a saturation at zero is inserted before the squarer (Fig. XXI-43). Also, there is an upper limit to the number of impulses that can be carried by the spindle efferent nerve. An upper-limit saturation provides this limit.

4. Remarks

An asymptotic Bode plot of H(S) (Fig. XXI-45) illustrates the approximate frequency response of the model to small signals in normal operating ranges of bias. Note that between 7-18 radians per second the response is differential. In this range the spindle receptor should cause viscous damping effects, rather than spring effects, on the overall system.[1] Unpublished data on the frequency response of the stretch receptor in the tail of crayfish indicate that these frequency-response characteristics are quite similar.[5]

J. C. Houk, Jr., L. Stark

References

1. J. Atwood, J. Elkind, J. Houk, M. King, L. Stark, and P. A. Willis, Digital computer simulation of a neurological system, Quarterly Progress Report No. 63, Research Laboratory of Electronics, M. I. T., November 15, 1961, pp. 215-217.

2. R. Granit, Neuromuscular interaction in postsutural tone of the cat's isometric soleus muscle, J. Physiol. 143, 387-402 (1958).

3. O. C. J. Lippold, J. G. Nicholls, and J. W. T. Redfearn, Electrical and mechanical factors in the adaptation of a mammalian muscle spindle, J. Physiol. 153, 209-217 (1960).

4. P. A. Merton, Spectulations on the servo-control of movement, CIBA Foundation Symposium, "The Spinal Cord," edited by G. E. W. Wohrtenholme (J. and A. Churchill, Ltd., London, 1953), pp. 247-260.

5. V. Sanchez, Crayfish frequency response data, Neurology Section, Electronic Systems Laboratory, M. I. T., 1962.

F. TRANSIENT RESPONSES OF HUMAN MOTOR COORDINATION SYSTEM

Investigation of the transient response of the human motor coordination system has been extended by: (a) quantification of voluntary tension by using sphygomanometer pressure (blood pressure cuff); (b) delivery of mechanical disturbance impulses to the handle shaft by means of a pendulum; and (c) approximation of the mechanical impulse response ($h_m(t)$) and the "follow-up" portion ($h_f(t)$) of the visual impulse response ($h_v(t)$) by a second order equation.

Our objective is to determine the effect of voluntary motor tension on the subject's response to both visual and mechanical impulse inputs in order ultimately to simulate

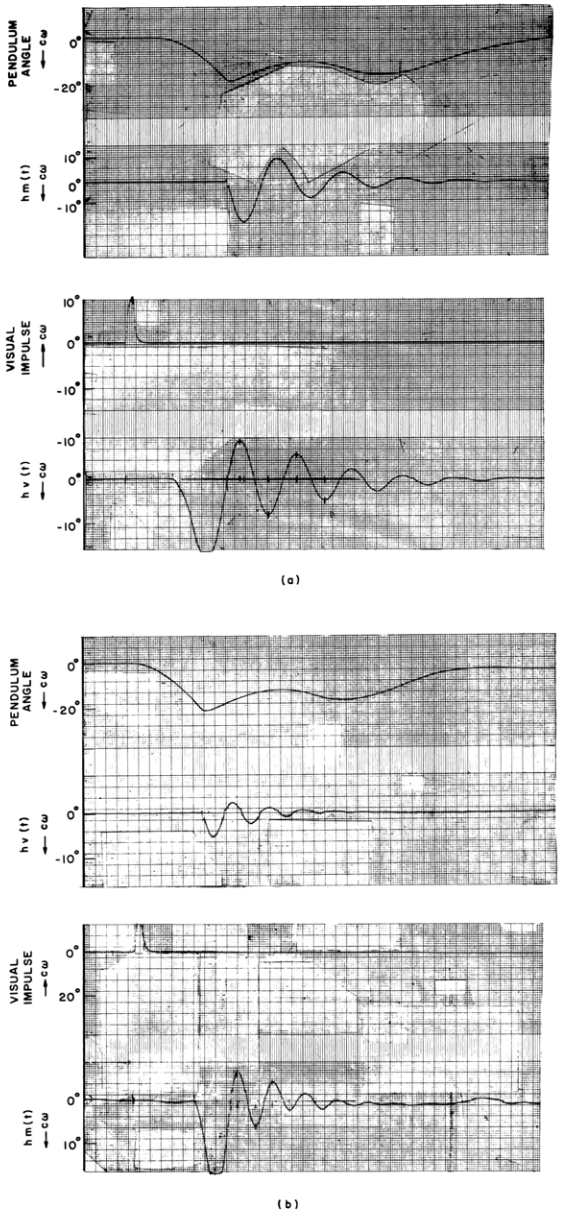

Fig. XXI-46. Examples of $h_m(t)$ and $h_v(t)$ at two tension levels. (a) Relaxed, 30 mm Hg. (b) Tense, 50 mm Hg.

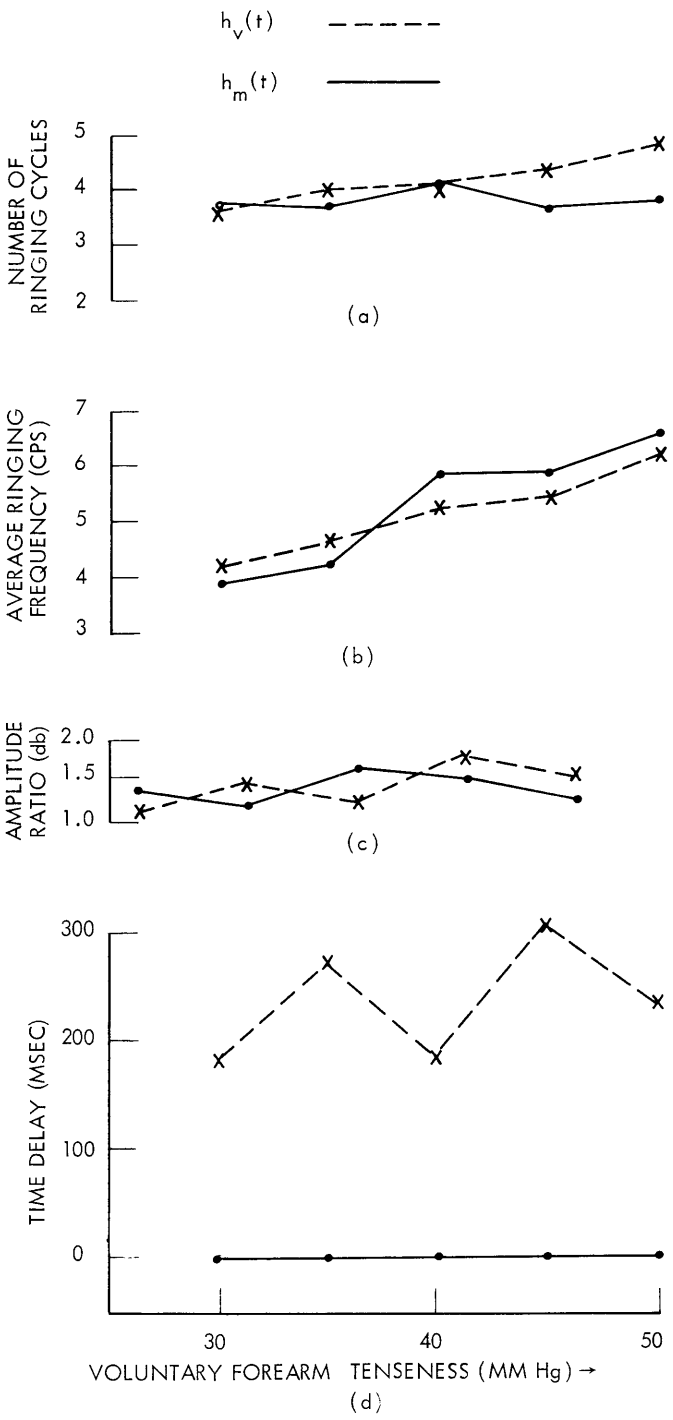

Fig. XXI-47. Comparison of variables analyzed in the response to visual and mechanical impulses as a function of state of muscle tension. (a) Number of ringing cycles. (b) Average ringing frequency. (c) Average amplitude ratio (db). (d) Time delay (msec).

the neuromuscular control system.

For measuring voluntary tension, the height of the mercury column controlled by a sphygomanometer cuff attached to the forearm was superior to the integrated electromyogram and was used in the experiment reported here. With this objective measure the subject could control his voluntary tension to any one of five levels with ease and reproducibility as compared with our previous reliance on the subject's estimate of his own tension level.

A mechanical pendulum whose position was monitored by a potentiometer was used to deliver impulses of torque to the handle shaft of the apparatus. The travel and rebound angles, the length and weight of the pendulum, and the elasticity of the impact determine the input energy delivered to the system. Examples of mechanical and visual impulse responses at two tension levels are shown in Fig. XXI-46. The increase in ringing frequency and the decrease in amplitude of response to mechanical impulses and of the follow-up portion of the response to visual impulses with increase of tension are shown in Fig. XXI-46. These experiments were carried out by using irregularly spaced, that is, unpredictable, mechanical and visual impulses, all of which require the same supination of the wrist. Parameters from these responses are shown in Fig. XXI-47, in which it can be seen that $h_m(t)$ and $h_v(t)$ have similar characteristics except, of course, for the time delay. The motor response has no time delay, whereas the visual response shows a time delay of approximately 200 msec. The insensitivity of visual response time delay to tension as contrasted with earlier results is possibly due to the distraction of the subject's attention by the task of controlling his voluntary tension.

In order to quantify some of these changes in response, we fitted a simple underdamped second-order system to both $h_m(t)$ and $h_f(t)$. Note that all of these responses

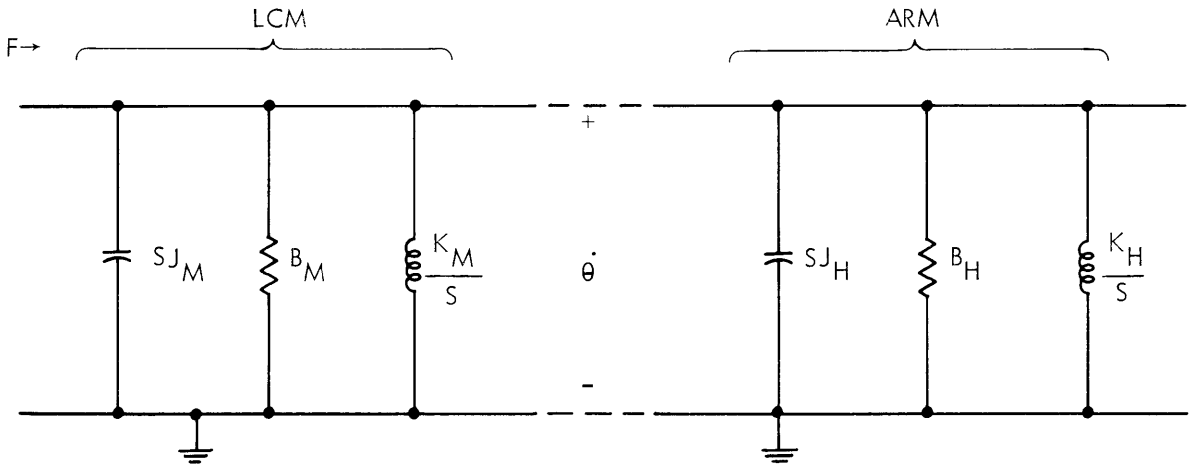

Fig. XXI-48. Mobility analog of light coordination machine and forearm.

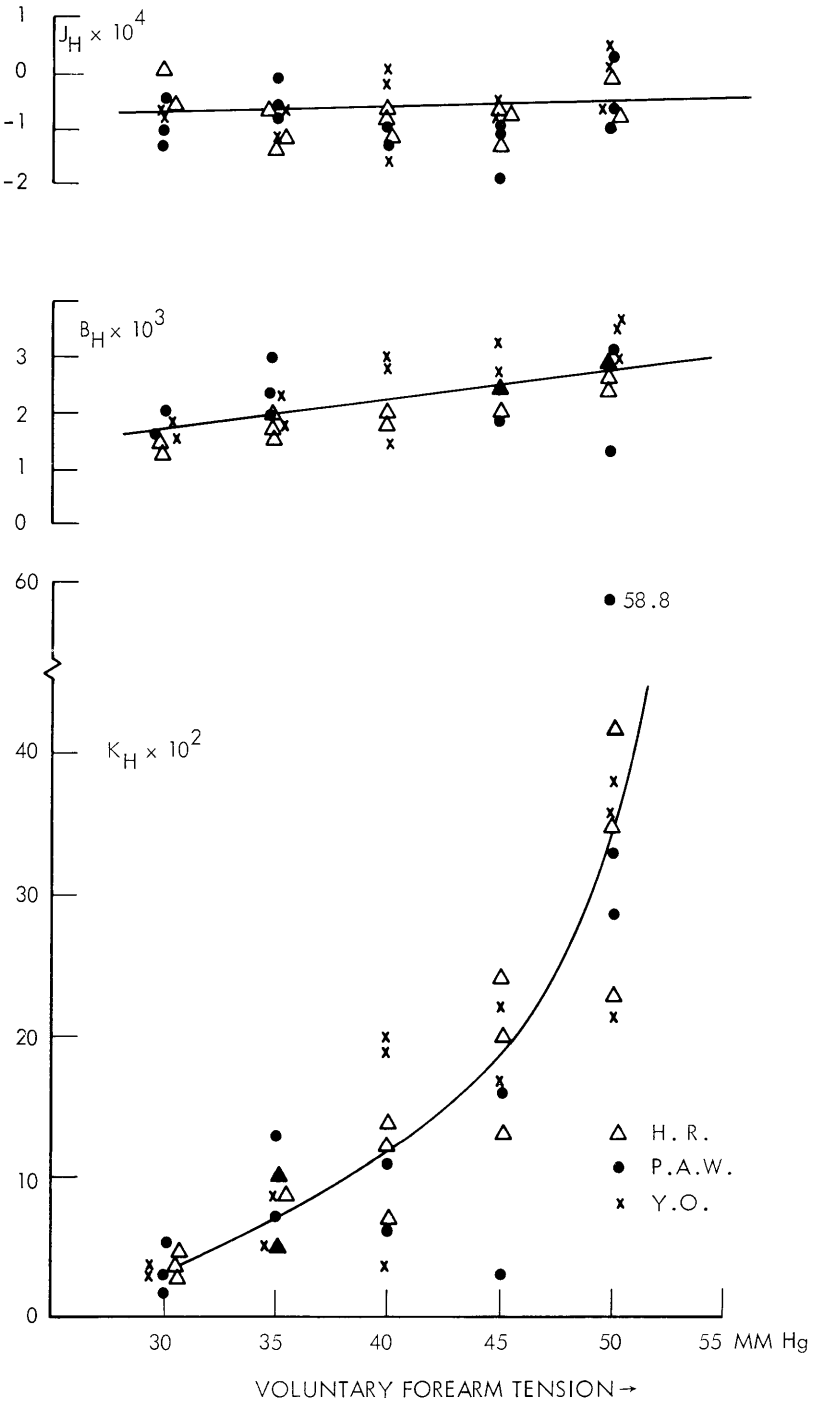

Fig. XXI-49. Variation of equivalent mechanical parameters of arm as a function of voluntary tension. Inertia J in $(kg\text{-}m\text{-}sec^2)/rad$; viscosity B in (kg-m-sec)/rad; and elasticity K in (kg-m)/rad. Results from a number of experiments on 3 subjects are shown.

include the mechanical characteristics of the apparatus so that it was necessary to determine these characteristics and subtract them. In Fig. XXI-48 is shown the mobility analog of the apparatus and the arm. Since all of the elements appear in parallel, the use of their equivalent admittance values means that the machine elements may be subtracted directly from their corresponding elements of the total response. A GE 225 program, written by Houk, was utilized to perform these calculations in a convenient manner. A plot of variation of mechanical constants of the arm as a function of voluntary tension is shown in Fig. XXI-49; K is a strong function of voluntary tension, while B increases only slightly with an increase in tension. Values of J are small, are the

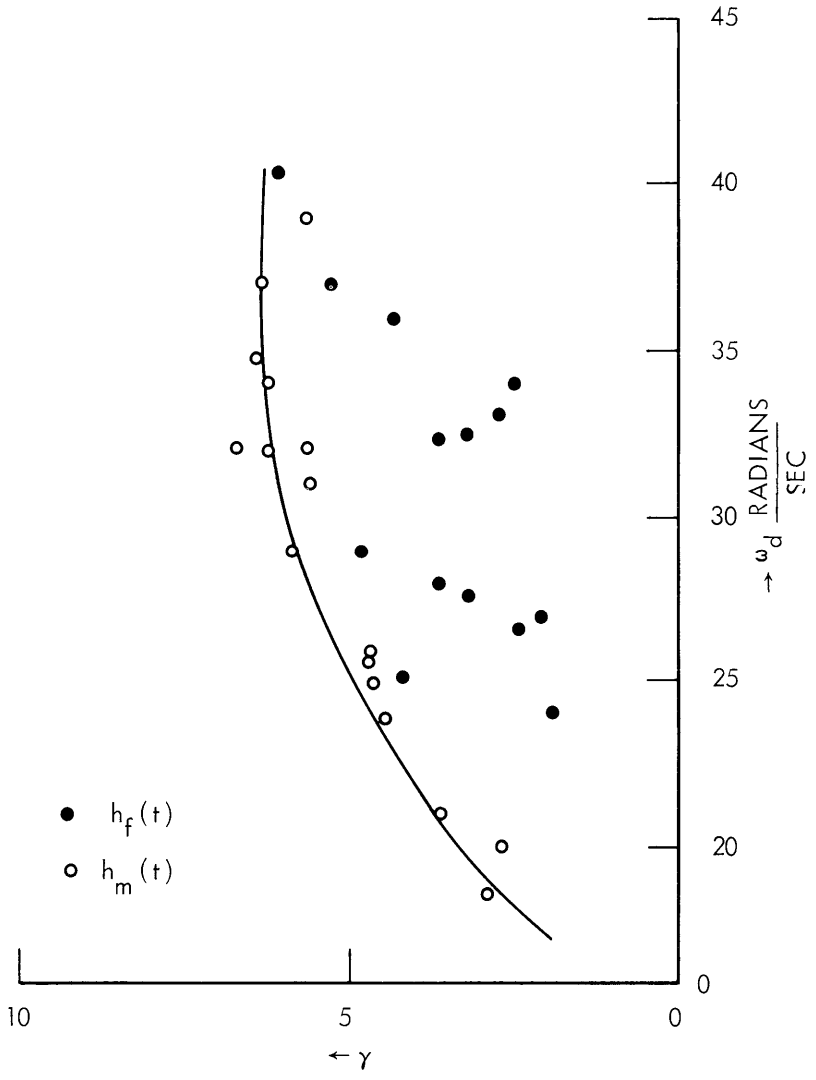

Fig. XXI-50. Effect of voluntary tension on the poles of the $h_m(t)$ and $h_f(t)$ equivalent second-order systems.

result of subtracting two large values, and are not believed to be significant.

The poles of the equivalent second-order system are at $s = -\gamma \pm j\omega_d$, and the effect of tension on the system is shown in Fig. XXI-50 by the path of migration of these poles. The principal effects of an increase in voluntary tension on the $h_m(t)$ equivalent second-order system are an increase in absolute bandwidth and a slight decrease in stability margin. It appears that the fit of $h_m(t)$ by a second-order system is reasonably good, although our block diagrams[1] of the physiological elements show that the system is more complex.

The response to a visual impulse is the behavior of an even more complex system. We postulate that $h_v(t)$ consists of two phases: the first, consisting of time delay and the first overshoot, is considered a visually driven response. After a transition period, the second, or "follow-up" movement, $h_f(t)$, is considered controlled by the postural reflex loop attempting to bring the hand to rest. Thus it is only this second portion, $h_f(t)$, that is comparable to the mechanical response. Only 30 per cent of the $h_v(t)$ records yielded $h_f(t)$ portions that could be reasonably described by a second-order fit, and even these data showed considerable scattering. The $h_f(t)$ points on the s-plane diagram of Fig. XXI-50 show the effects of this scatter. The principal correlation of the $h_f(t)$ equivalent second-order system with increase in voluntary tension is increase in absolute bandwidth.

These results are helping us to approach in a quantitative fashion the complex interactions between voluntary tension, voluntary movement, and postural feedback control.

Y. Okabe, Helen E. Rhodes, L. Stark, P. A. Willis

References

1. J. Atwood, J. Elkind, J. Houk, M. King, L. Stark, and P. A. Willis, Digital computer simulation of a neurological system, Quarterly Progress Report No. 63, Research Laboratory of Electronics, M. I. T., October 15, 1961, p. 216, Fig. XV-22.

G. SIMULTANEOUS HAND AND EYE-TRACKING MOVEMENTS

Separate experiments on hand and eye tracking have shown interesting comparisons between these two systems in response to unpredictable and predictable square waves.[1] Because of the large variation in response with different subjects under minor modifications of the experimental apparatus and with time, we decided to measure both of these system responses simultaneously. The eye and hand experimental arrangements have been separately described.[2]

Actual experimental records are shown in Fig. XXI-51. Sequential patterns of response times such as in Fig. XXI-52 could be obtained, or histograms of response, as in Fig. XXI-53, could be constructed. The median values of response times (75-150

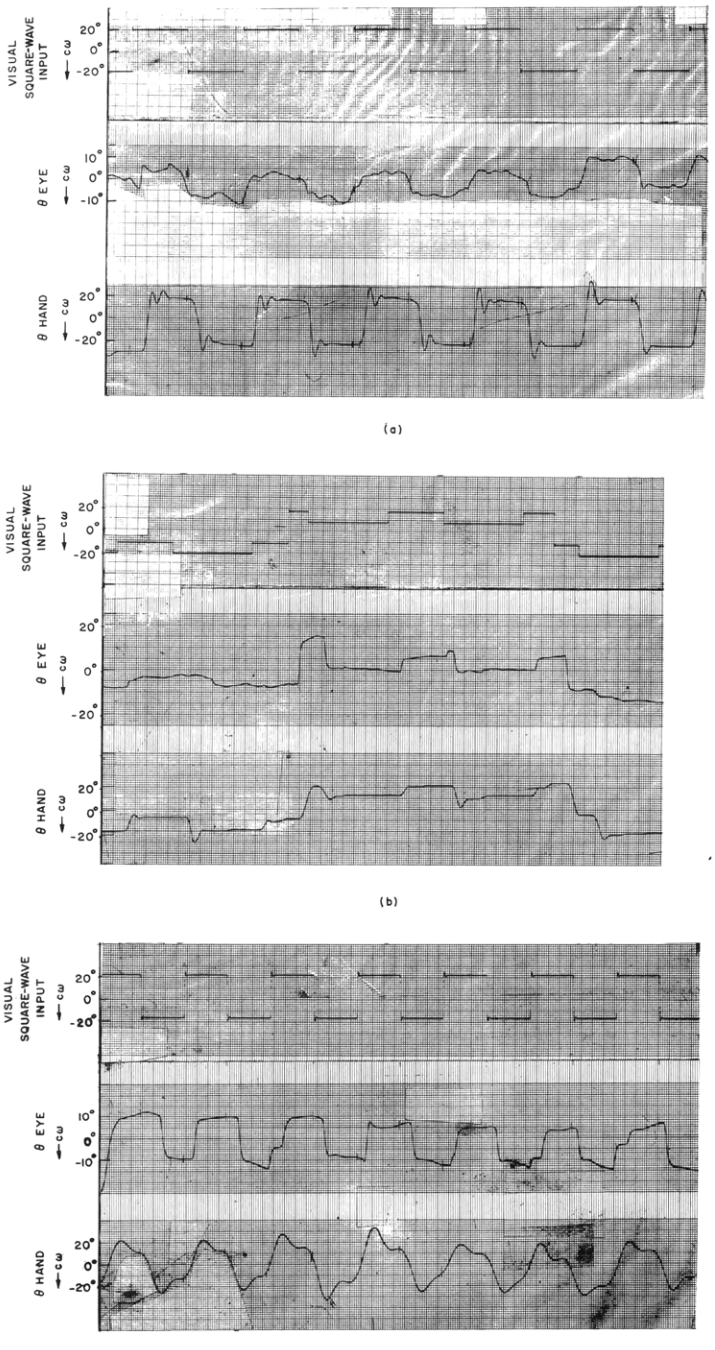

Fig. XXI-51. Eye and hand tracking response records. (a) 0.5-cps square-wave input; (b) Irregular square-wave input; (c) 1.3-cps square-wave input.

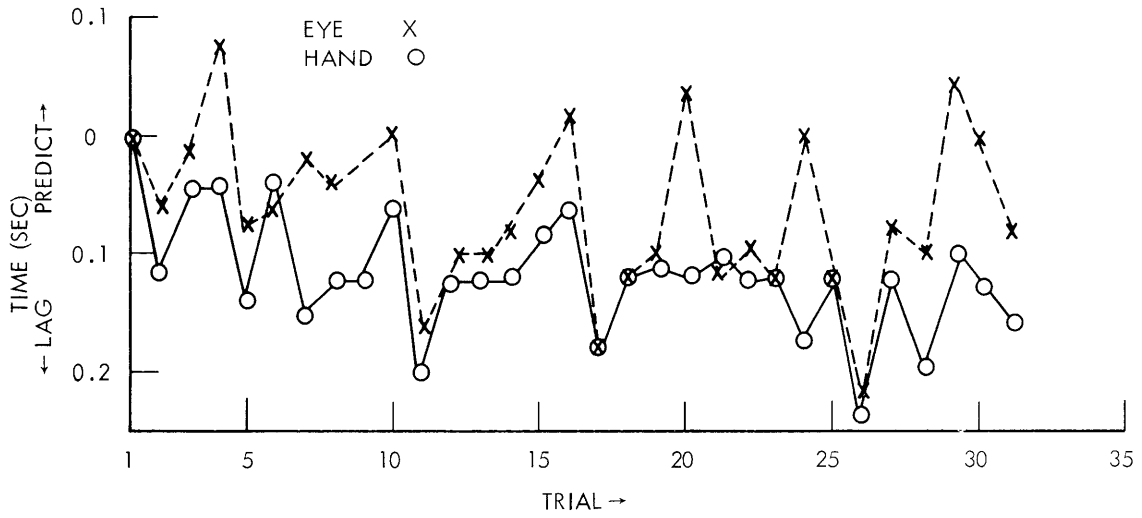

Fig. XXI-52. Sequential patterns of response times for eye and hand tracking.

responses) showed dependence upon the frequency of the regular square-wave target pattern (Fig. XXI-54).

For irregular target patterns and low-frequency (<0.5 cps) regular patterns the eye showed less time delay than the hand (Figs. XXI-51a and 51b, XXI-52, XXI-53a and 53b, and XXI-54). At moderate frequencies (0.7-1.0 cps) the hand develops prediction faster and to a greater extent than the eye(Fig. XXI-54). At higher frequencies (> 1.2 cps) the hand shows considerable prediction, while the median eye response time starts to lag (Figs. XXI-51c, XXI-53c, and XXI-54). This time lag comparison is in contrast with the maximum velocity responses of the two systems – the eye motion giving much faster rise and fall times than the hand.

At these higher frequencies, the eye may spontaneously stop moving without noticeably interfering with hand tracking (Fig. XXI-55). Conversely, the hand movement clearly and consistently seems to aid the eye-movement control system, as demonstrated in Fig. XXI-55b, which shows a typical example of eye movement deterioration during the cessation of hand tracking. Figures XXI-54a and 54b show this effect in terms of median response times. At low frequencies some correlation is evident between eye and hand response times, as Fig. XXI-52 demonstrates.

Processing retinal information is clearly an early operation in hand tracking a visual target. This same information is necessary for eye movement control. However, eye movement does not appear to be essential for the range of target motions (±20°) which we have used, in terms of response times for hand tracking. Conversely, the control system for eye movements seems to be aided at high frequencies by signals deriving from hand movement, which is operating here with

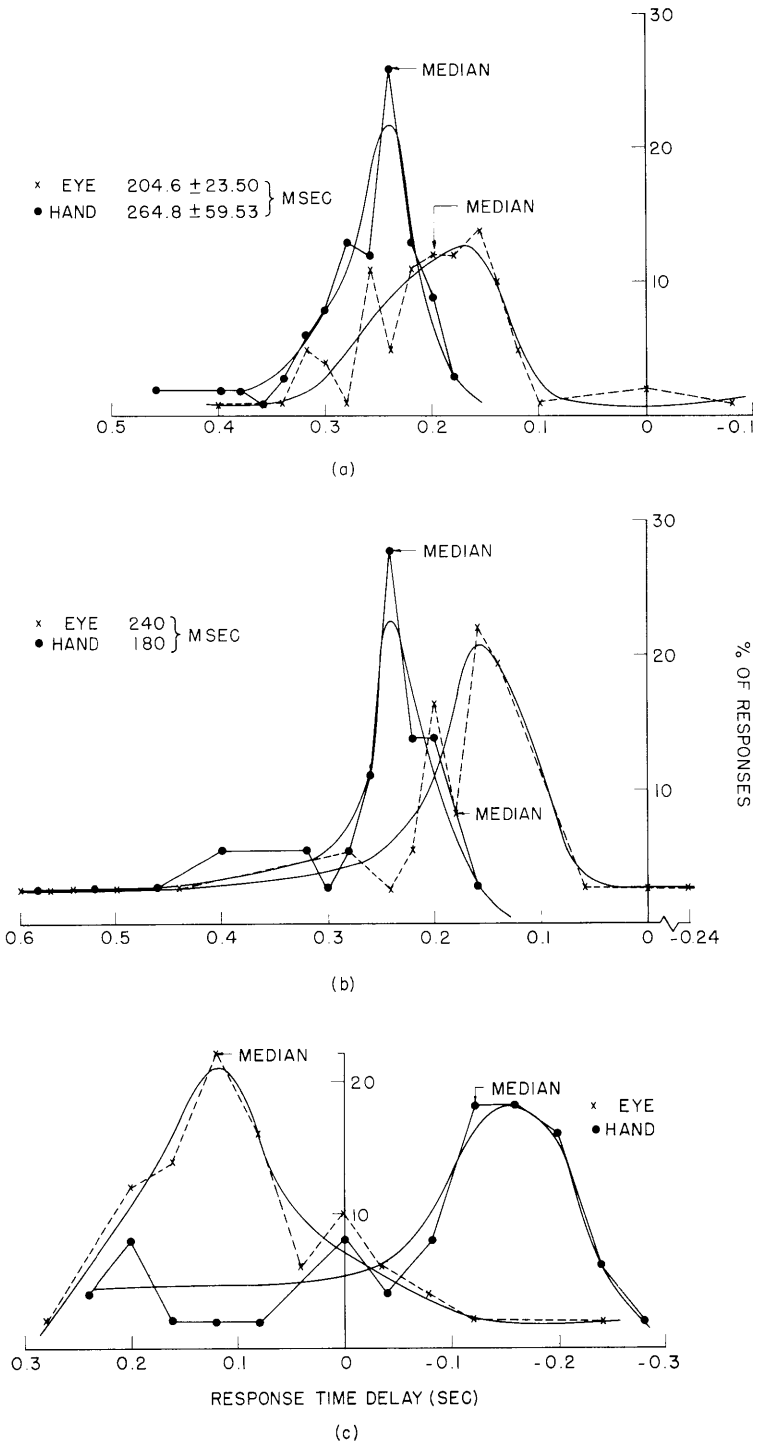

Fig. XXI-53. Histograms of response times for simultaneous eye and hand tracking (a) Irregular square-wave input; (b) 0.25-cps square-wave input; (c) 1.2-cps square-wave input.

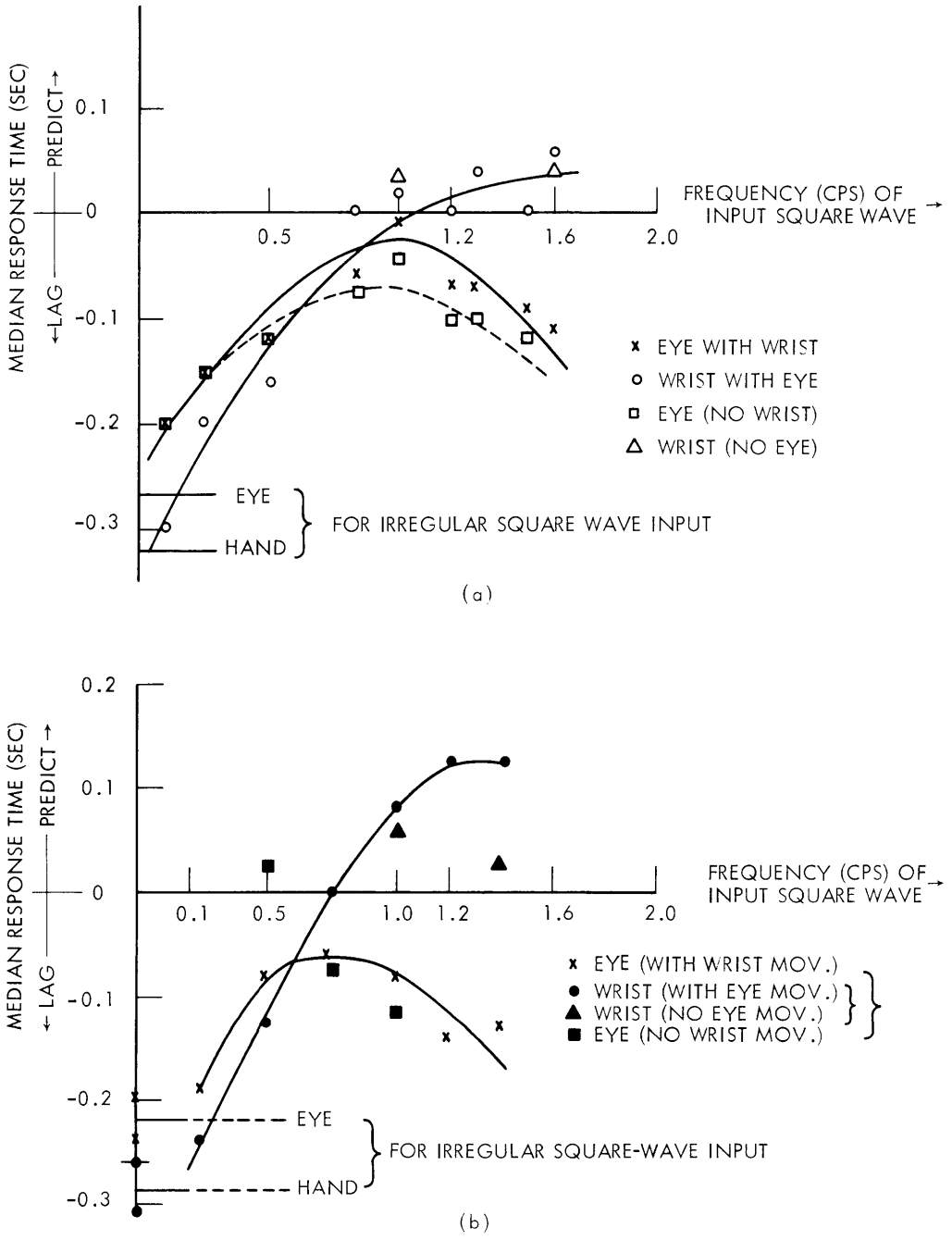

Fig. XXI-54. Median response times of eye and hand as a function of input frequency. Input, ±20° square wave. Four conditions shown: eye and hand together and each alone.

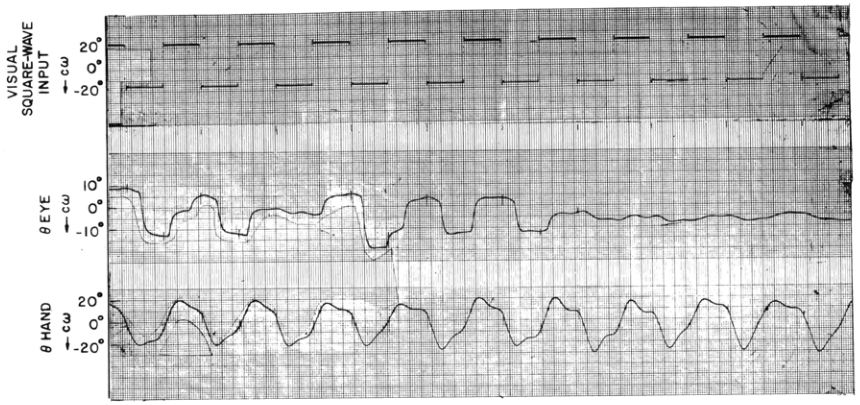

(a)

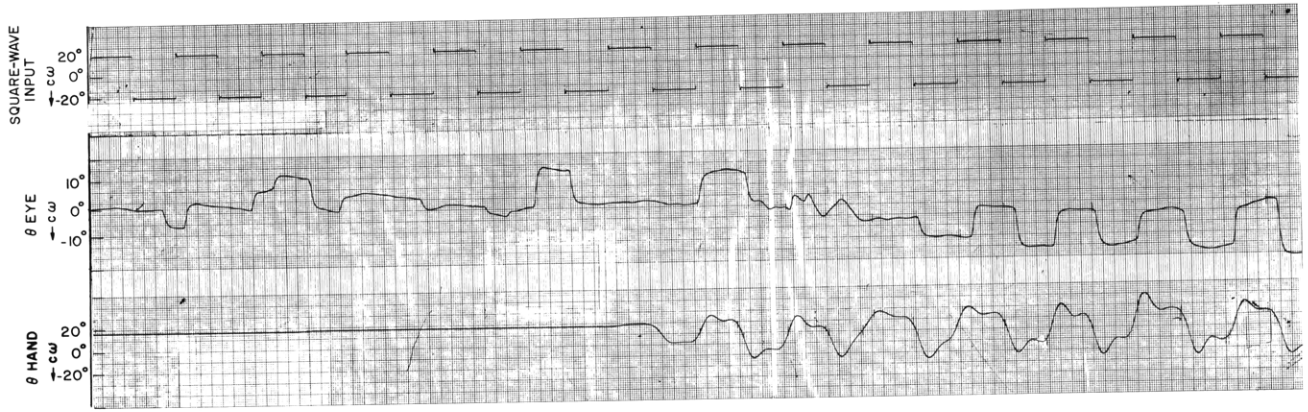

(b)

Fig. XXI-55. Eye tracking behavior. (a) Spontaneous eye stopping. (b) Improvement in eye tracking with hand tracking added.

much more prediction than the eye system.

In summary, by simultaneously recording eye and hand tracking movements and measuring their respective response times, some similarities, differences, and interactions between these two systems have been demonstrated.

Y. Okabe, Helen E. Rhodes, L. Stark, P. A. Willis

References

1. J. Houk, Y. Okabe, Helen E. Rhodes, L. Stark, and P. A. Willis, Transient responses of human motor coordination system, Quarterly Progress Report No. 64, Research Laboratory of Electronics, M. I. T., January 15, 1962, p. 322; see Fig. XXVIII-13.

2. Ibid., pp. 315-316.

H. COMPUTER ANALYSIS OF HANDWRITING

A previous report described preliminary results obtained with the TX-0 computer and its photomultiplier light cannon cathode-ray oscilloscope scanning system.[1] At that time only inked words on Plexiglas were used. The aim of the present report is to evaluate H. Levy's program by testing with enlarged photographs of real signatures.

Problems encountered included unreliability of the scanning system which could be alleviated by a "look-twice" scan routine to double-check results and reduce the effect of extraneous noise. In general, the program performed accurately and repeatably.

The program is rigid and is not adaptable to different sizes of samples, nor can it make full use of the communication that is available between the operator and the computer. In the future, we could aim at making more of the constants that are used in decision-making and measure-making controllable by the operator.

Only two criteria were studied to separate signatures of healthy and diseased persons. These were average curvature (at direction and transition points) and width ratio (between up and down strokes). Figure XXI-56 shows results from a small sample of signatures which indicate some correlation with the Kanfer test.

The Edge Track is another TX-0 computer program for the analysis of handwriting that is being written to allow maximum flexibility of communication between the operator and the computer. The first step in this direction is a subroutine that enables the TX-0 computer to trace the edge between a light and a dark region on a transparent print.

This program has been prepared and tested. The program is coded as a subroutine that, for each call, advances an approximately equal distance along the boundary. The time for each usage is approximately 1 msec. Several properties make the subroutine uncommonly flexible: its behavior is unchanged by photonegation of the input transparency; it has no preferred direction and will return the same information if the input

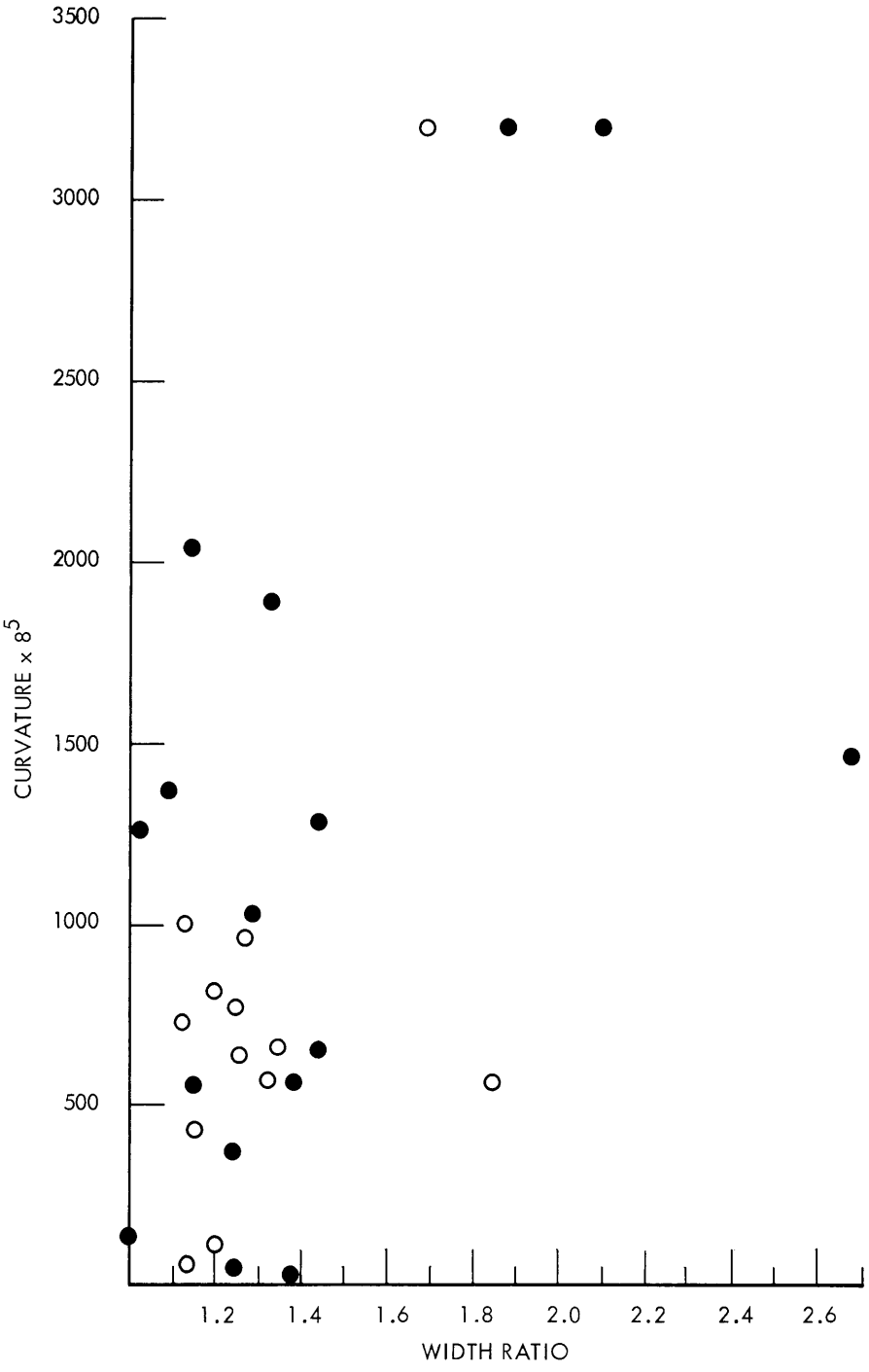

Fig. XXI-56. Experimental results of healthy (o) and diseased (●) signatures. Each point represents average width ratio and curvature value for a particular valid transition point.

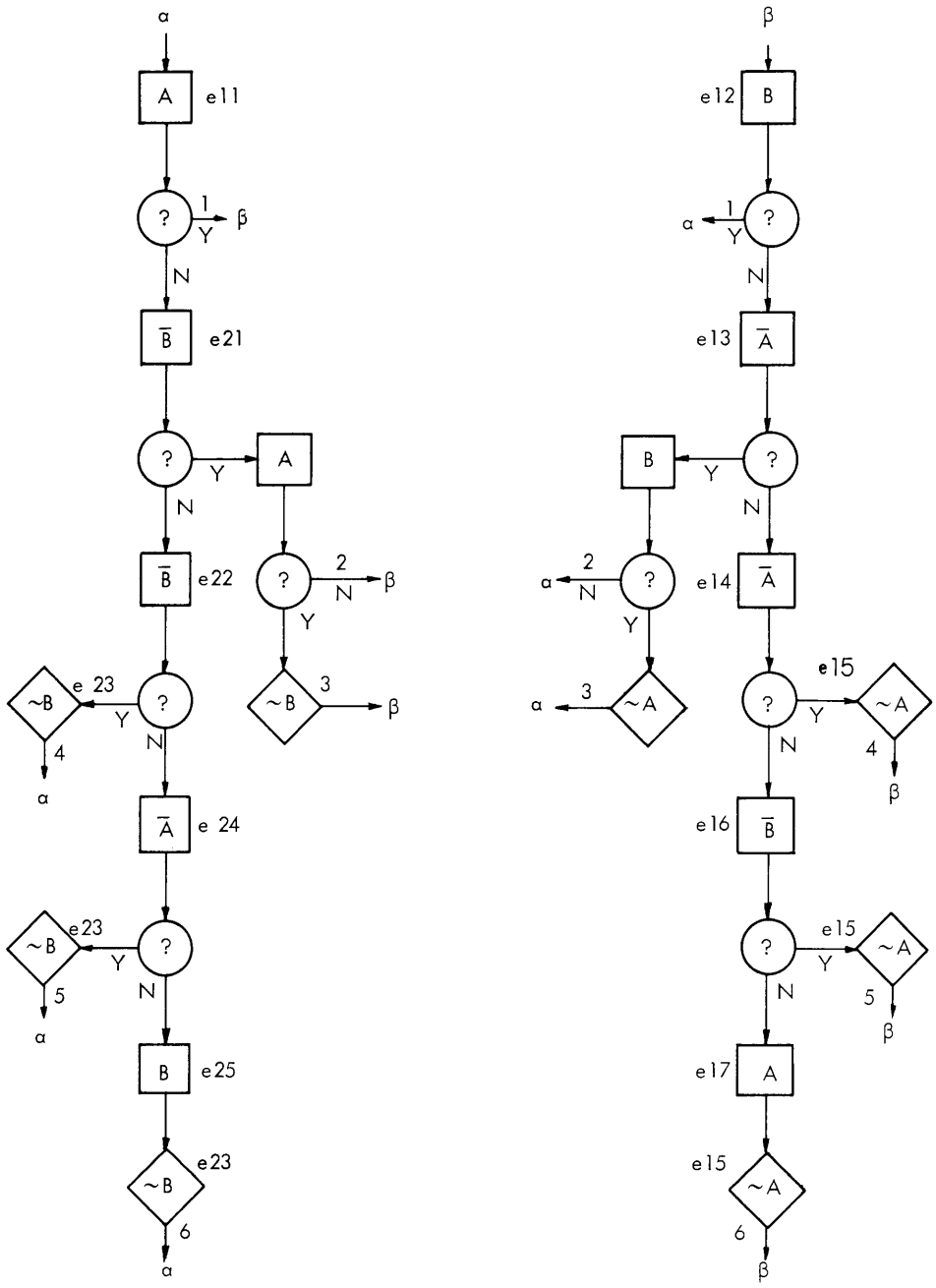

Fig. XXI-57. Edge-Tracer subroutine.

A Move in A direction.

Ā Move in contrary sense to A direction.

N ? Y Did the last movement cross the edge? No – go to N. Yes – go to Y.

~A Reverse the defined sense of A direction.

(The logic that enables this program to be called a subroutine is not indicated.)

sample is rotated or reflected; it is sufficiently fast that the speed of any program in extracting information from the pictorial material is limited by the analytic computation rather than by the input subroutine. Figure XXI-57 is the flow diagram.

The Edge-Tracer Algorithm that is used is of interest in that it is composed of only three basic operations. Two unit vectors, A and B, are defined as orthogonal and are initially chosen from the four alternatives x, -x, y, -y which are such that their resultant defines the initial direction of motion along the black-white boundary. The three operations are: (a) move one increment (whose length is a parameter of the subroutine) in the direction of either A or B or in the contrary sense to either; (b) branch control according to whether the last move crossed the boundary or not; (c) redefine either A or B as opposite its previous sense.

A Line-Tracer routine has also been coded which, by using two copies of the edge-tracer subroutines, will progress along a band of black-in-white or white-in-black. One edge of the band is defined as the master-edge location by the boundary-tracing subroutine, and then adjust the follower-edge location to find a local minimum in the distance between master point and follower point.

P. R. Samson, P. A. Willis, R. G. Kurkjian, L. Stark

References

1. H. Levy and L. Stark, Computer analysis of handwriting, Quarterly Progress Report No. 63, Research Laboratory of Electronics, M. I. T., October 15, 1961, pp. 214-215.

I. PUPILLOMETRY

The development of adequate instrumentation for the study of dynamic pupil movements has been a continual activity of physiologists since at least 1887. The infrared electronic pupillometer[1] (U. S. Patent 3,036,560) combines the advantages of continuous measurement with easily controlled open-loop stimulation; its main defect is the necessity for calibrating (by flash photography), since each iris has pigment that varies in infrared reflectance. A recent review of pupillometry included a description of an opto-mechanical infrared scanning pupillograph of Lowenstein.[2,3] The instruments described in this report represent attempts to utilize the scanning method (which does not require individual calibration) in pupillometry.

1. Television Pupillometer

a. System

A commercial closed-circuit television system was used as the main element in the system shown in Fig. XXI-58. Although the scanning rate is unnecessarily high, the

advantages of existing video circuitry were too attractive to attempt further development.

An image-converter tube permitted the use of invisible infrared light for the illumination of the eye. A simplified version of the video signal obtained by scanning

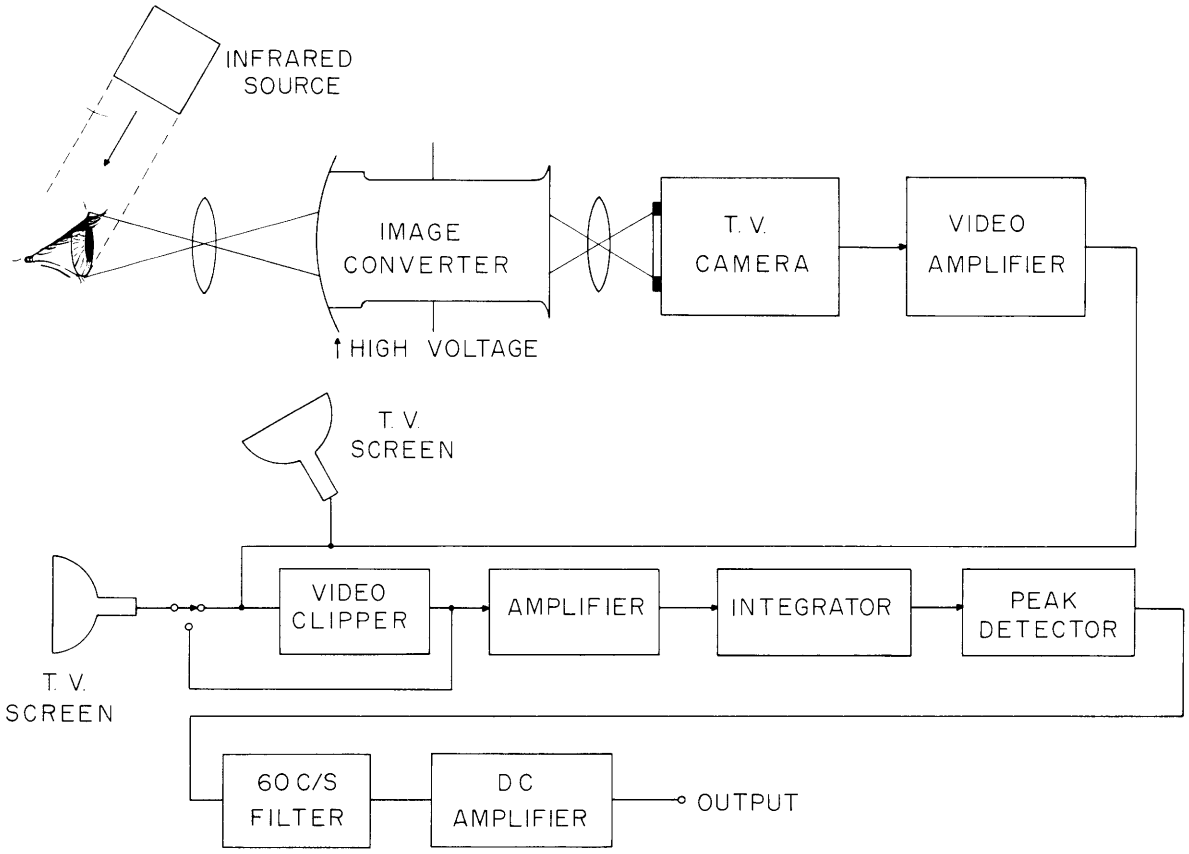

Fig. XXI-58. Block diagram of the Television Pupillometer.

across the scelera, iris, and pupil is shown in Fig. XXI-59, together with an indication of the clipping levels employed to obtain a television picture of the pupil alone, independently of the infrared reflectance of the iris. This clipping also served to reduce the amplitude of the synchronizing pulses so that the output of the following integrator could provide a more sensitive measure of the variations in pupil area.

The integrator is a 60-cycle sampling integrator. It is followed by a peak detector, a 60-cycle filter, a dc amplifier, and a pen recorder.

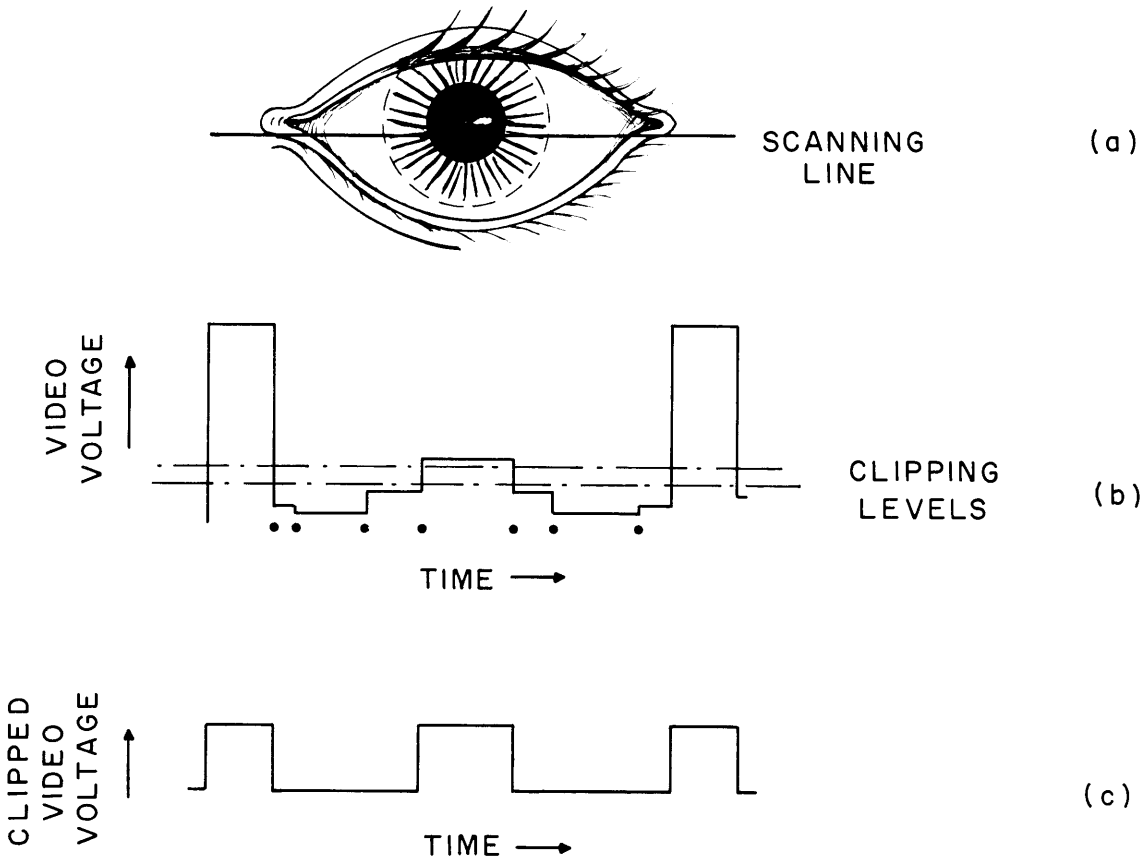

Fig. XXI-59. (a) The pupil and a scanning line. (b) Corresponding video signal and clipping levels. (c) Clipped video signal of the pupil.

b. Performance

An example of the human pupil response is shown in Fig. XXI-60. Also shown are a series of eye blinks that show the excellent high-frequency response of the system.

Evaluation of the system has shown that it is quite linear over the normal range of pupil area when tested by a series of artificial pupils as shown in Fig. XXI-61. The stability of the apparatus (Fig. XXI-61), as well as its accuracy in the face of movements along the optical axis (Fig. XXI-62) and perpendicular to the optical axis (Fig. XXI-63), is good.

A photograph of the television pupillometer with a subject in position is shown in Fig. XXI-64. The subject uses the image of his own pupil on a video monitor as the fixation point and this helps to control movements of the eye and head which would interfere with the accuracy of the experimental measurement.

2. Nonlinear Scanning Pupillometer

A wide range of eye and vision studies requires knowledge of eye position and/or pupil size. A specialized television system that can take continuous readings of pupil

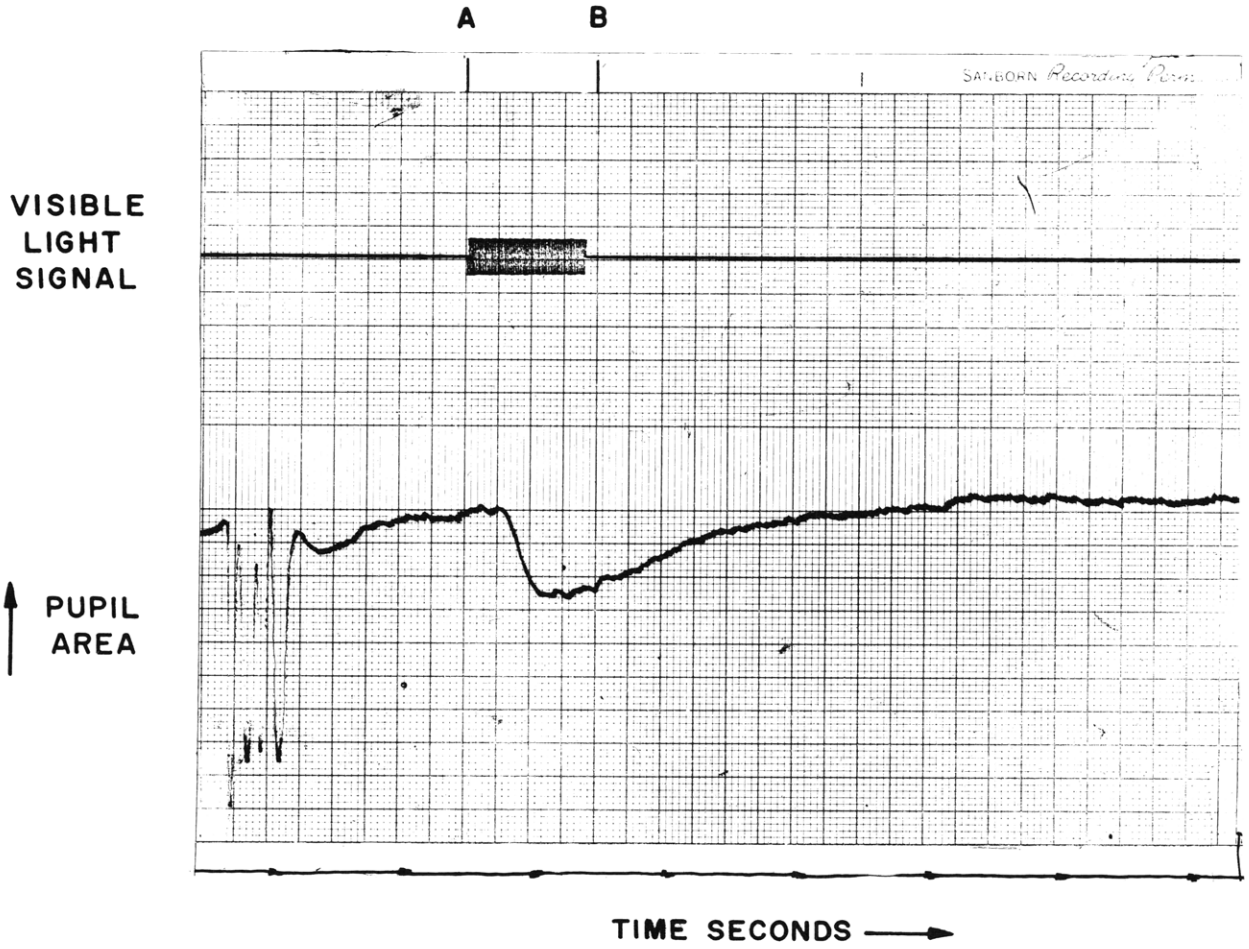

Fig. XXI-60. Pulse response of human eye as measured by the Television Pupillometer. A-B is the visible light pulse into the eye. Lower trace shows a series of eye blinks at left and the response to the A-B signal later.

size and position has been developed.[4] This system uses circular tracking scan. A block diagram of the system is shown in Fig. XXI-66.

A scanning video pickup is used. The scanning spot is made to follow the pupil-iris boundary of the eye. The ac components of the scanning deflection signals are then proportional to the pupil diameter, and the dc components are proportional to the pupil position. Data recovery is therefore very convenient.

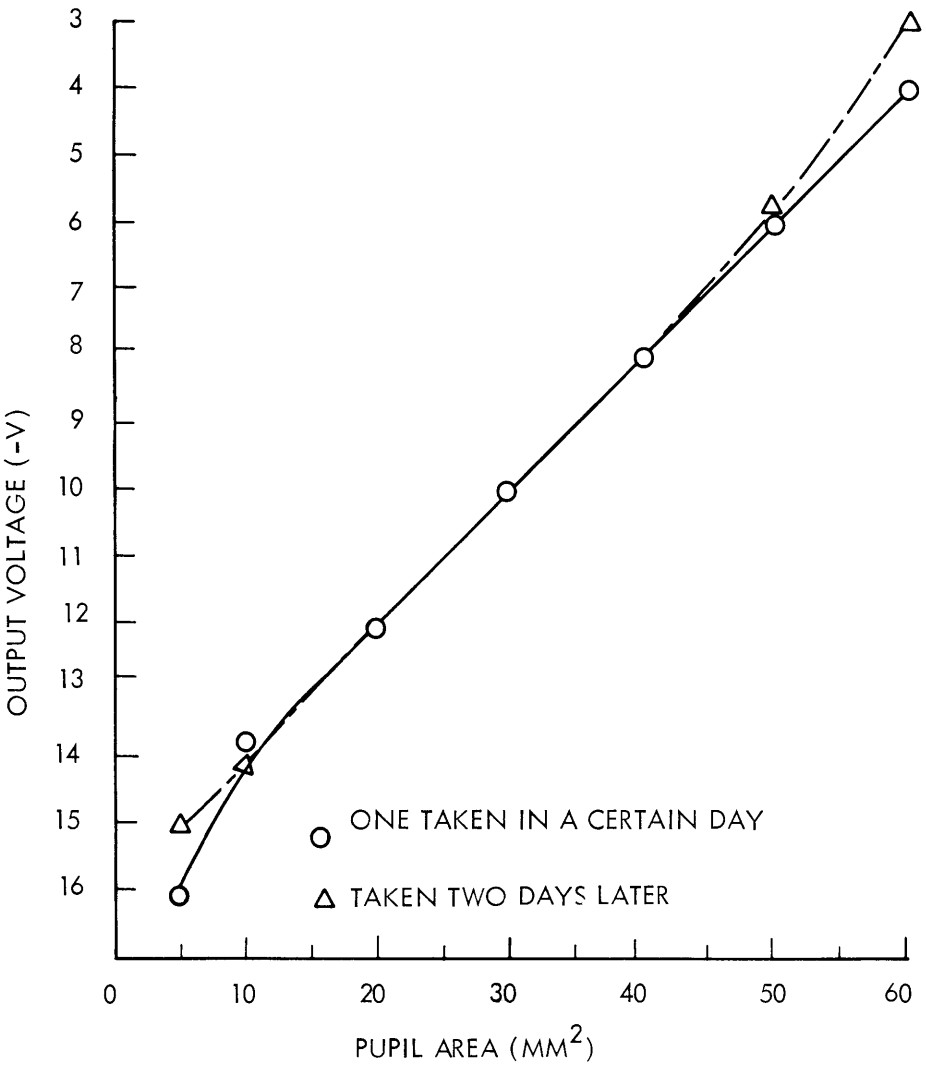

Fig. XXI-61. Calibration of dc amplifier output as pupil area. An artificial pupil was used for calibration.

Laboratory equipment that is capable of evaluating this circular tracking scan technique was designed and built. A record of the read-out of pupil diameter for step changes in the diameter of an artificial pupil is shown in Fig. XXI-65. The response to changes in eye position is equally rapid.

Difficulties encountered in consistent tracking of an actual pupil are principally the fault of the optics portion of the pupillometer. The aperture required must be small enough to keep eye or head motions along the optic axis from defocussing the scanning spot at the surface of the eye. This in turn requires a brighter light for the scanning than was obtainable from the face of the cathode-ray oscilloscope used in this prototype.

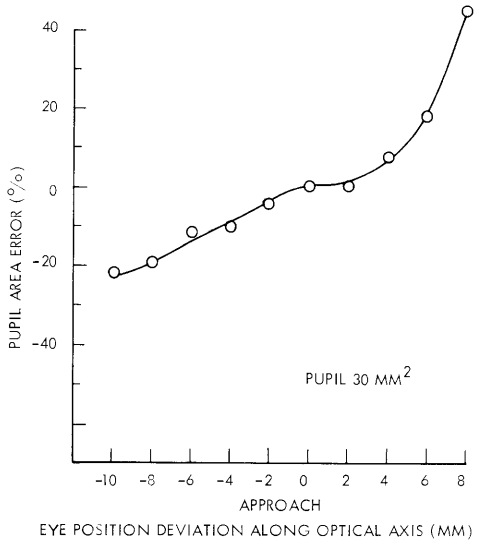

Fig. XXI-62. Effect of eye position along optical axis on pupil area measurement.

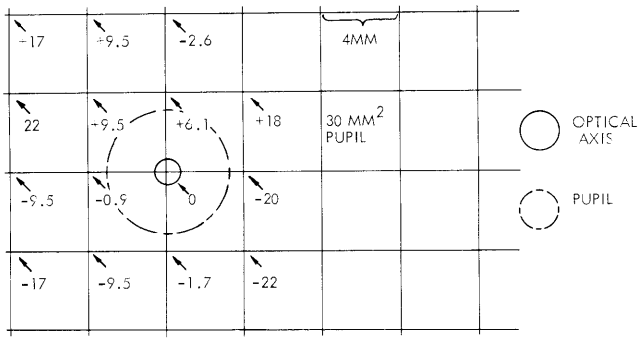

Fig. XXI-63. Pupil-area error in per cent when center of pupil is shifted in plane of focus. Percentage of error is the number beneath the corresponding positive arrow.

3. Television Stimulator

An excitation light source for the human pupil which is linear over a wide range of light flux has been developed. This stimulator uses the light flux emitted from the screen of an ordinary television receiver[5] cathode-ray tube. This flux is controlled by pulse-rate modulating the cathode, and a linear range of constant-spectrum light over 3.3 log units of intensity is obtained. Constant-width and constant-amplitude pulses are applied to the cathode-ray tube grid and cause it to produce a series of bright-light bars alternating with strips of darkness during which the tube is cut off. A diffusing screen

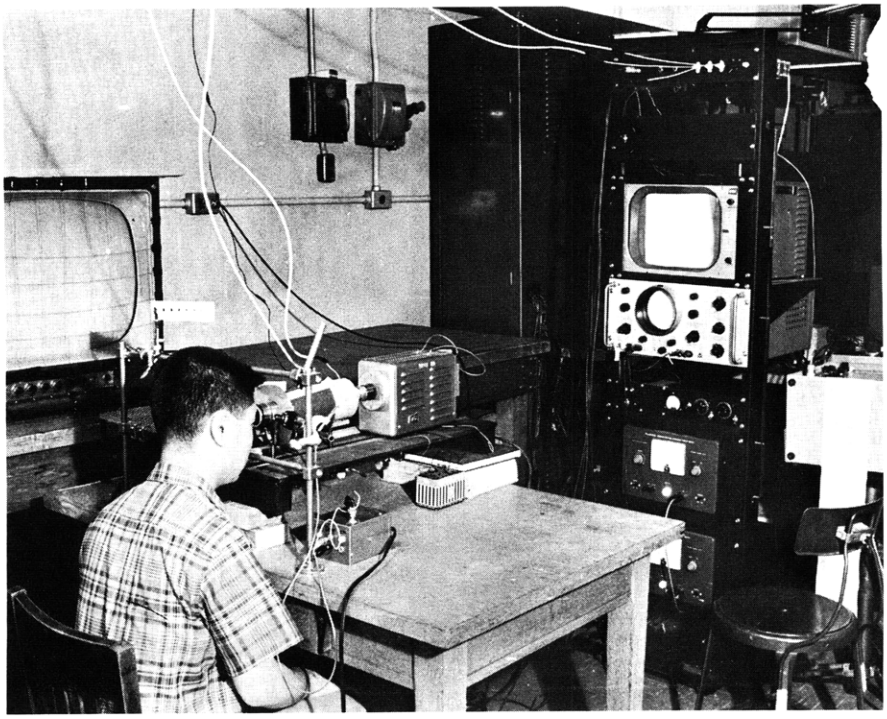

Fig. XXI-64. The Television Pupillometer with a subject in place. The camera is directly in front of the subject; the monitoring television screen, together with subsidiary electronic equipment, is in the rack in front of the subject. The large television screen at the left of the subject can also be used for displaying the eye. The pen recorder is at the right of the equipment rack.

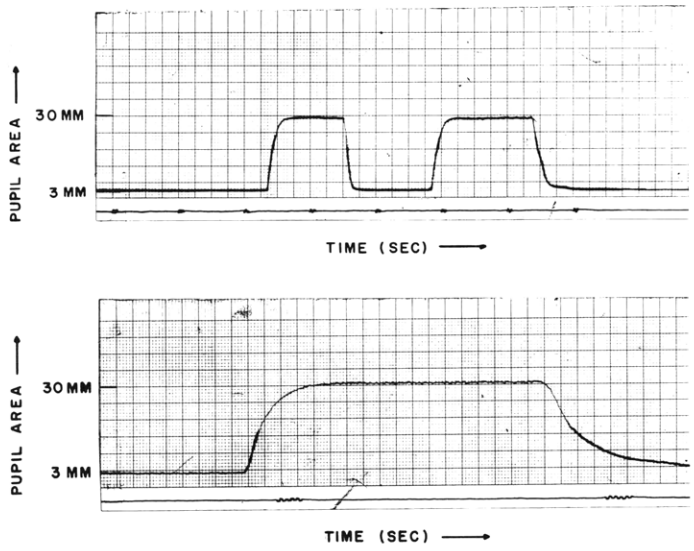

Fig. XXI-65. Step response of nonlinear scanning pupillometer. Top trace, 25 mm/sec; bottom trace, 100 mm/sec.

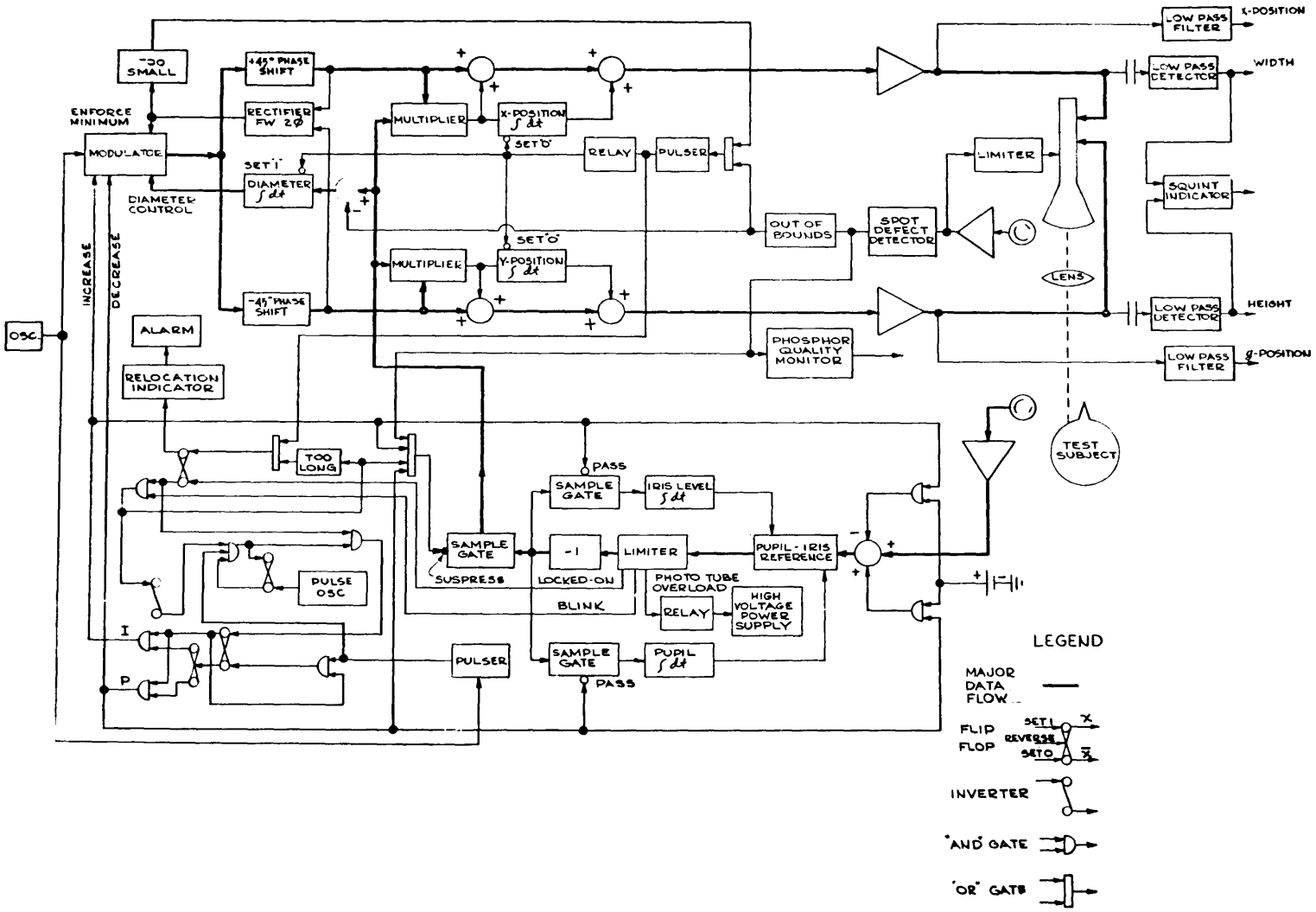

Fig. XXI-66. Block diagram of nonlinear scanning pupillometer.

keeps the subject from being distracted by the apparent motion of the bars across the screen.

S. Asano, C. A. Finnila, G. Sever,
S. Stanten, L. Stark, P. A. Willis

References

1. L. Stark, Stability, oscillations and noise in the human pupil servomechanism, Proc. IRE 47, 1925-1939 (1959).

2. O. Lowenstein, Pupillography: Methods and diagnostic systems, A. M. A. Arch. Ophthalmol. 55, 565-571 (1956).

3. G. W. King, An improved electronic pupillograph for clinical use, Proc. National Electronics Conference, Vol. 16, 1960, pp. 672-676.

4. C. A. Finnila, A Convenient Eye Position and Pupil Size Meter, S. M. Thesis, Department of Electrical Engineering, M. I. T., June 1962. [Professor William Schreiber helped freely with advice and suggestions.]

5. G. Sever, Linear Light Source for Eye Stimulation, S. B. Thesis, Department of Electrical Engineering, M. I. T., June 1962.

J. RE-EVALUATION OF THE PUPIL SYSTEM

In this report we attempt to put the various aspects of pupil research into a consistent mathematical framework.

1. A Priori Considerations

If one considers the iris muscles to be a regulator of visible power flux reaching the retina (the retina being a sensing device), their operation in our pupillometer arrangement can be schematized as shown in Fig. XXI-67. Two stimulating beam sizes are shown. These characterize two modes of pupil operation: (a) Closed-loop, for which the cross-section area of the stimulating beam is larger than the largest pupil area. In this mode the iris can regulate power flux to the retina. (b) Open-loop, for which the cross-section area of the stimulating beam is smaller than the smallest pupil area. In this mode the iris cannot affect the power flux to the retina. Thus retinal flux is completely controlled by the experimenter. Mathematical relationships between experimental variables are given in Fig. XXI-68 explicitly in block diagram form for closed- and open-loop modes. In this figure, $\mathcal{F}$ is some operator, to be empirically determined, that relates the flux function $\phi(t)$ to the pupil area $A(t)$. Notice that the closed-loop mode yields an implicit equation for A which cannot be explicitly solved without knowing something about the operator $\mathcal{F}$. Even if $\mathcal{F}$ is known, a simple closed-form solution may not be obtainable. The open-loop case, on the other hand, gives an explicit expression for A. The argument ϕ of $\mathcal{F}$ is completely controlled by

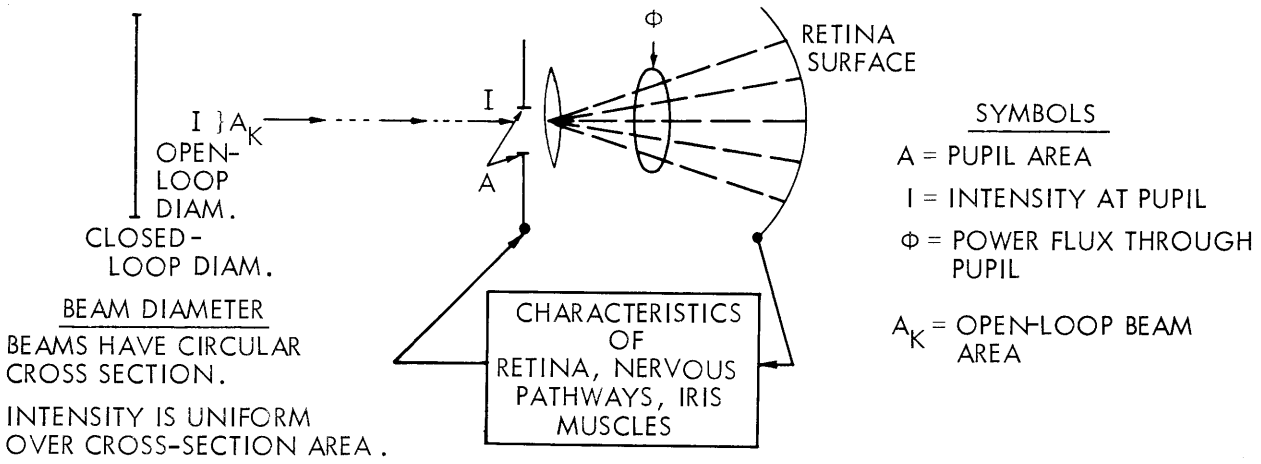

Fig. XXI-67. Functional description of pupil operation.

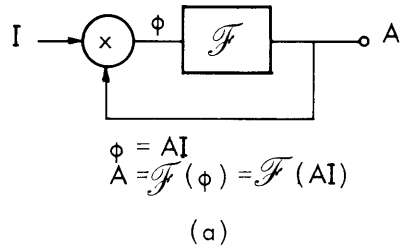

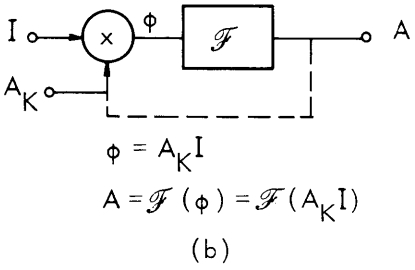

Fig. XXI-68. Mathematical relationships between experimental variables. (a) Closed loop. (b) Open loop.

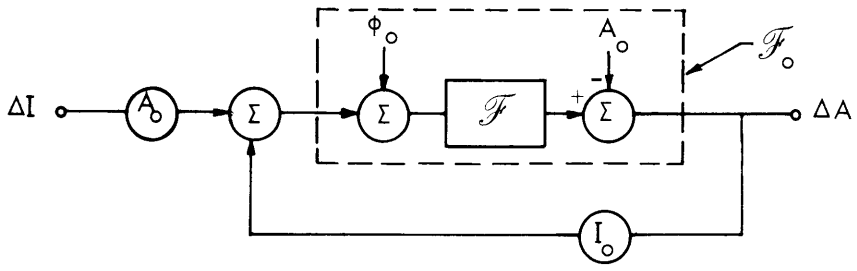

Fig. XXI-69. Block diagram for model with linearized multiplier.

the experimenter. This mode provides the easier method for experimentally determining $\mathcal{F}$.

For small signals ΔA, ΔI about operating levels A_o, I_o the multiplicative feedback operation can be linearized as follows:

$$\phi = AI = (A_o+\Delta A)(I_o+\Delta I) = A_oI_o + I_o\Delta A + A_o\Delta I + \Delta A\Delta I$$

$$\approx A_oI_o + I_o\Delta A + A_o\Delta I = \phi_o + \Delta\phi.$$

Thus the closed-loop equations for small signals become

$$\Delta\phi = I_o\Delta A + A_o\Delta I$$

$$\Delta A = \mathcal{F}(\phi_o+\Delta\phi) - A_o$$

$$= \mathcal{F}_o(\Delta\phi).$$

The corresponding block diagram is shown in Fig. XXI-69.

2. Experimentally Observed Characteristics of $\mathcal{F}$

For small sinusoidal inputs the pupil behaves in an easily predictable manner. The response to a sinusoid, both open-and closed-loop, is principally the fundamental. The fundamental output amplitude is roughly proportional to the input amplitude at any given frequency. The effects of short-time variations in output amplitudes can be neglected by considering average responses. In view of these observations, one can categorize

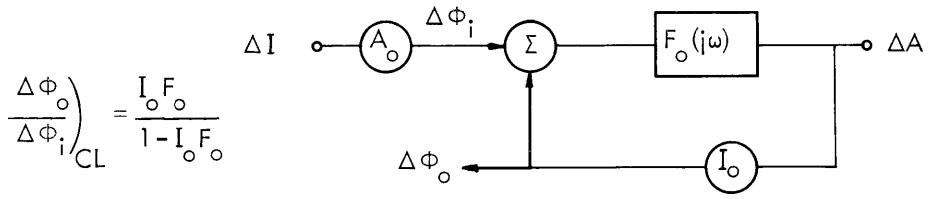

Fig. XXI-70. Closed-loop relationships for small sinusoidal inputs.

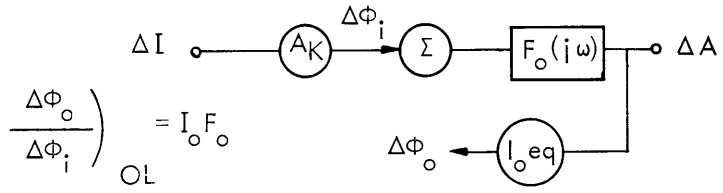

Fig. XXI-71. Open-loop relationships for small sinusoidal inputs.

the open-loop system response for this class of inputs by a transfer function $G_2(j\omega)$. For closed-loop operation the system can by characterized by some other transfer function $F_1(j\omega)$. If the feedback mechanism is approximately additive (for example, as shown above, the multiplicative pupil feedback is roughly additive for small signals), and if the feedback path contains a network whose sinusoidal response can be characterized by a transfer function $H(j\omega)$, then the formula

$$\left.\frac{\Delta A}{\Delta I}\right)_{\substack{\text{Closed}\\ \text{Loop}}} = F_1(j\omega) = \frac{G_1(j\omega)}{1 - H(j\omega)\, G_1(j\omega)}$$

is valid.

It has been found[1] that $G_1(j\omega)$ can be expressed in the form:

$$\left.\frac{\Delta A}{\Delta I}\right)_{\substack{\text{Open}\\ \text{Loop}}} = G_1(j\omega) = \frac{-k\, e^{-j\omega\tau}}{(1+j\omega\tau_1)^3},$$

where $\tau = 0.2$ sec; $\tau_1 = 0.1$ sec; and $k = k(A_o, I_o)$.

It is sometimes convenient to speak in terms of flux and define a dimensionless gain for the closed-loop situation with linearized multiplier. A definition that has been useful for predicting system instability[1] has been

$$G(j\omega) = \left.\frac{\Delta\phi_o}{\Delta\phi_i}\right)_{CL} = \frac{I_o \Delta A}{A_o \Delta I} \quad \text{for closed loop.}$$

For small-signal sinusoids $\mathcal{F}_o \approx F_o(j\omega)$. The closed-loop relation of F_o to G is shown in Fig. XXI-70. To find the relation between F_o and G for the open-loop case, one must consider the effect of the change in area of the stimulating beam. We must define an equivalent intensity $Ieq = I_o eq + \Delta Ieq$ so that $\phi_o = A_K I_o = A_o I_o eq$. Then $\Delta\phi_o = I_o eq \Delta A = \frac{A_K I_o \Delta A}{A_o}$ and $\left.\frac{\Delta\phi_o}{\Delta\phi_i}\right)_{OL} = \frac{I_o eq \Delta A}{A_K \Delta I} = \frac{A_K I_o \Delta A}{A_o A_K \Delta I} = \frac{I_o \Delta A}{A_o \Delta I}$. The formula $\left.\frac{\Delta\phi_o}{\Delta\phi_i}\right)_{OL}$ reduces to the same form as the closed-loop case, since correction factors for open-loop beam area cancel $\frac{\Delta Ieq}{I_o eq} = \frac{\Delta I}{I_o}$. The open-loop relation between F_o and G is shown in Fig. XXI-71.

3. Note on Pupil Models

From sinusoidal data the pupil was originally given the block form[2] shown in Fig. XXI-72. It was supposed that a reference signal (probably a function of average intensity) was generated in the retina or nervous system, and that incoming changes in flux were compared with this. If one makes this reference flux just a short-time

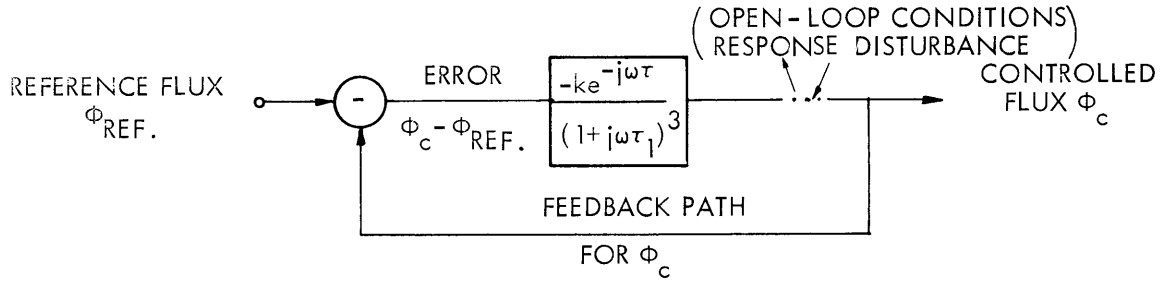

Fig. XXI-72. Early pupil block diagram used by Stark[2] for describing sinusoidal data.

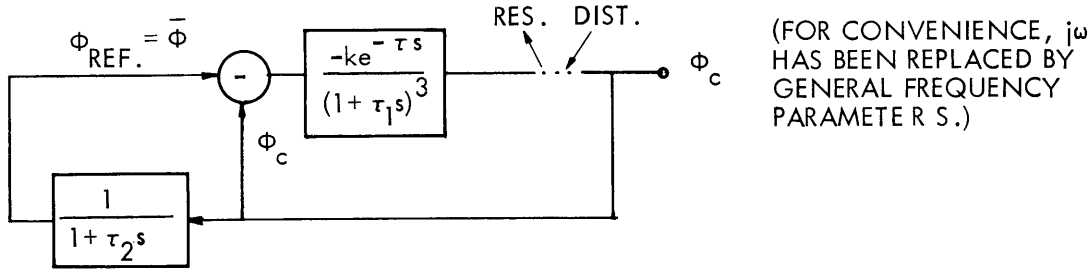

Fig. XXI-73. Modification of Fig. XXI-72 with $\phi_{REF} = \bar{\phi}$.

average flux ($\bar{\phi}$), then the block form is as shown in Fig. XXI-73. This configuration will give the correct waveform for positive step responses, in addition to providing a slowly varying reference light level. The dc error of this system will be zero. The pupil, however, exhibits a small dc gain. Such a term can be added as shown in Fig. XXI-74a. The diagram can be alternatively represented in the form given in Fig. XXI-74b and c. Notice that a summer has been added at the point of opening the loop. This represents the linearized multiplier. The form shown in Fig. XXI-74c was the one originally given by Stark.[1]

None of the diagrams shown thus far have included nonlinearity for characterizing the asymmetry seen in step responses. This can be introduced in the arrangement of Fig. XXI-74a, as shown in Fig. XXI-74d. The diagram of Fig. XXI-74d has been rotated for comparison with the form given in Fig. XXI-71.

4. Iris Muscle Constraints

The iris muscles have an interesting geometry. Here, we attempt to see what sort of constraints this places on the nature of their input-output characteristics. The muscles are sketched in Fig. XXI-75.

The sympathetic portion of the pupil system has a much smaller and more sluggish response than the parasympathetic part. We make the simplifying assumption that for fast light changes the dilator muscle is not driven by its nerve supply, and thus fast

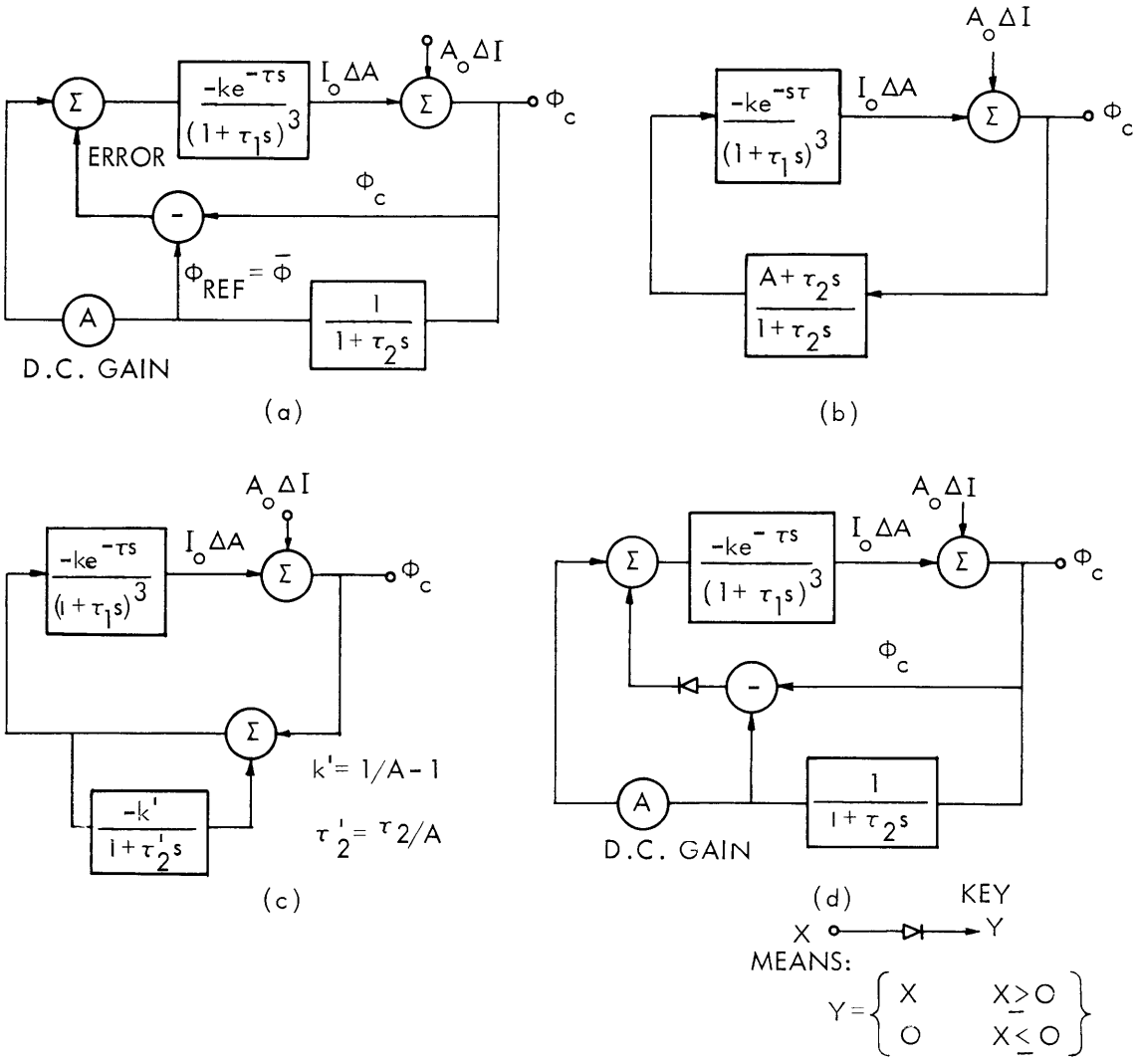

Fig. XXI-74. (a) Modification of Fig. XXI-73 with dc gain (A) added; (b) and (c) alternative representations of (a); (d) asymmetry represented by addition of nonlinearity to (a)

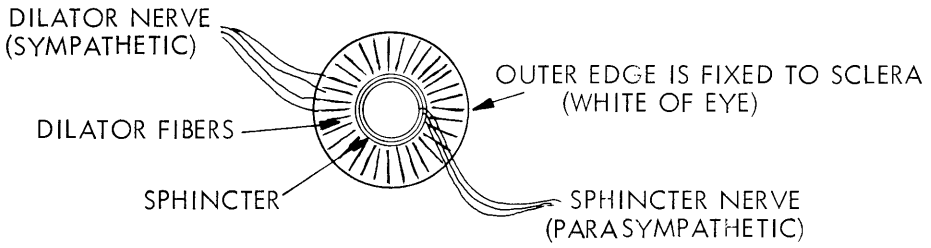

Fig. XXI-75. Iris muscles.

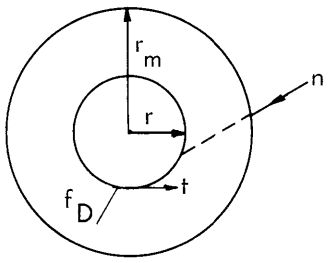

n = NERVE PULSE FREQUENCY
r = PUPIL RADIAL
t = SPHINCTER TENSION FORCE
f_D = RADICAL DILATOR FORCE/LENGTH
r_m = MAXIMUM PUPIL RADIUS

Fig. XXI-76. Simplified muscle system.

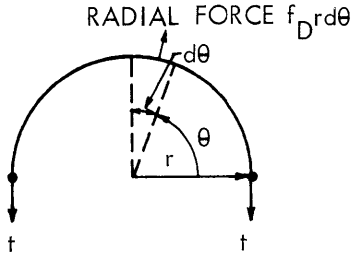

HORIZONTAL FORCES CANCEL

SUMMING VERTICAL FORCES

$$2t = \int_0^{\pi} f_D \sin\theta \, r \, d\theta = \left[\int_0^{\pi} \sin\theta \, d\theta\right] r f_D = 2 r f_D$$

THUS $t = r f_D$ FOR STATIC EQUILIBRIUM

Fig. XXI-77. Derivation of equilibrium relationship between f_D and t.

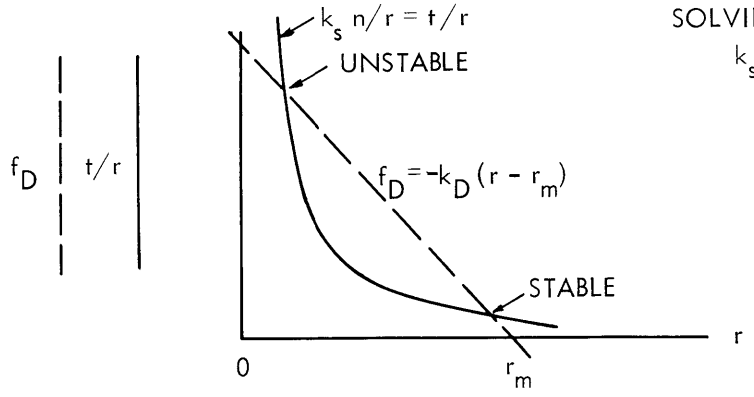

SOLVING FOR EQUILIBRIUM POINTS

$$k_s n = - k_D (r - r_m) r$$

$$\text{or } r^2 - r_m r + k_s/k_D \, n = 0$$

$$r = r_m/2 \pm \sqrt{\frac{r_m^2}{4} - \frac{k_s}{k_D} n}$$

Fig. XXI-78. Static equilibrium points for case 1.

responses (that is, transients up to ~3 sec duration) are attributed to nervous activation and deactivation of the sphincter alone. We can thus characterize the system for fast changes by a parasympathetic nervous pulse-frequency input n(t) driving a sphincter that is coupled to a passive dilator. We can treat the pupil radius r(t) as the output. The simplified muscle system is illsutrated in Fig. XXI-76.

We shall only consider conditions for static equilibrium here. In the static case $t = t(n, r)$ and $f_D = f_D(r)$. The equilibrium relationship between f_D and t can be derived by considering one-half the sphincter as a free body and by requiring that the sum of the forces acting on it be zero. The derivation is given in Fig. XXI-77, the result being $t = rf$. Laplace derived a similar formula for the relationship between the pressure exerted by a fluid on a cylindrical container and the tension in the container walls. We now proceed to derive the results of making some simple assumptions concerning the nature of f_D, t.

Case 1

Suppose that the sphincter is a tension source, that $t = k_s n$, and that the dilator is a simple spring $f_D = -k_D(r-r_m)$. Substituting these functions in the equilibrium equation gives $t = k_s n = -k_D(r-r_m)r = rf_D$. The radial forces f_D and t/r are plotted in Fig. XXI-78 for a midrange value of n. The intersections are the equilibrium points. Notice that equilibrium points below $r_m/2$ are unstable. Hence this model will not suffice to describe muscle action in the steady state.

Case 2

Suppose that the sphincter is a spring with variable stiffness $t = k_s nr$, and that the dilator is the same as in case 1. Substituting these functions in the equilibrium

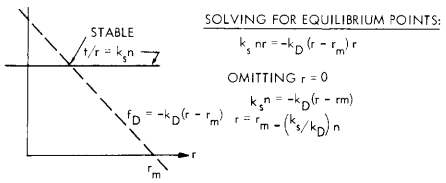

Fig. XXI-79. Static equilibrium points for case 2.

equation gives $t = k_s nr = -k_D(r-r_m)r = rf_D$. The radial forces for this case are plotted in Fig. XXI-79. Notice that there is only one equilibrium point for a given value of n, and it is always stable. Thus the assumptions made in this case lead to an allowable description of muscle behavior.

I. Sobel, L. Stark

References

1. L. Stark, Stability, oscillations, and noise in the human pupil servomechanism, Proc. IRE 47, 1925-1939 (1959).

2. L. Stark and P. M. Sherman, A servoanalytic study of the consensual pupil reflex to light, J. Neurophysiol. 20, 17-26 (1957).

K. ANALOG SIMULATION OF THE HUMAN PUPIL SYSTEM

1. Introduction

The attempt to simulate the human pupil system's response to light has led to the construction of two analog models of the pupil system. Before actually going into each system in detail it is useful to briefly review some of the more outstanding features of the pupil's transient behavior to pulses of light and darkness. Figure XXI-80a shows, in schematic form, typical pupillary responses to light, and Fig. XXI-80b shows actual pupil responses to light.

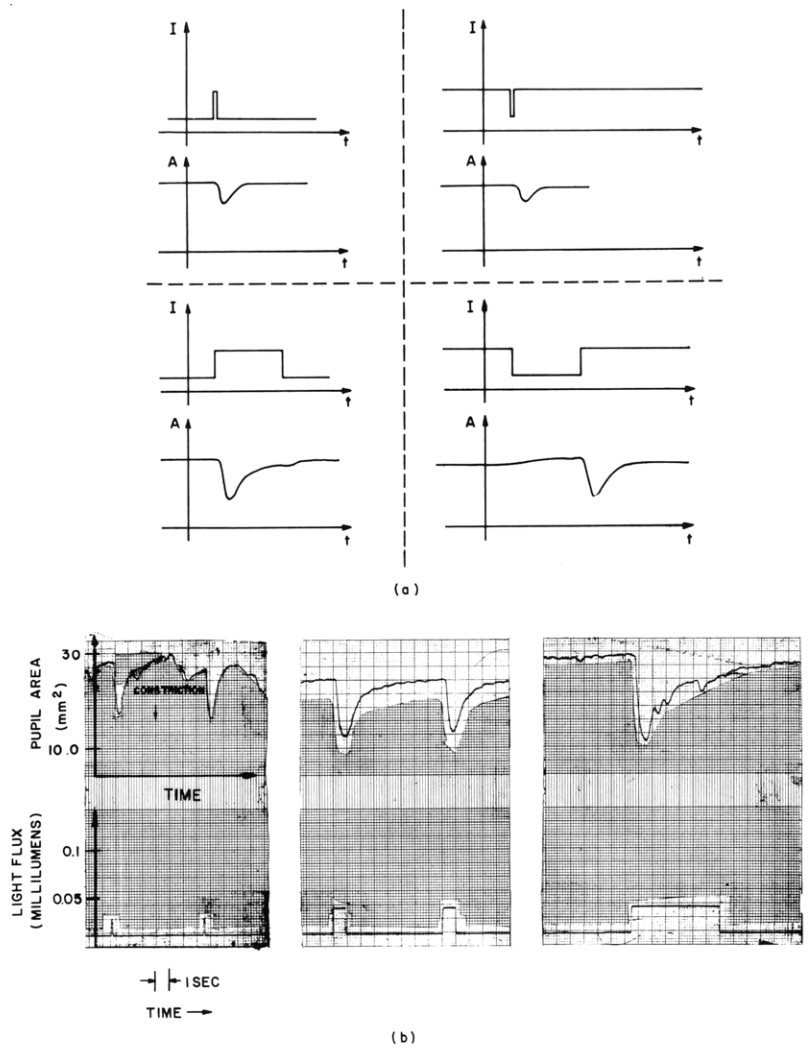

Fig. XXI-80. (a) Schematic representation of pupillary responses to light. (b) Actual pupil responses to light.

The design in both models is dictated by the simple observation that the pupil response is greater to an increase in light than to a decrease in light. The terms increase and decrease are clearly not very quantitative and their quantification in two different forms results in two different models. In the first model to be considered, the present value of light intensity is compared with an exponentially weighted integral of the past light which is given the significance of an average light intensity. The second model compares the present value of light with its immediately preceding value by measuring the sign of the derivative dI/dt. In each model the state of a diode, and hence system response, is controlled by the respective comparison.

It is evident from experimental data that an intrinsic asymmetry exists in the system regardless of how small the input signal is made. Also, various forms of scale compression and amplitude nonlinearities exist. Pulse experiments by Van Der Twell and Van Der Gon[1] and F. Baker[2] indicate that great nonlinearities exist with respect to pulse width of excitation light. The human pupillary system is indeed quite complicated, and in forming the models to be presented here no attempt has been made to account for all experimental data but rather to, at least initially, keep the models as simple as possible. We have concentrated mainly on getting agreement with certain gross short-term adaptation phenomena.

2. Basic Form of Models

Both models to be presented here have the same basic arrangement of blocks, as shown in Fig. XXI-81.

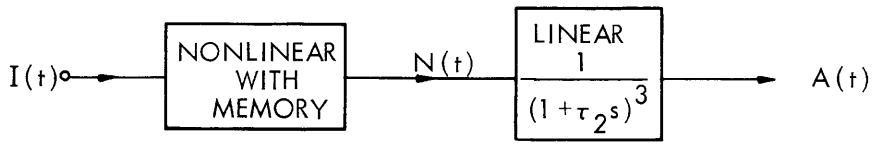

Fig. XXI-81. Basic block diagram of pupil models.

In working with the model of Fig. XXI-81 we have come to think of the linear triple lag as representing the pupillary muscles and we associate the nonlinear box with the retina and nervous system. Therefore N(t) is associated with some hypothetical nerve signal. It cannot be emphasized too strongly that this identification of various boxes in the model with certain biological quantities is presently merely a mnemonic convenience and has no profound physiological significance.

3. Model Making

a. Model 1

The redilatation of the pupil after initial constriction, when a step of light is used as excitation, can be thought of as a light-adaptation process. We interpret this

process by postulating that the pupil system responds to the difference between the present value of light intensity I(t) and some average light intensity called $\bar{I}$. This continuously computed average intensity is an exponentially weighted integral of the past light intensity. Thus $\bar{I}(t) = \frac{1}{\tau_1} \int_0^t I(x)\, e^{-\frac{x}{\tau_1}} dx$.

In order to account for the observed asymmetry, we postulate that the pupil does not respond appreciably to changes of intensity below $\bar{I}$. The rectification (clipping) of the negative portion of $I(t)-\bar{I}(t)$ accomplishes this requirement for asymmetry. Two examples of the procedure are shown in Fig. XXI-82.

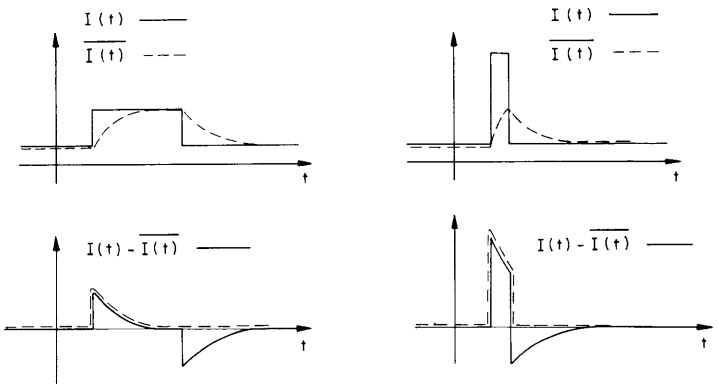

Fig. XXI-82. Generation of I(t).

As can be seen from Fig. XXI-80a the pupil exhibits a slight dc gain, inasmuch as it does not redilate to its original area when a step of light is applied. Since $\delta I = I - \bar{I}$ tends to zero as time approaches infinity for a step input, we add a fraction of $\bar{I}$ to δI in order to obtain the needed dc gain. The block diagram of Model 1 is illustrated in Fig. XXI-83.

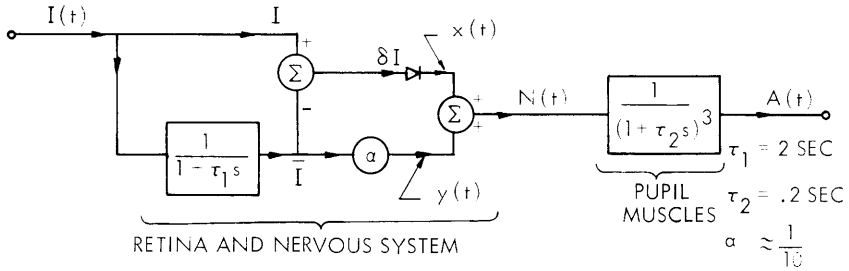

Fig. XXI-83. Block diagram of Model 1.

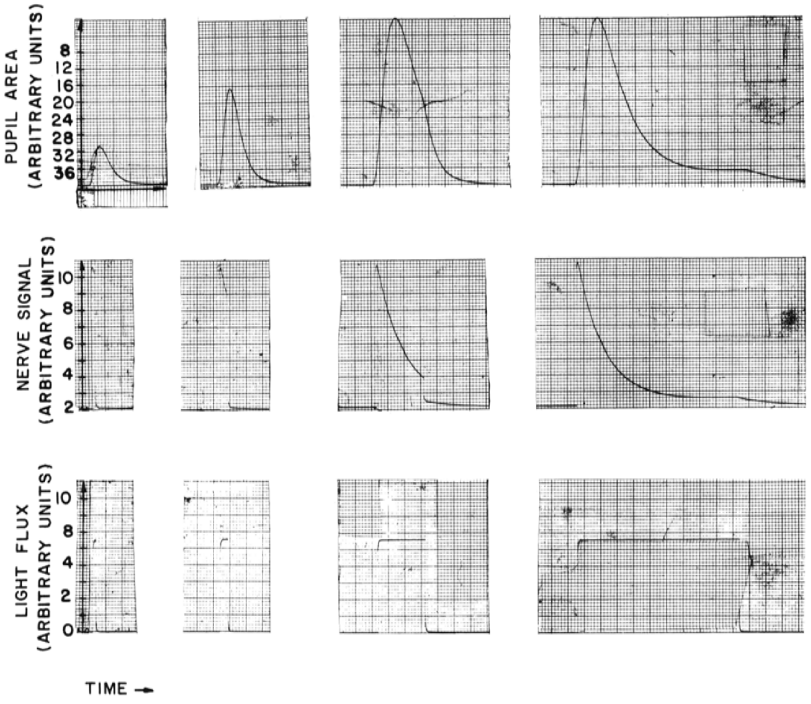

(a)

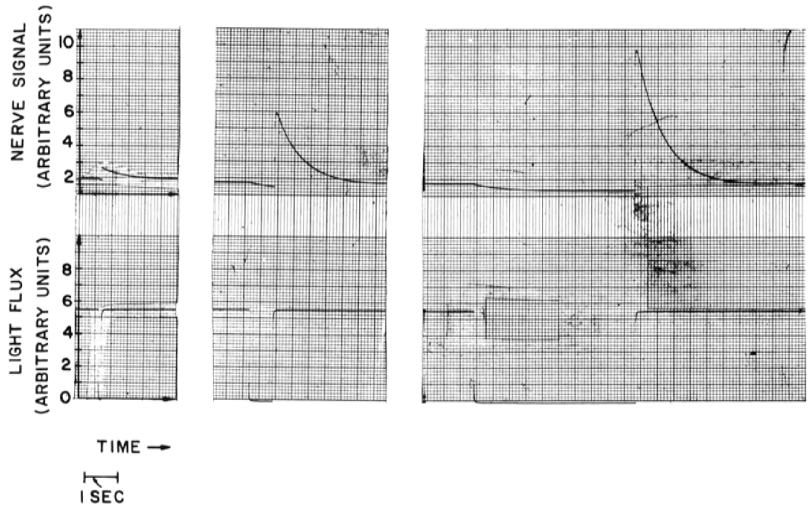

(b)

Fig. XXI-84. Simulated pupil responses of Model 1 to (a) positive pulses of light and (b) negative pulses of light.

The model of Fig. XXI-83 was simulated in the laboratory by using Philbrick operational amplifiers. The results of that simulation for positive light pulses is shown in Fig. XXI-84a.

The simulated pupil response to light is in fairly good agreement with actual observed pupil-response data. The relatively large biological noise level, especially at large light levels, and system variability have prevented us from making a detailed and quantitative comparison between actual and simulated data.

When dark pulses of light are used to excite the pupil system, the basic asymmetry is evident. This is illsutrated in Fig. XXI-80c and 80d, in which it can be seen that the pupil's response to the turning off of the light is relatively small in comparison with its response to the turning on of the light after the dark pulse is complete. Thus the observed pupil response to a dark pulse is really the response to the increase in light level after a period of low light level. As discussed in Quarterly Progress Report No. 61 (pages 223-230), the pupil's response to dark pulses is greatly affected by pulse width (time during which the eye is in subdued light), there being a greater response to the increase in light for a larger pulse width. The effect has been called rapid dark adaptation to distinguish it from the well-known long-term dark adaptation.

Simulation of this effect is seen in Fig. XXI-84b.

b. Model 2

The second analog model was constructed to be almost identical with the one proposed by Clynes.[3] In this model the time derivative of the input light intensity determines the state of a diode and, hence, the transfer function of the model. More specifically, when $dI/dt > 0$ the transfer function is different from that which it is when $dI/dt < 0$, so that a large response is obtained when $dI/dt > 0$ and a very weak response is obtained when $dI/dt < 0$; thus these characteristics of the model agree with the observed pupil asymmetry. When $dI/dt > 0$ the pupil responds mainly to the rate of change of the intensity and also slightly to the generally increasing value of light ($\bar{I}$). The latter response is given the term proportion response while the former is identified as a rate sensitive response. When $dI/dt < 0$ the rate sensitive response is absent.

A block diagram of Clynes' model is shown in Fig. XXI-85.

The relationship between the two models is very simple if the first model is redrawn as is illustrated in Fig. XXI-86.

A sample of some typical N(t) responses is shown in Fig. XXI-87. Notice the extreme similarity, both in magnitude and shape of responses for various pulse

inputs. This is a consequence of the fact that responses are primarily determined by the part of the input for which $dI/dt > 0$ is independent of the time that $dI/dt \leq 0$ (pulse width).

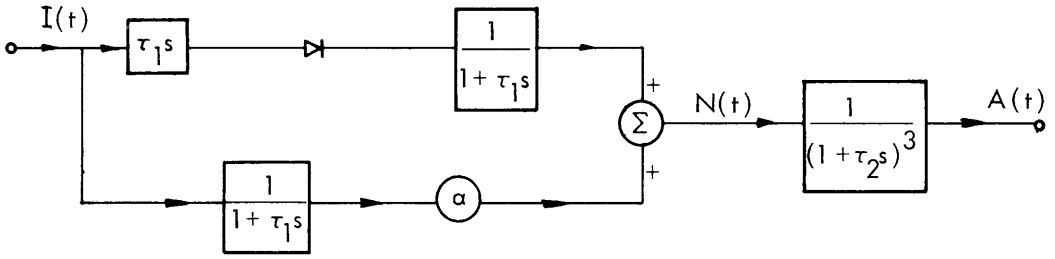

Fig. XXI-85. Model 2. $\tau_1 = 2$ sec; $\tau_2 = 0.2$ sec; $\alpha = 1/10$.

4. Comparison of the Two Models

Model 1 has several advantages over the Clynes type of representation, since it can account for a greater variety of actual experimental results. The same mechanism that causes the simulated response to indicate redilation of the pupil after

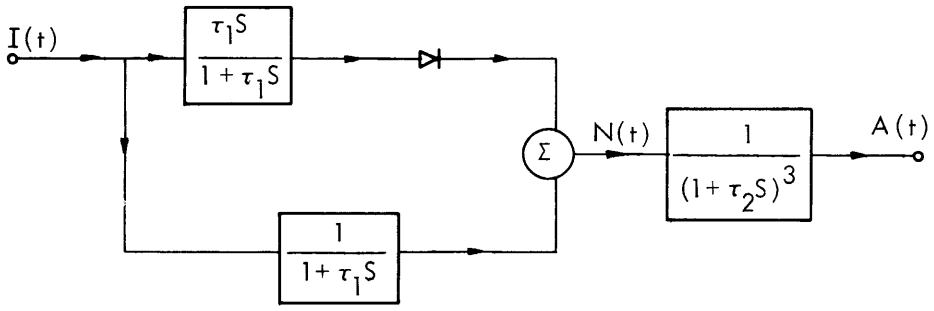

Fig. XXI-86. Variation of Model 1.

constriction when a step input is used also accounts for the rapid dark-adaptation effect. This phenomenon cannot be accounted for by the Clynes model without making it more complex. Also, Model 1 predicts that if two successive pulses are used as input, the response of the second should be less than that of the first

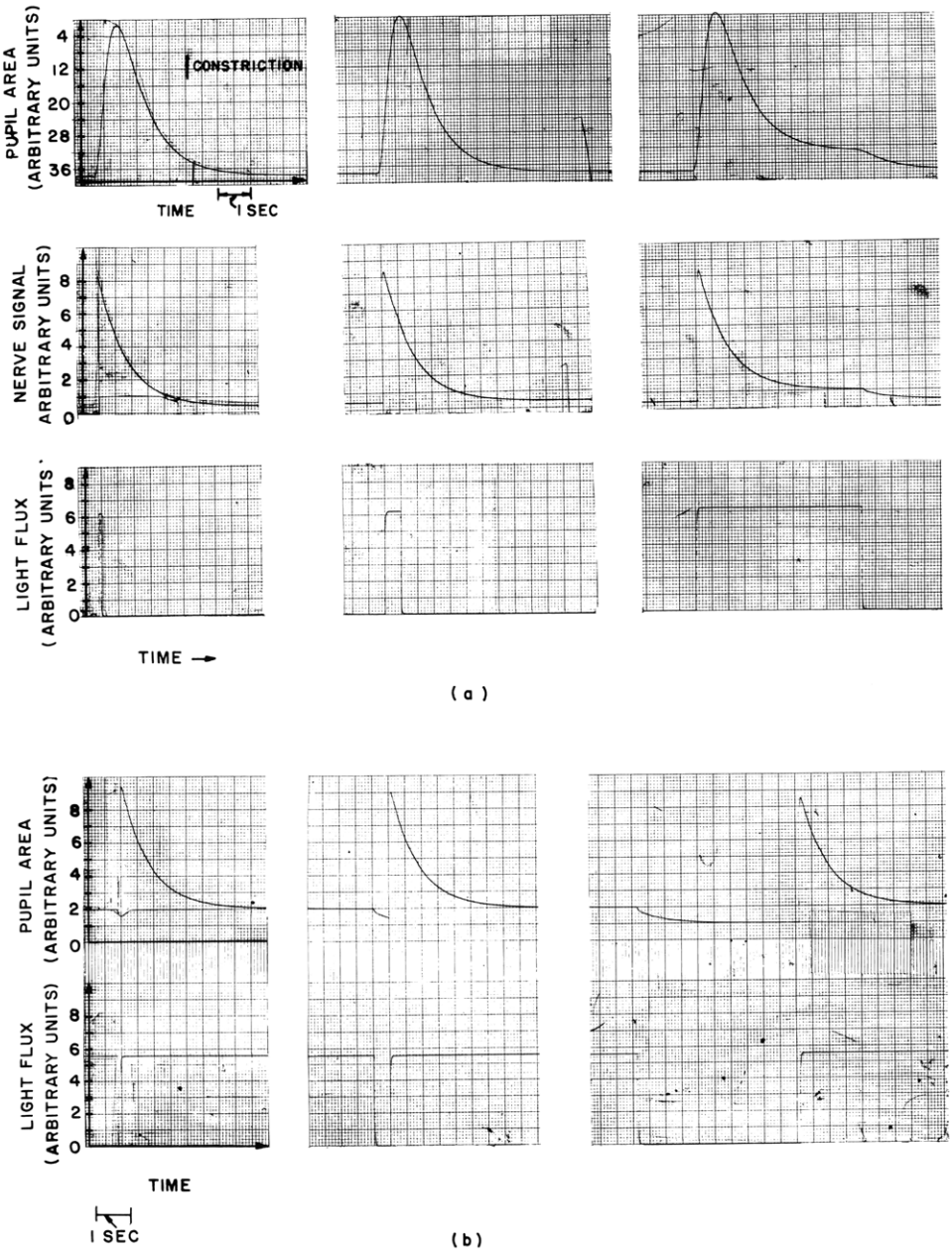

Fig. XXI-87. Simulated pupil responses of Model 2 to (a) positive pulses of light and (b) negative pulses of light.

pulse. This effect is shown in Fig. XXI-88. This phenomenon is observed in the pupil system although exact quantitative agreement with Model 1 is still questionable. Model 2, on the other hand, wrongly predicts that the response to the second pulse is almost identical with the response to the first pulse. Another feature that makes Model 1 appear plausible is its agreement with observed data concerning the relationship between time to peak of response and pulse width of stimulus. The increase in time to peak as pulse width is increased is shown in Fig. XXI-84a.

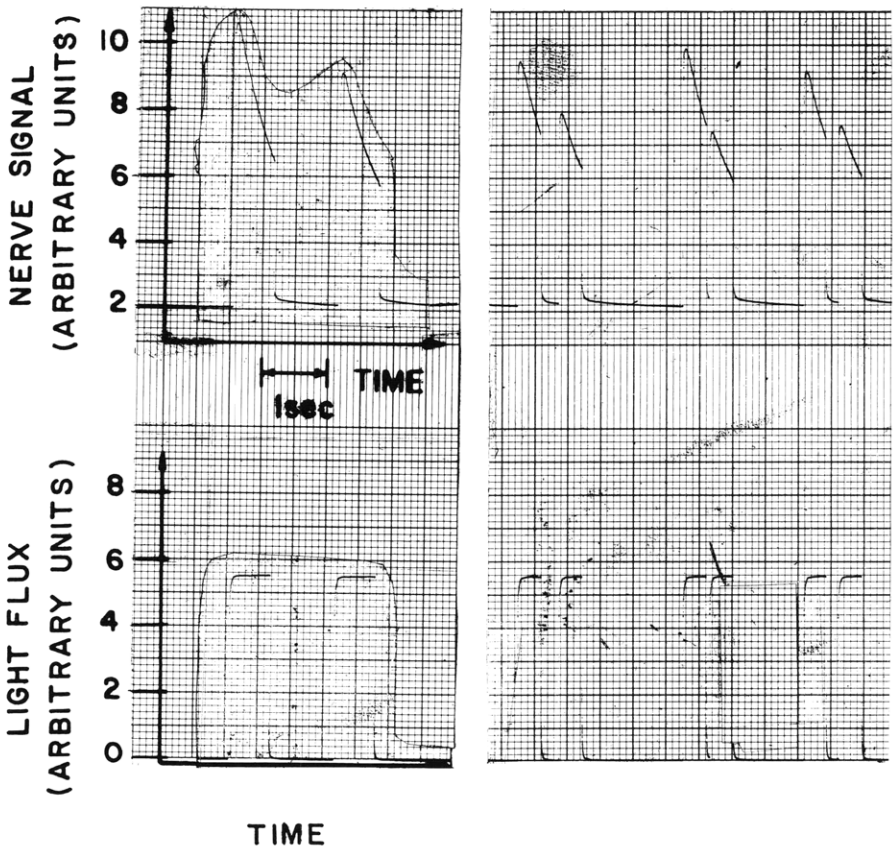

Fig. XXI-88. Light adaptation.

Unfortunately, Model 1 has some serious defects. Figure XXI-84a shows a simulated response to a 1.5-sec pulse of light. At the time that the light is suddenly reduced there is a marked increase in dilation rate. This is not observed in actual pupil responses. Also, some recently performed experiments with a ramp input seem to indicate some form of derivative effect very similar to that of Model 2.

5. Switching Problem

Obvious nonlinearities in the pupil system necessitate the presence of diodes or other nonlinear elements in any model that is made. One cannot make even crude transient approximations without including nonlinear effects. With diodes in the model, changing of their states immediately becomes crucial in determining system behavior. An important question is to determine the system variable that should control the state of the diodes. In Model 1 the judicially chosen variable used to control the diode state was $I-\bar{I}$, and dI/dt was used in Model 2. Exactly what function should govern the switching of the diode cannot be easily answered. Probably a combination of the two models will prove sufficient to explain a wide variety of experimental results.

A. A. Sandberg, L. Stark

References

1. F. Baker, Pupil response to short-duration pulses, Quarterly Progress Report No. 65, Research Laboratory of Electronics, M. I. T., April 15, 1961, pp. 251-257.

2. L. H. Van Der Twell and J. J. Denier Van Der Gon, The light reflex of the normal pupil of man, Acta Physiol. Pharmacol. Neer. 8, 69 (1959); see Fig. 15.

3. M. Clynes, Biologic control system characteristics and biologic rhythms, Digest of the 1961 International Conference on Medical Electronics, New York City, July 1961, edited by Peter L. Frommer (The Conference Committee for the 1961 International Conference on Medical Electronics, Leslie E. Flory, Chairman, RCA Laboratories, Princeton, N. J., 1961), p. 59.